Since 1955

Strojniški vestnik
Journal of Mechanical Engineering

no. 3
year 2020
volume 66

Strojniški vestnik – Journal of Mechanical Engineering (SV-JME)

Aim and Scope

The international journal publishes original and (mini)review articles covering the concepts of materials science, mechanics, kinematics, thermodynamics, energy and environment, mechatronics and robotics, fluid mechanics, tribology, cybernetics, industrial engineering and structural analysis.

The journal follows new trends and progress proven practice in the mechanical engineering and also in the closely related sciences as are electrical, civil and process engineering, medicine, microbiology, ecology, agriculture, transport systems, aviation, and others, thus creating a unique forum for interdisciplinary or multidisciplinary dialogue.

The international conferences selected papers are welcome for publishing as a special issue of SV-JME with invited co-editor(s).

Editorial Office

University of Ljubljana, Faculty of Mechanical Engineering

SV-JME, Aškerčeva 6, SI-1000 Ljubljana, Slovenia

Phone: 386 (0)1 4771 137

Fax: 386 (0)1 2518 567

info@sv-jme.eu, http://www.sv-jme.eu

Print: Koštomaj printing office, printed in 275 copies

Founders and Publishers

University of Ljubljana, Faculty of Mechanical Engineering, Slovenia

University of Maribor, Faculty of Mechanical Engineering, Slovenia

Association of Mechanical Engineers of Slovenia

Chamber of Commerce and Industry of Slovenia, Metal Processing Industry Association

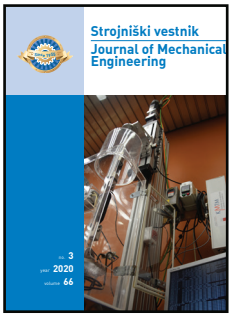

Cover:
In house developed tensile-testing device for human soft tissue characterization with upgraded control system built using low cost hardware and open source software. Accurate and reliable measuring equipment is crucial for acquiring good experimental results in all fields of material characterization, especially for gathering human tissue mechanical properties.

Image courtesy:
University of Ljubljana, Faculty of Mechanical Engineering, Chair of Modeling in Engineering Sciences and Medicine (KMTM), Slovenia

General information

Strojniški vestnik – Journal of Mechanical Engineering is published in 11 issues per year (July and August is a double issue).

Institutional prices include print & online access: institutional subscription price and foreign subscription €100,00 (the price of a single issue is €10,00); general public subscription and student subscription €50,00 (the price of a single issue is €5,00). Prices are exclusive of tax. Delivery is included in the price. The recipient is responsible for paying any import duties or taxes. Legal title passes to the customer on dispatch by our distributor. Single issues from current and recent volumes are available at the current single-issue price. To order the journal, please complete the form on our website. For submissions, subscriptions and all other information please visit: *http://www.sv-jme.eu.*

You can advertise on the inner and outer side of the back cover of the journal. The authors of the published papers are invited to send photos or pictures with short explanation for cover content.

We would like to thank the reviewers who have taken part in the peer-review process.

ISSN 0039-2480, ISSN 2536-2948 (online)

The journal is subsidized by Slovenian Research Agency.

Strojniški vestnik - Journal of Mechanical Engineering is available on *https://www.sv-jme.eu*.

Contents

Strojniški vestnik - Journal of Mechanical Engineering
volume 66, (2020), number 3
Ljubljana, March 2020
ISSN 0039-2480

Published monthly

Papers

Strojniški vestnik - Journal of Mechanical Engineering 66(2020)3, 155-163,

DOI:10.5545/sv-jme.2019.6418 Original Scientific Paper
Received for review: 2019-10-30
Received revised form: 2020-01-07
Accepted for publication: 2020-01-22

Control System for a Tensile-Testing Device Using Low-Cost Hardware and Open-Source Software

Matej Kranjec* – Jernej Korinšek – Miha Ambrož – Robert Kunc
University of Ljubljana, Faculty of Mechanical Engineering, Slovenia

The aim of this study is to verify whether a Raspberry Pi 3 B+ can be utilized as a low-cost device for controlling a tensile-testing device used for material research purposes. A list of requirements based on already-available hardware was drawn up, which the new control system had to fulfil. To connect all the necessary equipment, a connection board was constructed, and some additional hardware was acquired for the system to be able to perform all the necessary tasks. The whole controlling system was also put in a small enclosure to make it portable. The control-system software was written in C++ using the Pigpio library. The developed system was then tested, and the results were compared to a commercially available Instron 8802 device. A comparison of the results shows that the upgraded equipment can produce comparable results to commercially available devices and is sufficiently accurate to be applied for research purposes for the characterization of soft tissues and other materials.
Keywords: Raspberry Pi, low-cost, tensile testing, measuring equipment

Highlights
- *Existing test device's control system has proven unreliable and has been upgraded.*
- *A Raspberry Pi was chosen as the core of the new control and data-acquisition system.*
- *The system was tested and compares favorably to a certified machine.*
- *The developed system is affordable to most researchers.*

0 INTRODUCTION

The everyday challenge of many researchers is to conduct experiments with a limited budget. We strive to spend as little as possible, but still have equipment that is reliable enough to provide accurate and fast measurements as the protocol requires. Because of the age and malfunctioning of our control and data-acquisition hardware, we wanted to upgrade that part of a specifically designed uniaxial tensile-testing machine used for the acquisition of soft-tissue material properties in physiological conditions. The proposed system had to control the motion of a stepper motor and acquire data from a magnetic linear encoder and a tensile load cell.

Many researchers have already searched for a low-cost system to replace or substitute expensive devices for their research purposes and some of them chose an open-source single-board computer (SBC) such as the Raspberry Pi [1] to [4]. The main reason for using the Raspberry Pi is its low cost, small size, versatility and a huge online community that can help solve problems while proposing improvements for new generations of the device. We decided to use the latest currently available version of the Raspberry Pi as the main processing unit for our tensile-testing device. Because of the limitations of the Raspberry Pi, a circuit board had to be constructed to connect the encoder and the motor controller. Also, an analog-to-digital converter (ADC) had to be added to acquire the data from the load cell. The goal was for the new control system to perform at least as well as the previous system, or even better. The new control solution was expected to be at least 80 % cheaper than a commercially available solution on the market.

In the world of industry and research, there are many commercially available tensile-testing devices from firms such as Instron, Hegewald&Peschke, TestResources, Mecmesin, and Labthink, where the user can buy the whole device with a control system included. Because we already had a tensile-testing device that had been developed in our laboratory and control equipment that was independent of the testing part of the machine, we were able to replace only the control part of the device.

Using the newly constructed control and data-acquisition system we want to show that low-cost equipment and simple open-source software can be used to obtain the tensile properties of materials.

1 MATERIALS AND METHODS

1.1 Tensile-Testing Machine Hardware

The main purpose of the research is to upgrade the control and data-acquisition part of our custom-built mechanical tensile-testing device (Fig. 1).

*Corr. Author's Address: Faculty of Mechanical Engineering, University of Ljubljana, Aškerčeva cesta 6, 1000 Ljubljana, Slovenia, matej.kranjec@fs.uni-lj.si

Fig. 1. *Custom-made tensile-testing machine for obtaining soft-tissue tensile properties in physiological conditions*

The device is constructed using a standard aluminum framing system (Bosch Rexroth) [5], on which a linear ball screw drive compact module (CKK 20-145, Bosch Rexroth) [6] is mounted, driven by a stepper motor (VRDM 3913/50LWCEB, Berger Lahr) [7] through a 3:1 gear-reduction gearbox (GBX080003K, Schneider electric) [8]. The motor is controlled by a motion-control stepper-motor drive (SD 326RU68S2, Berger Lahr) [9]. For measuring tensile loads, an S-type load cell (CTS63200KC25, AEP transducers) [10] connected to an analogue transmitter (ETA4/2IXO11D24, AEP transducers) [11] is used. The displacement of the carriage, fixed on the linear module, is measured using a magnetic linear incremental encoder system (EMIX 23, ELGO electronic) [12]. The tensile-testing device in this configuration can produce vertical carriage speeds of up to 80 mm/s and generate forces up to 2100 N, while measuring the movement with an accuracy of 0.001 mm at any time.

1.2 Controlling Hardware before the Upgrade

In the previous configuration [13], National Instruments (NI) equipment was used for the stepper-motor motion control (NI PCI-7324) [14] and a NI USB module for the data acquisition (NI USB-6221) [15]. NI-Max software was used for the configuration of the PCI and USB cards. The experimental protocol was developed using LabVIEW GUI software. The whole process of control and data acquisition was carried out on a personal computer (PC) running Windows XP. The sensor's sampling rate for the soft-tissue tensile testing was set to 1 kHz.

The described system is suitable for experimental work, but only if it is properly set up in both the NI Max and LabVIEW environments. The software for motion control and data acquisition must be properly coded by a trained person, otherwise damage can occur to the cards or controllers.

1.3 Upgrade Requirements

Like the old NI system, the upgraded control and acquisition system has to:

- ensure the correct speed and distance of the motor's movement in both directions,
- reliably monitor the encoder movement at all times while performing any protocol that needs the measurement of distance at any motor speed and direction,
- monitor the analogue transmitter voltage and convert it to a digital signal with at least 1000 divisions of the full load-cell measuring range,
- read measurement data from both the encoder and the load cell with a minimum frequency of 1 kHz,
- collect all the recorded data into one file or separate files that can be later combined into one,
- ensure the repeatability of the measurements,
- be simple to use (an error during component connection has to be impossible) and execute desired protocols (ease of use).

1.4 The Hardware Setup of the Proposed Upgrade

For a cost-effective upgrade, the Raspberry Pi 3 B+ (RPi) was chosen. The RPi is a miniature, low-cost SBC with a performance similar to a low-end desktop computer, but it has the advantage of being portable, upgradable and easily replaceable if any damage occurs. It is also possible to integrate the RPi into another system, as we did. The RPi can be powered via a micro USB connector using a 5 V / 2.5 A power supply or via its 40-pin general purpose input-output GPIO header using a 5 V input connector or even via Power over Ethernet (POE) with a POE HAT [16]. It uses a 1.4 GHz Broadcom's BCM2837B0, Cortex-A53 64-bit System on Chip (SoC) processor and 1 GB of LPDDR2 SDRAM. The connection to the RPi can be established using 2.4 GHz and 5 GHz

IEEE 802.11.b/g/n/ac wireless LAN, Bluetooth 4.2/BLE or Gigabit Ethernet over USB 2.0 (max. 300 Mbps) and four USB 2.0 ports. The access to other devices is provided by an extended 40-pin GPIO header. The whole operating system is stored on a micro SD card, which is also used for measurement-data storage [17]. A significant advantage of using the RPi instead of another similar SBC is its widespread community, which results in timely firmware and operating-system updates.

To collect tensile force data from the load cell through an analogue transmitter (load-cell amplifier), an analogue-to-digital converter (ADC) had to be added to our system. For this purpose, a commercially available ADC board (Baart board, Efftek UK) [18] was used. The board converts the analogue signal to digital values using an 8-channel 12-bit ADC chip (MCP 3208-BI/P, Microchip Technology Inc.) [19] with a maximum sampling frequency of 100,000 samples/s. The communication with MCP 3208 is via a Serial Peripheral Interface (SPI). The maximum SPI bus speed is 1 MHz, which is limited by its 3.3 V power supply (the chip itself can do 2 MHz at 5.0 V). The ADC process takes 1.5 cycles to sample and 12 cycles to convert, which amounts to 13.5 μs (at 1 MHz SPI bus) per channel, which can only be read one after another in sequence. The SPI line (0 or 1) of the ADC chip on the Baart board can be selected with a jumper, enabling the simultaneous connection of another Baart board to the system for possible future needs.

To connect all the components of the control system to the RPi's (GPIO) (Fig. 2), a connection board was developed (Fig. 3). The RPi GPIO limits the safe current draw to 16 mA per pin and 50 mA distributed across all the pins. The input-gate threshold is approximately 1.8 V, but can range anywhere between the maximum input low (0.8 V) and the minimum input high (2.0 V). The output drives to high (3.3 V) or low (0 V) [20] and [21].

The issues of unmatched voltage of the input signals from the magnetic encoder (5 V) and insufficient current output for the motor controller (16 mA) had to be solved. For the magnetic-encoder issue, a voltage divider was constructed using 4 kΩ and 6 kΩ resistors to convert the encoder's 5 V signals to 3 V signals that are safe to use on the RPi input GPIO pins. To amplify the signals sent to the motor controller from the RPi, an operational amplifier (MCP6002-E/P, Microchip Technology Inc.) [22] in a voltage-follower configuration was mounted to the circuit board.

The maximum output current was raised from 16 mA to 23 mA. The used operational amplifier has a 1 MHz gain bandwidth, which is fast enough for the motion controller that can receive and transmit signals with a maximum frequency of 200 kHz.

The connection board is also used to provide power to the RPi from a common 5 V power supply through a 40-pin flat ribbon cable. After initial testing, it appeared that the resistance of the flat ribbon cable wires was too high to deliver enough current at the

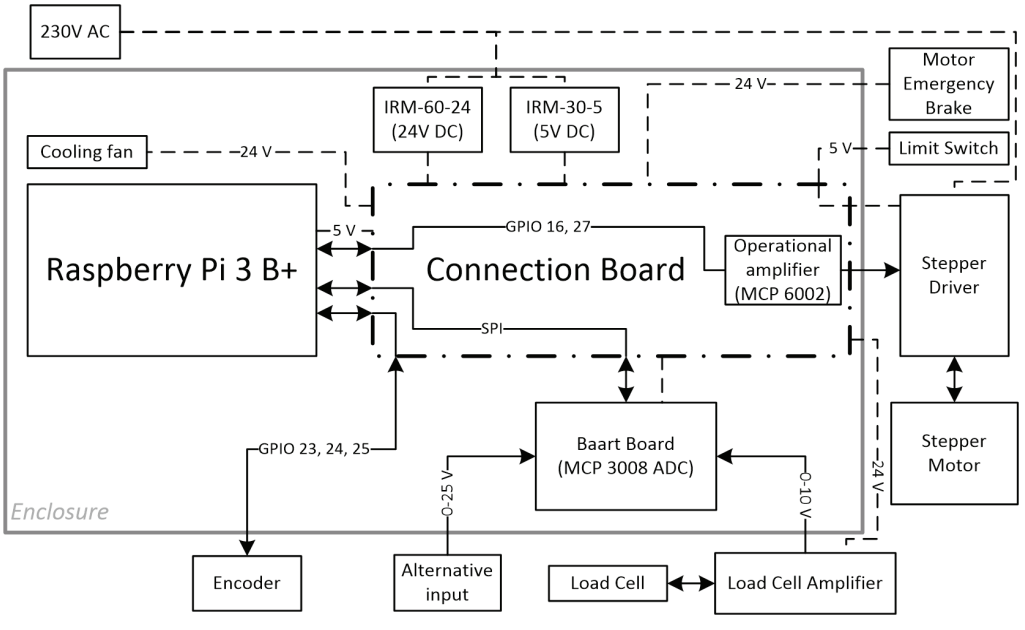

Fig. 2. *Block diagram of the whole tensile-testing system; proposed upgrade is shown inside the enclosure*

maximum operating processor load, incurring a voltage drop. For that purpose, the two 5 V power pins and at least two ground (GND) pins on the connection board had to be connected to improve the current delivery.

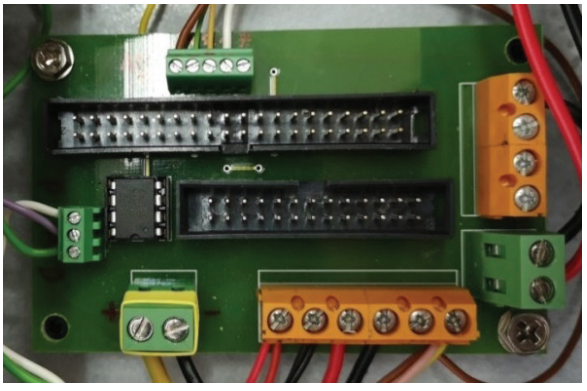

Fig. 3. *Top view of the connection board*

Some extra wire-to-board screw terminal blocks were also added to the connection board for 5 V and 24 V DC power delivery for the motor brake, inverted motor signals (as required by the installation manual of the stepper drive [9]), operational amplifier and other future devices that need a power source, which is provided using two power supplies: one for 24 V DC (IRM 60 24, Mean Well) [23] and the other for 5 V DC (IRM 30-5, Mean Well) [24]. The provided power of 60 W on the 24 V rail and 30 W on the 5 V rail is more than enough to fulfill the system's power requirements. The detailed and complete connection scheme is available at our GitHub repository [25].

The controlling hardware enclosure was made using a short part of a wall-mounting cable raceway (Fig. 4) on which the holes were drilled for cable connectors. On one end the enclosure is covered with the front plate incorporating the power and error LEDs and the manual switch to override the limit switches. On the other end it is covered with the rear plate on which the RPi, the power switch, the power connector and a 24 V cooling fan are mounted. The plates are our own design and were manufactured in-house using a FDM 3D printer.

Table 1. *The cost of the controlling system upgrade*

Component	Quantity	Cost [€]
Raspberry Pi 3 B+	1	39.03
HDMI cable	1.5 m	4.99
micro SD card 32GB	1	16.90
multi-pin screw-in connectors	5	7.03
Custom connection PCB	1	10.60
MCP 6002 ADC IC	1	0.32
Baart board	1	20.95
IRM-30-5 PSU	1	13.62
IRM-60-24 PSU	1	15.61
Fan 24V	1	5.25
other small components	approx.	25.00
	Total:	159.30

The cost of the control-system upgrade was approximately 160 € (Table 1). In comparison to other

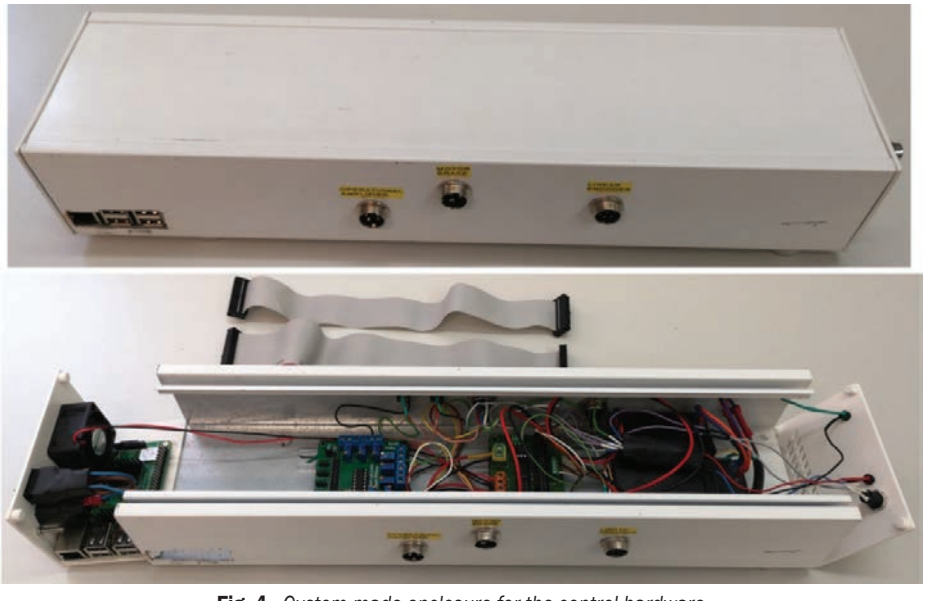

Fig. 4. *Custom-made enclosure for the control hardware*

commercially available equipment (i.e., NI modules) which can cost €1000 or more each [26], we can easily claim that our proposed upgrade is at least 80 % less costly and affordable to most researchers in the field of small-scale, non-commercial tensile testing.

1.5 Software Setup of Proposed Upgrade

The operating system is based on a Raspbian Stretch Lite install (Version: April 2019, Release date: 2019-04-08) [27], using the latest testing branch repository and a Real Time kernel (4.14.y-RT) [28]. Every system service not needed for the operation has either been removed or disabled in the system software. The controlling software is run on the command line using different command arguments for every protocol implemented (Fig. 5) and the appropriate action commences.

The controlling software is written in C++ and the source code is open and available at GitHub [25]. For GPIO control the Pigpio library [29] is used. The program consists of three main functions: encoder reading, ADC reading and motor control, each running in its own thread. The functions are then interconnected. Another important part of the program is the data saving and processing.

1.5.1 Encoder Reading

The resolution of the magnetic encoder ELGO 23 [12] is 1 µm when four-edge triggering is used. At the maximum motor speed of 95 mm/s, 95,000 pulses/s must be sampled and processed to measure the correct distance. For this purpose, one processor thread is dedicated to acquiring signals from the encoder at all times. A call-back function with four-edge triggering is implemented, so every time the state of a pin changes, the function is triggered and the position is either incremented or decremented. To keep the software code simple, we did not monitor the Z signal of the encoder, which is used as a 2 mm reference index and is not crucial for distance measurements.

1.5.2 Load-Cell Reading

The load-cell primary sensor is a Wheatstone bridge consisting of four resistive strain gauges [10], which requires its signal to be amplified by a load-cell amplifier [11]. The amplified signal range is between 0 and 10 V and is sampled by the ADC. An SPI reading function is implemented, which sends the appropriate bits for reading each channel and reads the result [19]. After all the required channels are read, it enters

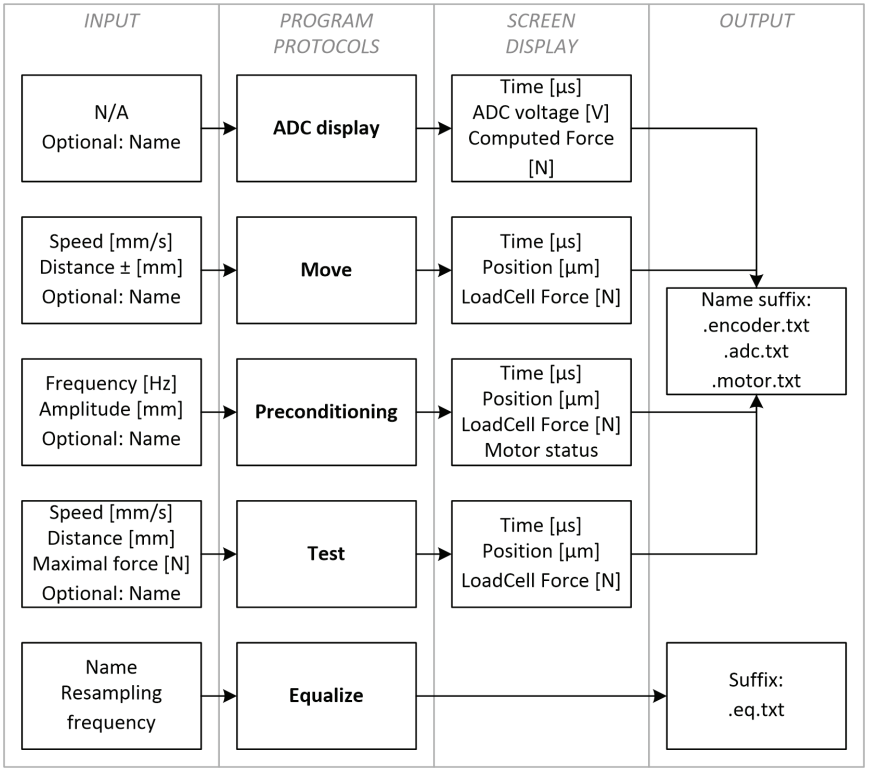

Fig. 5. *Schematics of the implemented protocols*

the sleep mode for a predetermined amount of time (~101 μs) repeating the cycle. Two variants of the function are implemented: one only for reading and another that signals the motor to stop if the maximum predetermined force is reached or exceeded. The latter includes an additional check of whether the force reaches or exceeds this value in any three non-consecutive samples, to avoid premature signaling due to signal noise.

1.5.3 Motor Control

A pulse/direction protocol is used to control the motion of the motor. For this purpose, a square wave must be sent to the motor controller for every step of the motor. The speed of the motor is controlled by the frequency of the pulses. The shortest pulse the stepper driver can receive is 5 μs (2.5 μs up, 2.5 μs down) defining the maximum pulse frequency of 200 kHz.

Toggling the RPi GPIO outputs at those frequencies, while maintaining an equally spaced square wave, has proven difficult to achieve consistently. To solve this problem, the built-in hardware pulse width modulation (PWM) was used because it can achieve much higher signal frequencies and is very accurate, as far as the frequency and duty cycle are concerned. This is very important for correct control of the motor speed.

Two operating modes for the motor control were developed: PWM mode and Pulse mode. The PWM mode for motor control is used when an accurate frequency and duty cycle is required. The Pulse mode for the motor control is intended for accurate positioning.

In PWM mode, the PWM hardware on the RPi is used and the duration is calculated. For the duration, the sleep function is used, and the CPU is free to perform other tasks. It also takes some time to switch the PWM ON and OFF. Because of this, the system can overshoot by a few pulses (<10 pulses equaling <0.01 mm on full scale or <0.01 %). In Pulse mode, we generate the square wave signal in software using busy loops in between. However, the frequency and duty-cycle stability of this mode are not very high as it can occasionally miss the frequency by up to 10 %.

1.5.4 Data Saving and Processing

Because the data-acquisition system runs on the RPi's Operating System (OS), the sample times are not equally spaced. In this configuration, the samples are approximately 250 μs apart, but the tests show that the actual interval can range from 200 μs to 300 μs. The samples from the ADC, encoder and motor are also not sampled at the exact same time. To remedy this design limitation, a data-processing protocol called "Equalize" was implemented.

The "Equalize" protocol takes the data from the measurement files and produces a new file suffixed by ".eq.txt" containing equally spaced time-series data from all three files. This works by taking the latest available sample before each time step while discarding all the other samples in between **[25]**. A time step of 1000 μs proved to be a reliable choice, producing stable results.

1.6 Validation of Upgraded System

To validate the proposed system upgrade, tensile-testing measurements were conducted on our device and on the reference device, the Instron 8802 system **[30]**. The protocols (Table 2) consisted of 5 loading and unloading cycles, triangularly shaped (Figs. 6, 7 and 8), using a metal tension spring after pre-tensioning it to a load of 50 N.

Table 2. *Validation protocol parameters*

Speed [mm/s]	Distance [mm]	Frequency [Hz]
5	10	0.2500
	50	0.0500
	75	0.0333
10	10	0.5000
	50	0.1000
	75	0.0666
25	10	1.2500
	50	0.2500
	75	0.1666
50	10	2.5000
	50	0.5000
	75	0.3333

The results of all the tensile tests were then compared and evaluated. Measurement of the maximum speed and displacement of our device were also conducted to determine the limits of its capabilities. The load cell used on our device had a range of 200 kg and the one on the Instron 8802 had a range of 1 kN.

2 RESULTS

The results of the comparison between our device and the Instron 8802 are shown in Figs. 6 to 9. The left Y axis shows the tensile force from the load cell and the right axis shows the displacement of the tensile

testing head measured by the linear encoder. For representation purposes, all the charts (Figs. 6, 7 and 8) have the same scale on all three axes.

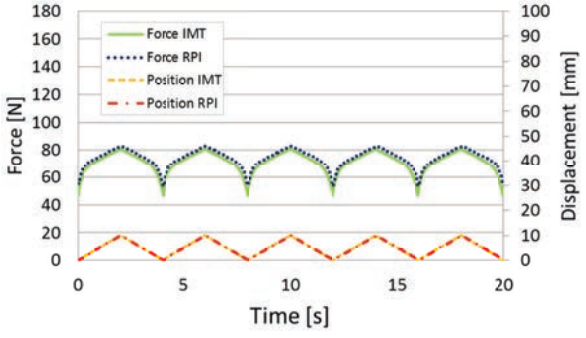

Fig. 6. *Comparison of Instron 8802 (IMT) and our device (RPi) at a distance of 10 mm and a frequency of 0.25 Hz*

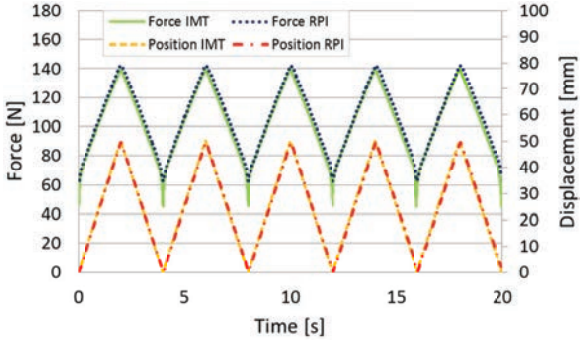

Fig. 7. *Comparison of Instron 8802 (IMT) and our device (RPi) at a distance of 50 mm and a frequency of 0.25 Hz*

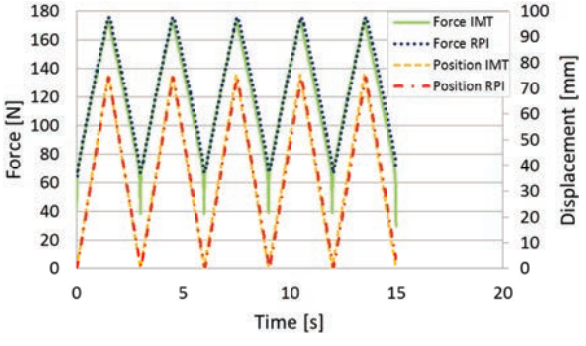

Fig. 8. *Comparison of Instron 8802 (IMT) and our device (RPi) at a distance of 75 mm and a frequency of 0.333 Hz*

The measured force from the Instron 8802 (IMT) and our device (RPi) shows a small difference of around 6 N, which is constant throughout the whole protocol. The difference is a result of the inaccurate pre-tensioning of the spring before the protocol on each device.

After the data acquisition the measured force from our device was filtered using a 10 Hz low-pass filter to exclude the spikes that occurred due to sampling the load cell with a greater measuring range than the one on the Instron 8802 **[30]**.

The force and displacement-response differences in time is minimal, but occurs due to the "soft-start" option on motor controller, which limits the starting acceleration of the stepper motor to reduce the wear on the motor and other hardware of the tensile device. The "Soft-start" option could be turned off, resulting in a much slower maximum speed of the tensile device and higher wear on the stepper motor.

All the measurements also showed similar characteristics of the metal spring (Fig. 9), which also reflects in a very high Pearson correlation coefficient (Table 3).

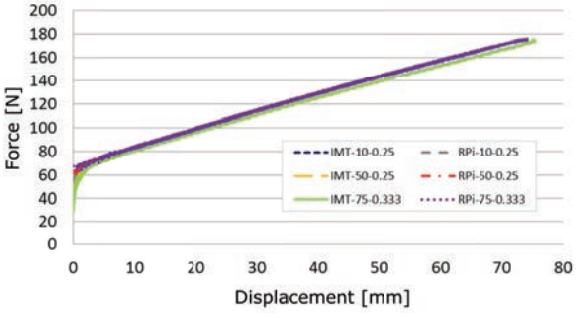

Fig. 9. *Characteristics of the metal spring at three different protocols*

Table 3. *Pearson coefficient for measurements shown in previous graphs*

	10 mm, 0.25 Hz	50 mm, 0.25 Hz	75 mm, 0.333 Hz
Pearson correlation	0.99337	0.99531	0.99018

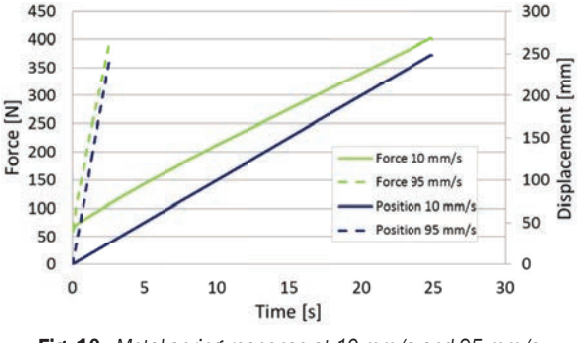

Fig. 10. *Metal spring response at 10 mm/s and 95 mm/s loading speed for a distance of 250 mm*

Using the same spring, a full-range tensile test was also conducted (Fig. 10) at slow speed (10 mm/s) and at the maximum device speed (95 mm/s). Both

measurements show the same force-displacement response of the spring (Fig. 11).

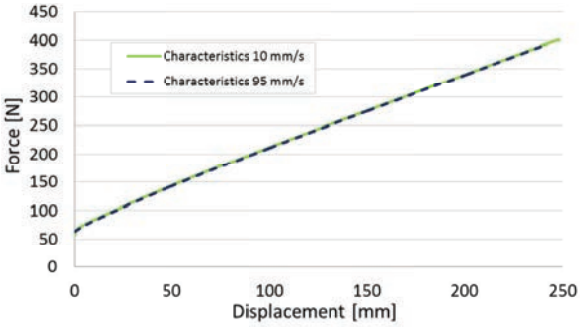

Fig. 11. *Metal spring "force-displacement" response at two different loading speeds*

3 DISCUSSION AND CONCLUSIONS

The principal purpose of the presented research and development was to test whether the principles of designing low-cost data-acquisition systems can be applied to a somewhat more complex system for tensile testing. The design of the system was adopted from the existing tensile-testing machine, which has proven problematic from the usability and durability point of view. The reasoning behind the component selection was to integrate a system that will provide the same level of measurement accuracy for an affordable price. This was the reason for selecting the low-cost off-the-shelf hardware and the development of own software using previously acquired experience.

The resulting system is a well-balanced compromise between invested resources and the quality of the resulting product. Using our product, we managed to control the whole tensile testing system with enough speed and accuracy to use it for the experimental testing of soft tissues. We successfully replaced the expensive and unreliable existing control equipment with low-cost hardware running open-source software developed in-house.

The results from the comparison of our custom-built tensile-testing device with the upgraded controlling system and a commercially available certified Instron 8802 tensile-testing device show that our device can produce comparable results and is sufficiently accurate to be used for research purposes. The typical dynamic tests of a steel tensile spring, conducted on both systems, yielded results with a Pearson correlation over 99 %.

The upgraded system is currently being used for acquiring the material properties of samples of post-mortem human ligament tissues. Although the application is currently limited to a single purpose, the controlling and data-acquisition system can be easily utilized for other types of measurements or be transferred to another mechanical system.

Compared to the available turn-key solutions, our system did take more time to design and develop, yet it is more versatile, less costly and easily adaptable, while maintaining a comparable level of accuracy. The development of the presented system also enriched our expertise in this field, which has encouraged us to consider upgrading or developing future measurement systems in a similar manner.

4 ACKNOWLEDGMENTS

This research was funded by the Slovenian Research Agency (ARRS) as part of the Young Researcher Programme for the P2-0109 Research Programme.

5 REFERENCES

[1] Foster, S.W., Alirangues, M.J., Naese, J.A., Constans, E., Grinias, J.P. (2019). A low-cost, open-source digital stripchart recorder for chromatographic detectors using a Raspberry Pi. *Journal of Chromatography A*, vol. 1603, p. 396-400, **DOI:10.1016/j.chroma.2019.03.070**.

[2] Kuziek, J.W.P., Shienh, A., Mathewson, K.E. (2017). Transitioning EEG experiments away from the laboratory using a Raspberry Pi 2. *Journal of Neuroscience Methods*, vol. 277, p. 75-82, **DOI:10.1016/j.jneumeth.2016.11.013**.

[3] Kirby, J., Chapman, L., Chapman, V. (2018). Assessing the Raspberry Pi as a low-cost alternative for acquisition of near infrared hemispherical digital imagery. *Agricultural and Forest Meteorology*, vol. 259, p. 232-239, **DOI:10.1016/j.agrformet.2018.05.004**.

[4] Ambrož, M. (2017). Raspberry Pi as a low-cost data acquisition system for human powered vehicles. *Measurement*, vol. 100, p. 7-18, **DOI:10.1016/j.measurement.2016.12.037**.

[5] Bosch Rexroth standard aluminum framing system, from *https://www.boschrexroth.com/en/xc/products/product-groups/assembly-technology/topics/aluminum-profiles-solutions-components/aluminum-profiles-products/index*, accessed on 2019-07-11.

[6] Berger Lahr stepper motor, from *https://www.schneider-electric.com/en/download/document/0098441113309/*, accessed on 2019-07-11.

[7] Bosch Rexroth linear compact module, from *https://www.boschrexroth.com/en/us/products/product-groups/goto-products/goto-linear-motion/ckk-and-ckr-compact-modules/index*, accessed on 2019-07-11.

[8] Schneider electric gearbox, from *https://www.schneider-electric.com/en/product/GBX080003K/gearbox-straight-teeth-gbx---%C3%B8-80-mm---reduction-3%3A1-%3C-7-arc.min---85-n.m/*, accessed on 2019-07-11.

[9] Berger Lahr motion control stepper motor drive, from *https://www.schneider-electric.com/en/product/SD326RU68S2/*

motion-control-stepper-motor-drive---sd326---pulse-direction---%3C%3D-6.8-a/, accessed on 2019-07-11.

[10] AEP transducers tensile-compression load cell, from *http://www.aeptransducers.com/load-cells/82-ts.html*, accessed on 2019-07-11.

[11] AEP transducers analogue transmitter, from *http://www.aeptransducers.com/instruments/164-ta4-2.html*, accessed on 2019-07-11.

[12] Elgo magnetic linear encoder, from *https://www.elgo.de/en/products/measuring-systems/linear-measurement-incremental/emix23/*, accessed on 2019-07-11.

[13] Stojanović, A., Omerović, S., Krašna, S., Prebil, I. (2012). Mechanical properties of human cervical spine ligaments: Age related changes. *Journal of Biomechanics*, vol. 45, no. 1, p. S611, **DOI:10.1016/S0021-9290(12)70612-7**.

[14] National instruments motion controller NI PCI-7324, from *http://www.ni.com/pdf/manuals/322503b.pdf*, accessed on 2019-07-11.

[15] National instruments USB multifunction I/O device NI USB-6221, from *http://www.ni.com/sl-si/support/model.usb-6221.html*, accessed on 2019-07-11.

[16] Power over net HAT, from *https://www.raspberrypi.org/products/poe-hat/*, accessed on 2019-07-11.

[17] Raspberry Pi 3 B+ specifications, from *https://static.raspberrypi.org/files/product-briefs/Raspberry-Pi-Model-Bplus-Product-Brief.pdf*, accessed on 2019-07-11.

[18] Efftek ADC Baart board, from *https://www.raspberrypi.org/forums/viewtopic.php?f=93&t=132508&p=883282&hilit=adc+board#p883282*, accessed on 2019-07-11.

[19] Microchip Technology MCP 3208, from *https://www.microchip.com/wwwproducts/en/MCP3208*, accessed on 2019-07-11.

[20] Raspberry Pi GPIO overview, from *https://www.raspberrypi.org/documentation/hardware/raspberrypi/gpio/README.md*, accessed on 2019-07-11.

[21] Electrical specifications of GPIO pins on Raspberry Pi, from *https://raspberrypi.stackexchange.com/questions/60218/what-are-the-electrical-specifications-of-gpio-pins/60219#60219*, accessed on 2019-07-11.

[22] Microchip technology MCP6002, from *https://www.microchip.com/wwwproducts/en/MCP6002*, accessed on 2019-07-11.

[23] Mean Well 24V AC/DC power supply, from *http://www.meanwellusa.com/webapp/product/search.aspx?prod=IRM-60*, accessed on 2019-07-11.

[24] Mean Well 5V AC/DC power supply, from *http://www.meanwellusa.com/webapp/product/search.aspx?prod=IRM-30*, accessed on 2019-07-11.

[25] Controlling equipment source code "trgalnik", FSKMTM GitHub repository, from *https://github.com/FSKMTM/trgalnik*, accessed on 2019-10-28.

[26] National Instruments Multifunction modules – shop, from *http://www.ni.com/en-us/shop/select/multifunction-io-category#facet:&productBeginIndex:0&orderBy:&pageView:grid&pageSize:&*, accessed on 2019-07-11.

[27] Raspbian Stretch Lite: Version: April 2019 Release date: 2019-04-08), from *https://www.raspberrypi.org/downloads/raspbian/*, accessed on 2019-07-11.

[28] Real Time kernel 4.14.y-RT, from *https://github.com/raspberrypi/linux/tree/rpi-4.14.y-rt*, accessed on 2019-07-11.

[29] Pigpio library, from *http://abyz.me.uk/rpi/pigpio/*, accessed on 2019-07-11.

[30] Instron 8802 Fatigue testing system, from *https://www.instron.us/en-us/products/testing-systems/dynamic-and-fatigue-systems/servohydraulic-fatigue/8802*, accessed on 2019-07-11.

6 APPENDIX

Supplementary material consisting of measurement results, protocol, data saving and processing descriptions, source code and the connection scheme of the whole system is available at our GitHub repository: https://github.com/FSKMTM/trgalnik

Strojniški vestnik - Journal of Mechanical Engineering 66(2020)3, 164-174

DOI:10.5545/sv-jme.2019.6283 Original Scientific Paper
Received for review: 2019-08-09
Received revised form: 2019-12-09
Accepted for publication: 2020-01-22

Dynamic Characteristics and Stability Prediction of Steam Turbine Rotor Based on Mesh Deformation

Heyong Si* – Lihua Cao – Pan Li
Northeast Electric Power University, Department of Energy and Power Engineering, China

In order to study the steam flow excited vibration caused by the eccentricity of a rotor, three-dimensional rotor whirl motion is simulated based on mesh deformation. The mechanism of steam flow excited vibration and its influence on the dynamic characteristics of the rotor are investigated. The results show that the exciting forces change with the displacement of the rotor's centre. Rotor dynamic coefficients are nonlinear when the rotor whirls pass the mesh deformation. The rotor dynamic coefficients and effective damping increase with the increase of whirl frequency. When the whirl frequency is 24.41 Hz, the rotor dynamic coefficients are strongly affected by rotational velocity. The maximum fluctuations of average direct stiffness, cross-coupling stiffness, direct damping and cross-coupling damping are 8.1 %, 113.2 %, 45.8 %, and 121.0 %, respectively. Effective damping fluctuates greatly when both whirl and rotational frequency are 24.41 Hz. The direct stiffness, direct damping, and effective damping increase with the increase of pressure ratio, which can improve rotor stability. The pressure fluctuation on the rotor's surface is a primary reason for steam flow excited vibration. The stability margin of the rotor can be estimated precisely via effective damping.

Keywords: steam turbine; labyrinth seal; steam flow excited vibration; rotor dynamic characteristics; mesh deformation; stability

Highlights

- *The three-dimensional rotor whirl motion was simulated based on the mesh deformation.*
- *The mechanism of steam flow excited vibration and the influence of factors on the dynamic characteristics of the rotor were investigated.*
- *The stability of the rotor can be predicted precisely through effective damping.*

0 INTRODUCTION

With the continuous growth of power demand and the adjustment of industrial energy structures, steam turbines with large capacities are widely used in power generation. Steam flow plays an essential role in rotor stability. The uneven circumferential clearance in a seal caused by the eccentricity of the rotor will lead to the uneven distribution of steam, which easily induces steam flow excited vibration. This is the main reason for the variation of rotor dynamic characteristics and rotor instability. Therefore, the analysis of rotor dynamic characteristics and the stability of the rotor system including steam flow excited vibration are necessary.

In Alford's analysis of steam flow exciting forces, the uneven force on rotor produced by steam can easily cause the eccentricity of the rotor, which results in circumferential uneven leakage flow and continuously aggravates the whirl motion of rotor [1]. To analyse the mechanism of steam exciting force, many different computational models of seal have been used by scholars [2] to [6]. With the deepening of research, the computational models of seal for steam flow exciting forces are constantly improved [7] and [8]. In recent years, computational fluid dynamics (CFD) has been widely used for simulations of fluid flow, combustion, and chemical reactions due to its fast and effective computational model. The static eccentricity of a rotor model is calculated with a steady-state solver, in which the rotor only has rotational motion. The results show that the radial and tangential steam flow exciting forces on rotor increase with the increase of eccentricity [9] and [10]. The rotor dynamic coefficients have a nonlinear relationship with the eccentricity. With the increase of positive prewhirl at seal inlet, the cross-coupling stiffness increases gradually from negative to positive, and the rotor system is unstable [11]. However, a proper reverse prewhirl can enhance the rotor stability [12] and [13]. Based on the influences of preswirl and circumferential movement of steam flow on rotor stability, the damping seal proposed by von Pragenau is applied to practice. The seal can reduce circumferential non-uniform distribution of pressure and cross-coupling stiffness, which can enhance the rotor stability [14].

Based on the static eccentricity of the rotor model, the rotor whirl motion relative to rotating coordinate system is put forward. In this model, the stator and rotor have opposite rotational motion at the same time. Ishii et al. simulated the complex turbulent flow field of the seal to verify the validity of the model, and indicated that the accurate flow field near the teeth

*Corr. Author's Address: Northeast Electric Power University, Department of Energy and Power Engineering, Jilin 132012, China, ssiheyong0927@163.com

is necessary for evaluating the rotor dynamic forces [15]. Other scholars conducted a comparative analysis of different solvers via this model and indicated that CFX-TASC flow can accurately calculate the rotor dynamic coefficients [16]. Sivakumar Subramanian et al. studied the influence of centrifugal force on the radial exciting force and tangential exciting force. The centrifugal effect at low rotational velocity decreases the radial exciting force, which is more obvious when the pressure ratio increases; the tangential exciting force is almost constant. However, at the condition of high rotational velocity and high-pressure ratio, the radial and tangential exciting forces change sharply with the centrifugal effect [17]. Scholars established the rotor whirl model for gas turbines and calculated the dynamic coefficients in the frequency domain [18]. In addition, the instability in compressors can be linked to the high structural stress, which are associated with flow-induced blade vibrations. The research on the long-blade turbine stage showed that the frequency of separation vortex had a certain influence on the steam flow excited vibration [19]. In the research on rotor nonlinear motion [20], Ma et al. studied the bifurcation of rotor system and found that the bigger seal diameter, the higher bifurcation velocity of rotor system [21].

At present, simplified models are adopted in most of the research in order to reduce the computational time, such as the static eccentricity of the rotor and the rotor whirl motion based on the relative rotating coordinate. However, these models can only show the forces and flow characteristics at a certain position of rotor. The flow field analysis under the condition of rotor whirl is ignored. Furthermore, the result from the simplified dynamic coefficients equation by duality is not accurate enough. Therefore, based on the structure of the diaphragm seal, the computational fluid dynamics software is applied to establish a three-dimensional rotor whirl model. The mesh deformation is used to simulate the real rotor whirl. The influences of whirl frequency, rotational velocity, whirl radius and pressure ratio on the steam flow excited vibration are considered to solve the rotor dynamic coefficients. At the same time, the rotor stability of steam turbine is analysed. The structure of the paper and the relative contents of sections are shown as Fig. 1.

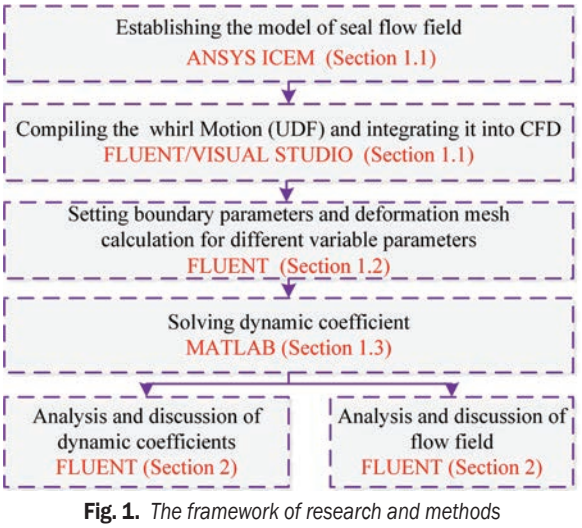

Fig. 1. *The framework of research and methods*

1 NUMERICAL MODEL AND METHODS

1.1 Computational Model

Taking a second stage diaphragm seal in a high-pressure cylinder of 300 MW steam turbine as an example, the three-dimensional full-cycle rotor whirl model is established. The unstructured grid is generated by ANSYS ICEM, and the unsteady flow field in seal is calculated with a FLUENT pressure solver. The seal model is shown in Fig. 2. The cavity depth, teeth thickness, convex plate height, and seal tip clearance are represented by h, t, l and C_r, respectively. The specific structural parameters are shown in Table 1.

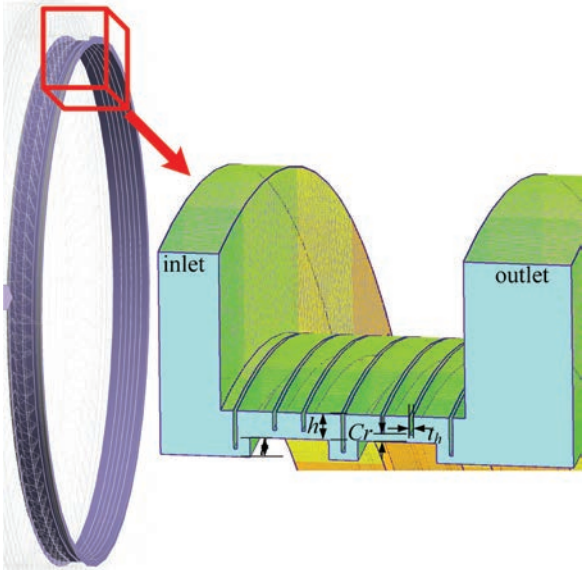

Fig. 2. *Schematic diagram of labyrinth seal structure*

A single-frequency rotor whirl model is constructed at one whirl velocity, as shown in Fig. 3. Orbit 1 is an example of single-frequency rotor whirl motion. The expression of motion in the forward direction is as follows:

$$\dot{x}(t) = -e \times \Omega \times \cos(\theta_0 + \Omega \times t), \quad (1)$$

$$\dot{y}(t) = e \times \Omega \times \sin(\theta_0 + \Omega \times t), \quad (2)$$

where e is the whirl radius of the rotor; $\dot{x}(t)$ is the velocity of the x direction; $\dot{y}(t)$ is the velocity of the y direction; Ω is the whirl velocity; θ_0 is the initial angle; t is the time.

Table 1. *Structural parameters of labyrinth seal*

Name	Value	unit
Cavity depth, h	3.2	mm
Teeth thickness, t	0.4	mm
Convex plate height, l	2.4	mm
Seal tip clearance, Cr	1	mm
Rotor diameter	496.6	mm

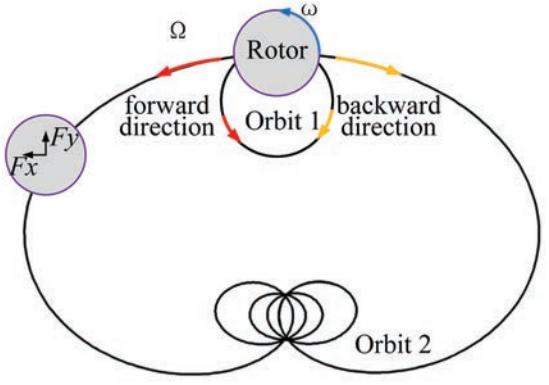

Fig. 3. *Schematic diagram of whirl motion*

The multi-frequency rotor whirl model is obtained from the improvement of single-frequency rotor whirl model, as shown in Fig. 3. Orbit 2 is an example of multi-frequency rotor whirl motion. The expression of the forward direction is as follows:

$$\dot{x}(t) = -e \times \sum \Omega_i \times \cos(\theta_0 + \Omega_i \times t), \quad (3)$$

$$\dot{y}(t) = e \times \sum \Omega_i \times \sin(\theta_0 + \Omega_i \times t), \quad (4)$$

where i is the whirl velocity which has five values (750, 1500, 2250, 3000, 3750) r/min.

1.2 Mesh Deformation Method

As the boundary profile of the model will be changed by the whirl of rotor, the defined function is compiled with a user-defined function (UDF) to command the motion of boundary, and mesh deformation is used to the computational domain. Thus, the three-dimensional whirl motion of the rotor is achieved. The main structure of UDF is shown in Fig. 4, in which the control function of the rotor is DEFINE_CG_MOTION.

```
#include "udf.h"
#pragma comment(lib, "kernel32.lib")//Invoking
function
#define PI 3.1415926
DEFINE_CG_MOTION(rotor,dt,vel,omega,time,dtime)
{
        real  ***;//Parameters
        NV_S(vel,=,0.0);
        NV_S(omega,=,0.0);//Initialization
        real  ***;//Assignment
        Formula calculation
            Output
}
```

Fig. 4. *Main structure of UDF program*

The boundary parameters are derived from the rated operating conditions of the unit. The pressure boundary is applied to the inlet and outlet, the inlet pressure is 10.7 MPa and the inlet temperature is 744.25 K, the outlet pressure is 10.263 MPa and the outlet temperature is 734.25 K. The N-S equation in labyrinth seal flow field is solved by the standard k–ε equation with the SIMPLE algorithm. Because the mesh can be updated and reconstructed, the high quality of the initial mesh and suitable mesh updating are necessary. The initial mesh number under the condition of static eccentricity is shown in Table 2. There is no significant influence on the results when the grid number reaches 5.4 million.

Table 2. *Influence of mesh quantity on results*

Mesh number(×10⁴)	F_x	F_y
270	–11.1223	22.2852
300	–16.9572	17.9165
410	–13.7212	36.0879
540	–13.6620	36.2510
720	–13.6460	36.2544

Table 3. *Specific parameters of "Remeshing" and dimension function*

Items	Value
Spring constant	1
Convergence tolerance	0.001
Number of iterations	20
Laplace node relaxation	1
Split factor	0.4
Collapse factor	0.2
Remeshing methods resolution	1
Remeshing Methods variation	0.1
Remeshing methods rate	0.7

The remeshing method of grid updating and dimension function are used; the specific parameters are shown in Table 3. The grids at 0 s and 0.002 s are shown in Fig. 5. Taking a grid element as an example, when the rotor is whirling, rotor displacement appears and the node K on rotor surface moves in the *x* direction. It can be seen from Table 5 that the volume difference of grids between 0 s and 0.002 s is small, so the grids updated by mesh deformation still have high quality.

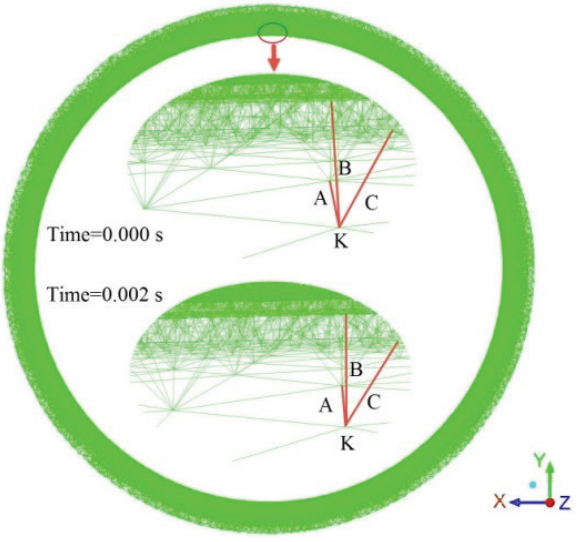

Fig. 5. *Schematic diagram of mesh deformation*

Table 4. *Comparison of mesh deformation*

Grid statistics	t = 0 s	t= 0.002 s
Minimum volume [m³]	3.3922e-13	3.3882e-13
Maximum volume [m³]	1.4430e-07	1.6809e-07
Total volume [m³]	9.3375e-04	9.3375e-04
Minimum face area [m²]	4.2743e-09	4.2743e-09
Maximum face area [m²]	8.0990e-05	8.0970e-05

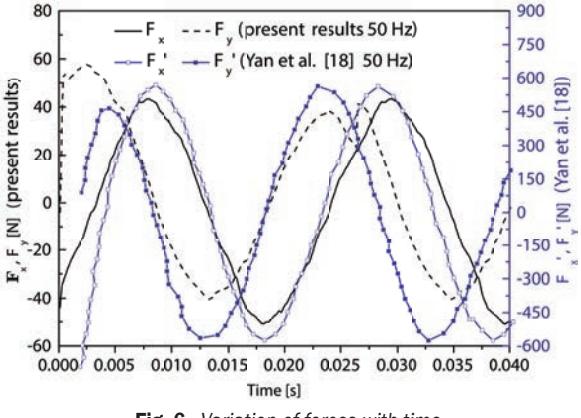

Fig. 6. *Variation of forces with time*

In order to verify the accuracy of the model, a single-frequency whirl model is simulated at 50 Hz. The steam flow exciting forces in *x* and *y* directions is shown in Fig. 6. Compared with the forces of the honeycomb seal in literature [18], they have a very similar variation trend. Therefore, the model established in this paper is reliable.

1.3 Calculation Method of Rotor Dynamic Coefficients

The mathematical relation between the steam flow exciting forces and rotor dynamic coefficients in the labyrinth seal can be represented by the following equation:

$$\begin{bmatrix} F_x(t) \\ F_y(t) \end{bmatrix} = -\begin{bmatrix} k_{xx} & k_{xy} \\ k_{yx} & k_{yy} \end{bmatrix}\begin{bmatrix} x(t) \\ y(t) \end{bmatrix} - \begin{bmatrix} c_{xx} & c_{xy} \\ c_{yx} & c_{yy} \end{bmatrix}\begin{bmatrix} \dot{x}(t) \\ \dot{y}(t) \end{bmatrix}, \quad (5)$$

where $F_x(t)$ and $F_y(t)$ are the component forces in *x* and *y* direction, as shown in Fig. 3. k_{xx} and k_{yy} are the direct stiffness, k_{xy} and k_{yx} are the cross-coupling stiffness, c_{xx} and c_{yy} are the direct damping, c_{xy} and c_{yx} are the cross-coupling damping, $x(t)$ and $y(t)$ are the displacements in the *x* and *y* directions.

The rotor dynamic coefficients are solved according to the solution in [22]. The matrix in Eq. (5) is performed by Fast Fourier transform to obtain the matrix in Eq. (6) in the frequency domain.

$$\begin{bmatrix} -F_x \\ -F_y \end{bmatrix} = \begin{bmatrix} k_{xx} + j\Omega c_{xx} & k_{xy} + j\Omega c_{xy} \\ k_{yx} + j\Omega c_{yx} & k_{yy} + j\Omega c_{yy} \end{bmatrix}\begin{bmatrix} d_x \\ d_y \end{bmatrix}. \quad (6)$$

In order to distinguish the forward and backward motions, the forward whirl motion and backward whirl motion are defined as *a* and *b*, respectively. For each group of whirl motion, there is the following matrix:

$$\begin{bmatrix} -F_{ax} & -F_{bx} \\ -F_{ay} & -F_{by} \end{bmatrix} = \begin{bmatrix} k_{xx} + j\Omega c_{xx} & k_{xy} + j\Omega c_{xy} \\ k_{yx} + j\Omega c_{yx} & k_{yy} + j\Omega c_{yy} \end{bmatrix}\begin{bmatrix} d_{ax} & d_{bx} \\ d_{ay} & d_{by} \end{bmatrix}. \quad (7)$$

Therefore, the dynamic coefficients can be expressed in the following equations. The real parts and the imaginary parts in Eqs. (8) to (11) are the rotor dynamic coefficients.

$$k_{xx} + j\Omega c_{xx} = \frac{(-F_{ax})d_{by} - (-F_{bx})d_{ay}}{d_{ax}d_{by} - d_{bx}d_{ay}}, \quad (8)$$

$$k_{xy} + j\Omega c_{xy} = \frac{(-F_{ax})d_{bx} - (-F_{bx})d_{ax}}{d_{ay}d_{bx} - d_{by}d_{ax}}, \quad (9)$$

$$k_{yx} + j\Omega c_{yx} = \frac{(-F_{by})d_{ay} - (-F_{ay})d_{by}}{d_{ay}d_{bx} - d_{by}d_{ax}}, \quad (10)$$

$$k_{yy} + j\Omega c_{yy} = \frac{\left(-F_{by}\right)d_{ax} - \left(-F_{ay}\right)d_{bx}}{d_{by}d_{ax} - d_{bx}d_{ay}}. \qquad (11)$$

2 RESULTS AND ANALYSIS

Based on the multi-frequency whirl model and solution method of dynamic coefficients, the influences of whirl radius, whirl frequency, rotational velocity and pressure ratio on rotor dynamic characteristics have been researched. The quantitative relationship among them is also studied. Specific calculation parameters are shown in Table 5.

Table 5. *Calculation parameters*

Name	Value	unit
Whirl frequency	12.5, 25, 37.5, 50, 62.5	Hz
Whirl radius	0.05, 0.075, 0.10	mm
Rotational velocity	750, 1500, 3000	r/min
Pressure ratio	1.04, 1.06, 1.08	-

The displacements and steam flow exciting forces of the rotor are calculated when the whirl radius is 0.05 mm, the rotational velocity is 3000 r/min, and the pressure ratio is 1.04, as shown in Fig. 7. Both the displacements and steam flow exciting forces have nonlinear variations in the time domain. The variations of displacement and steam-exciting force in the *x* direction are in good agreement, and also in the *y* direction. Compared with the static eccentric model, the mesh deformation has more practical significance because it can realize actual whirl motion. In the frequency domain, the displacement amplitudes corresponding to whirl frequencies are high and the amplitudes of steam flow exciting forces increase with the increase of whirl frequency.

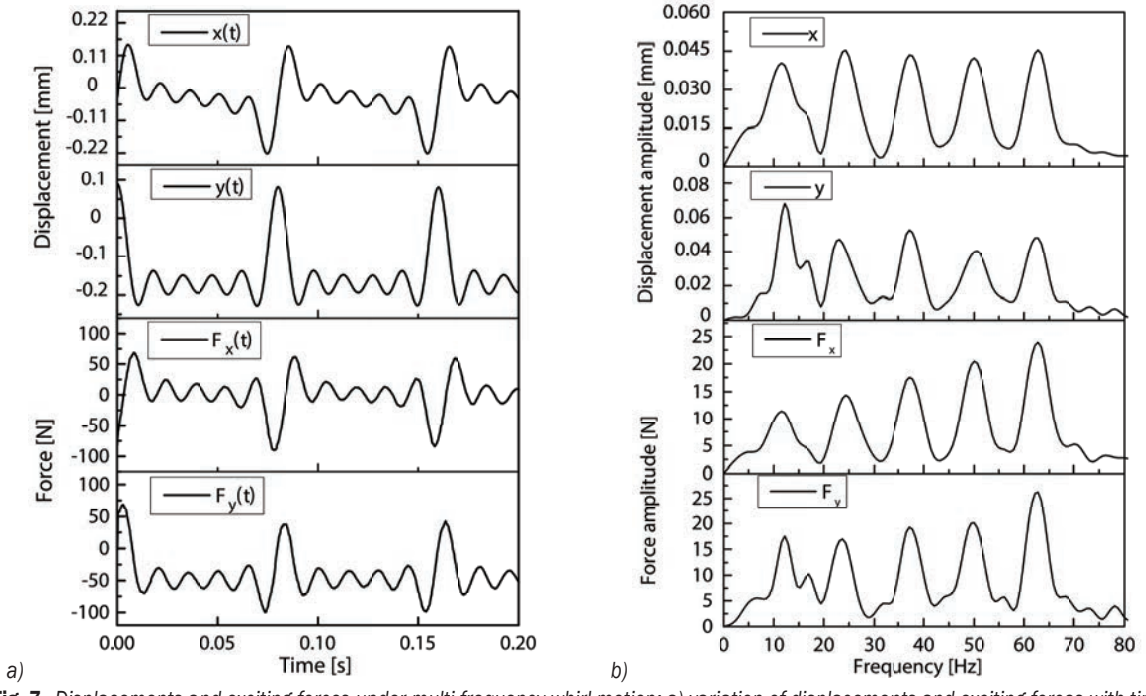

Fig. 7. *Displacements and exciting forces under multi-frequency whirl motion; a) variation of displacements and exciting forces with time, and b) variation of displacements and exciting forces with frequency*

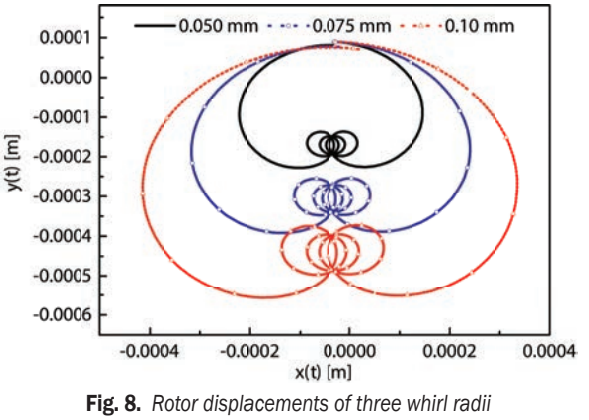

Fig. 8. *Rotor displacements of three whirl radii*

The rotor dynamic coefficients are calculated in three different whirl radiuses. The three whirl orbits are shown in Fig. 8, and the influence of whirl radius on rotor dynamic coefficients is shown in Fig. 9.

It can be seen that the rotor dynamic coefficients present evident nonlinear variation in the multi-frequency whirl motion. With the increase of whirl frequency, the dynamic coefficients present an increasing trend with fluctuation. When the whirl radius grows, the direct stiffness, cross-coupling stiffness, and cross-coupling damping in the *xy* direction can hardly match themselves in the *yx* direction. The direct damping increases with the increase of whirl frequency. With the increase of whirl radius, the direct stiffness, cross-coupling stiffness, and cross-coupling damping change obviously but without regularity. Furthermore, they have the approximate trend of trigonometric function under the large whirl radius. Comparing the direct stiffness 0.05 mm with 0.1 mm, it can be determined that the direct stiffness increases with the increase of whirl radius, while the direct damping is less affected by the whirl radius. The duality of dynamic coefficients is used in most studies to simplify the calculation equations, namely, $k_{xx}=k_{yy}$, $c_{xx}=c_{yy}$, $k_{xy}=-k_{yx}$, $c_{xy}=-c_{yx}$. In this research, however, the duality is not applicable to the dynamic coefficients except the direct damping. Therefore, in the research of rotor dynamic coefficients for a steam turbine, the results obtained by the simplified equation based on the duality are not accurate enough.

Fig. 10 shows the rotor dynamic coefficients under different rotational velocity. The variation of coefficients is similar to the above analysis, but the rotational velocity also has a great influence on the rotor dynamic coefficients. The dynamic coefficients fluctuate considerably under different rotational velocity when the whirl frequency is near 24.41 Hz. It is shown in Fig. 10 that the rotational velocity has a significant effect on the direct damping in the low-frequency range and this effect decreases gradually with the increase of frequency. The direct damping decreases at exactly 24.41 Hz when the rotational velocity is 1500 r/min. This is because the rotational velocity and whirl velocity are both near the first critical velocity, which makes the stability of rotor decreased. The influence between the rotational velocity and whirl velocity is significantly reduced with the increase of whirl frequency, so the variation of direct damping decreases gradually. The average

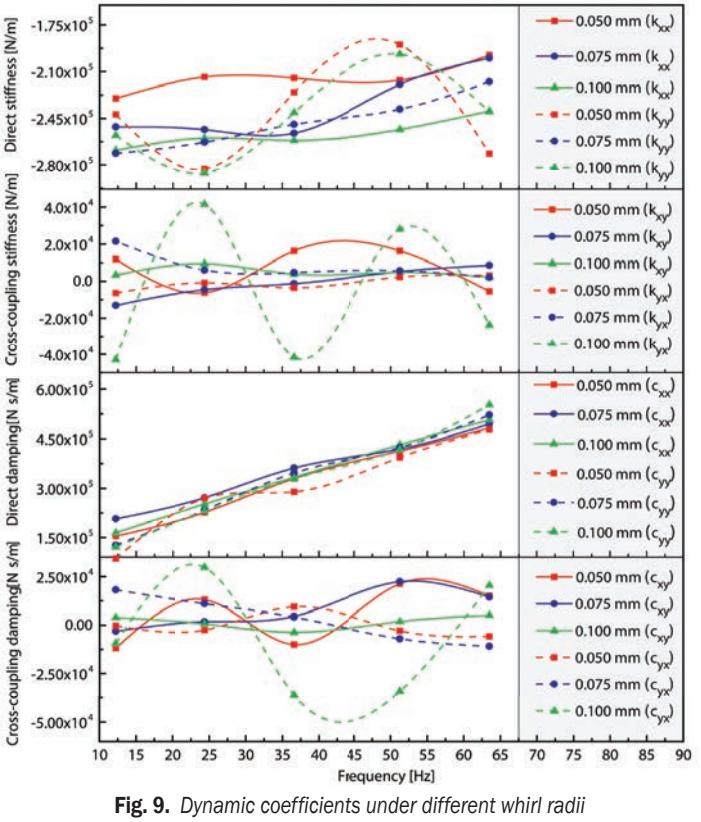

Fig. 9. *Dynamic coefficients under different whirl radii*

direct stiffness, cross-coupling stiffness, direct damping and cross-coupling damping are listed in Table 6, as well as their equations. It can be seen that the rotational velocity of 1500 r/min has the greatest impact on the rotor dynamic coefficients. The maximum fluctuations of average dynamic coefficients are 8.1 %, 113.2 %, 45.8 %, and 121.0 %, respectively.

Fig. 11 shows the variation of rotor dynamic coefficients in different pressure ratios between inlet and outlet. The direct stiffness increases gradually towards the negative direction with the increase of pressure ratio, while the direct damping increases towards the positive direction. The direct stiffness and damping vary with pressure ratio in a hierarchical distribution. According to the rotor dynamics analysis, the increase of direct damping is conducive to the stability of the rotor system and the direct damping increases obviously with the increase of pressure ratio. Therefore, the stability of the rotor system can be improved by increasing the pressure ratio. The variation of cross-coupling stiffness and cross-coupling damping with the increase of pressure ratio is not regular. A comparison of the 1.04 with 1.08 pressure ratio shows that the variation range of cross-coupling stiffness and cross-coupling damping increase as the pressure ratio increases.

The above research shows that the whirl frequency, whirl radius, rotational velocity and pressure ratio have considerable influence on the rotor dynamic coefficients. The effective damping coefficient C_E can reflect the stability margin of the

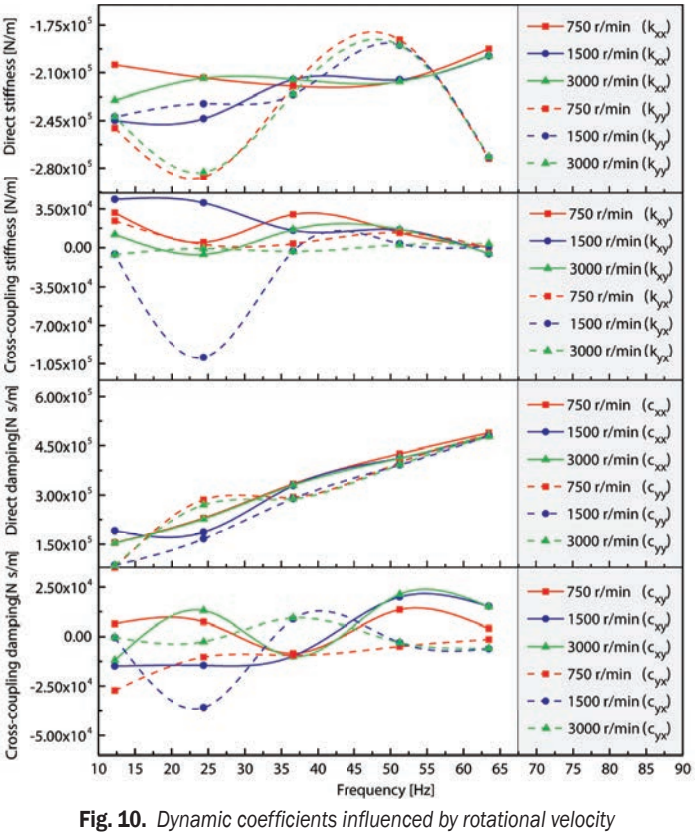

Fig. 10. *Dynamic coefficients influenced by rotational velocity*

Table 6. *Fluctuations of average dynamic coefficients at whirl frequency 24.41 Hz*

Name	Calculation equation	Rotational velocity			Maximum fluctuation [%]
		750 r/min	1500 r/min	3000 r/min	
Average direct stiffness [N/m]	$(k_{xx}+k_{xx})/2$	–250227	–238030	–248539	8.1
Average cross-coupling stiffness [N/m]	$(k_{xy}+k_{yx})/2$	3877	–29329	–3531	113.2
Average direct damping [N·s/m]	$(c_{xx}+c_{xx})/2$	257580	176607	248374	45.8
Average cross-coupling damping [N·s/m]	$(c_{xy}+c_{yx})/2$	–1464	–25224	5289	121.0

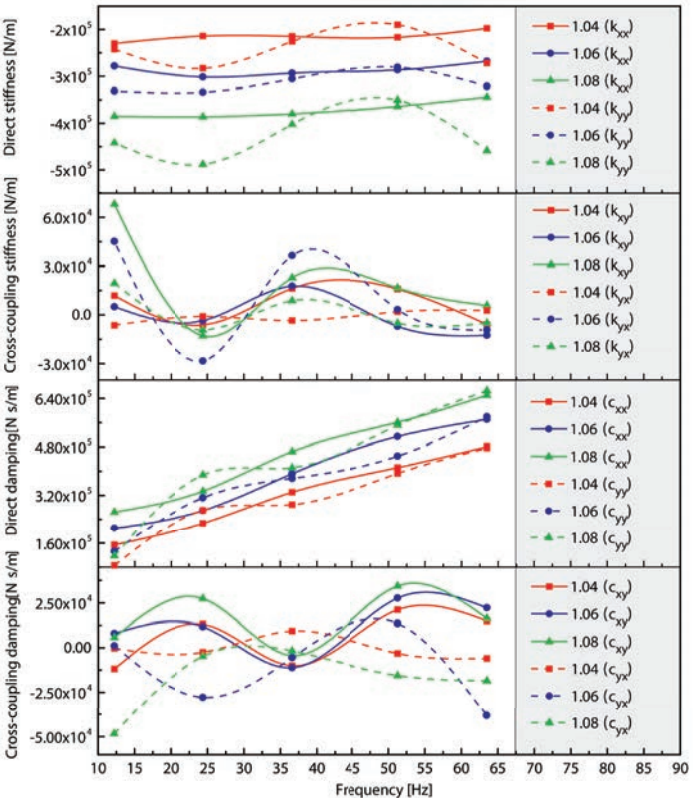

Fig.11. *Influence of pressure ratio on dynamic coefficients*

rotor system. Hence, C_E is used as the evaluation index for the stability of the rotor, as defined below:

$$C_E = \int_0^T \left(F_z \dot{z} + F_y \dot{y}\right) \mathrm{d}t \Big/ 2\pi e^2 \Omega, \tag{12}$$

$$e^2 \pi \left(\left(k_{zy} - k_{yz}\right) - \Omega\left(c_{zz} + c_{yy}\right)\right) = -\int_0^T \left(F_z \dot{z} + F_y \dot{y}\right) \mathrm{d}t, \tag{13}$$

where Ω is whirl velocity. When $C_E > 0$, the higher value is, the more stable rotor system is. When $C_E < 0$, the smaller C_E is, the more possible that the rotor system is unstable.

As shown in Fig. 12, the effective damping of rotor increases with the increase of whirl frequency. It increases slightly with the increase of whirl radius and this trend is not obvious in low frequency range until the whirl frequency exceeds 50 Hz. The relationship between the rotational velocity and the effective damping is shown in Fig. 12. It can be seen that the effective damping of rotor decreases when the rotational velocity is 1500 r/min, and the whirl frequency is 24.41 Hz. When the whirl frequency exceeds 35 Hz, the rotor stability at the 1500 r/min rotational velocity is improved. This is because the rotational velocity is equal to the whirl velocity, and they are close to the first critical velocity, which leads to the stability of the rotor being decreased. According to the relationship between the pressure ratio and effective damping, the effective damping increases obviously with the increase of pressure ratio. It indicates that the pressure ratio has a great influence on the rotor stability, and a high pressure ratio is beneficial to rotor stability.

In order to better understand the internal flow characteristics, the flow field of the seal is analysed under different factors. Fig. 13 shows the streamlines and turbulent kinetic energy contours at the rotational velocity of 750 r/min and 3000 r/min. The leakage steam in seal presents an unsteady motion. The distribution of turbulent kinetic energy in the seal has a small variation with the increase of rotational velocity. However, high turbulent kinetic energy appears at the tip of the seal, which indicates that the kinetic energy dissipation caused by throttling is the main mechanism of the seal. At high rotational velocity, the leakage steam has more severe vortex motion and generates larger vortex at seal outlet. This is the result of leakage steam carried by rotor surface. The circumferential velocity of leakage steam increases with the increase of rotational velocity, which makes the vortex become larger.

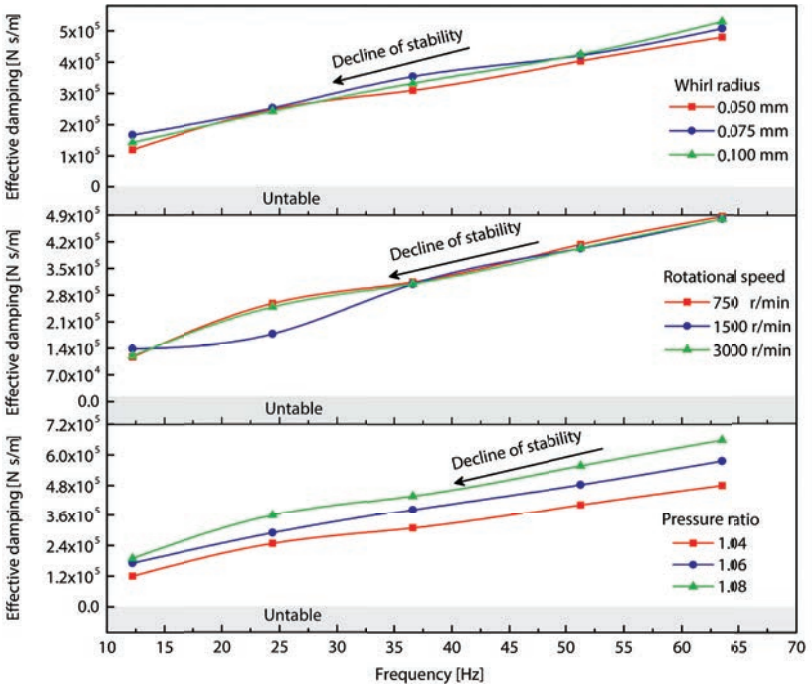

Fig. 12. *Influence of three factors on effective damping*

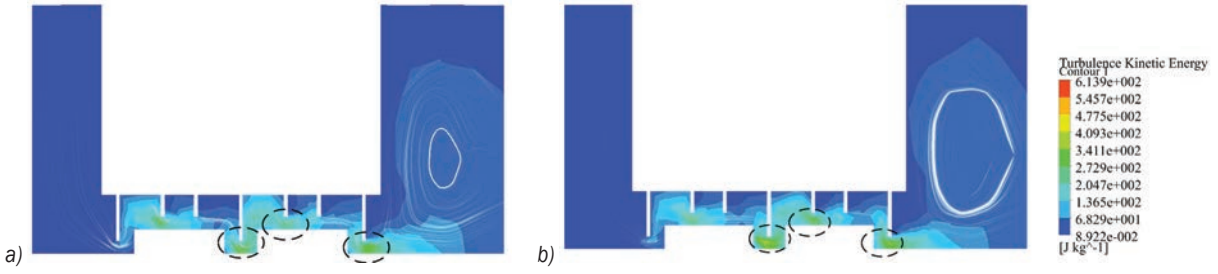

Fig. 13. *Streamlines and turbulent kinetic energy of flow field; a) rotational velocity is 750 r/min, and b) rotational velocity is 3000 r/min*

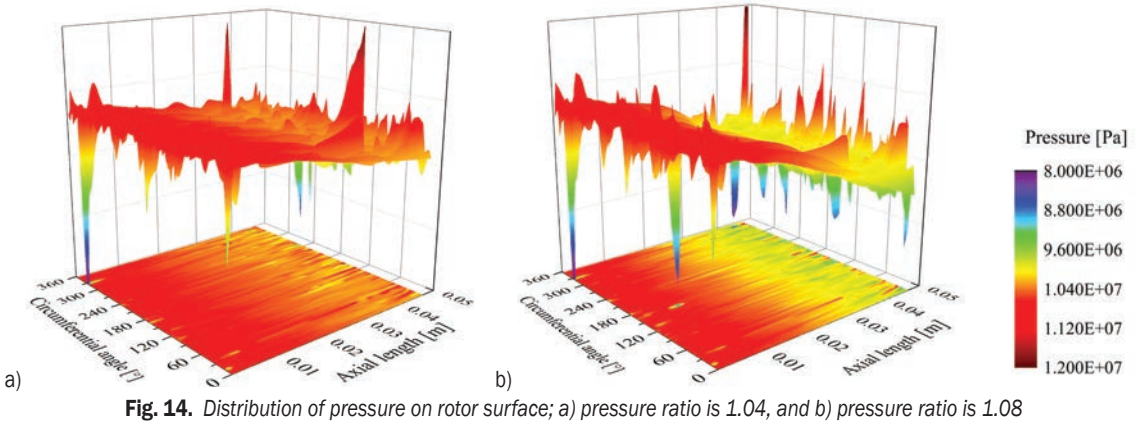

Fig. 14. *Distribution of pressure on rotor surface; a) pressure ratio is 1.04, and b) pressure ratio is 1.08*

Fig. 14 shows the three-dimensional distribution of pressure on the rotor surface. It can be seen that the pressure of rotor surface fluctuates violently as the eccentricity of the rotor, which is caused by the unsteady flow of leakage steam. It is the main reason for steam flow-excited vibration of the rotor. The

maximum pressure fluctuation appears at model inlet and outlet. Compared Fig. 14a and b, the fluctuation range of outlet pressure under the high-pressure ratio is wide, but the pressure distribution is relatively uniform; meanwhile, the lower pressure causes the smaller force on the rotor. At the same time, Fig. 12 shows that the effective damping of the rotor is larger under the high-pressure ratio, so the rotor is relatively stable.

3 CONCLUSIONS AND FUTURE OUTLOOK

The three-dimensional whirl motion is implemented through mesh deformation. On this basis, the influences of whirl radius, whirl frequency, rotational velocity, and pressure ratio on the rotor dynamic characteristics are obtained. The rotor stability affected by steam flow excited vibration is analysed and the mechanism of steam flow excited vibration is clearly revealed through analysis of flow field. The conclusions are as follows.

The rotor whirl motion using mesh deformation is in good agreement with the actual situation. The steam flow exciting forces and dynamic coefficients in multi-frequency whirl motion show nonlinear change and the steam flow exciting forces increase with the increase of whirl frequency. The calculation results obtained from the simplified equation based on duality is not accurate enough.

The whirl radius, whirl frequency, rotational velocity, and pressure ratio have great influence on the rotor dynamic coefficients. The direct damping increases with the increase of whirl frequency. The range of direct stiffness, cross-coupling stiffness and cross-coupling damping are increased at large whirl radius. At the 24.41 Hz whirl frequency, the maximum fluctuations of average direct stiffness, cross-coupling stiffness, direct damping and cross-coupling damping are 8.1 %, 113.2 %, 45.8 % and 121.0 % respectively. The direct stiffness and direct damping increase with the increase of the pressure ratio.

The pressure fluctuation caused by eccentricity is the main reason for steam flow excited vibration. With the increase of rotational velocity, the turbulent kinetic energy increases and the vortex motion is more intense. The effective damping of the rotor can adequately evaluate the rotor stability. The rotor stability increases with the increase of whirl frequency because the effective damping is improved. At a high-pressure ratio, the fluctuation range of pressure at seal outlet is wide, but the pressure distribution is relatively symmetrical and uniform.

The dynamic characteristics and stability of a 300 MW steam turbine rotor influenced by steam flow excited vibration are investigated. The nonlinear dynamic characteristics of the seal are different for steam parameters and seal structures, which is more prominent for the ultra-supercritical units. However, the existing whirl equation is unsuitable for large diameter rotor (over 800 mm). An improved whirl equation for ultra-supercritical units is necessary to make large diameter rotor whirling. Meanwhile, the nonlinear motion of rotor induced by steam flow excited vibration is also worthy of further study.

4 ACKNOWLEDGEMENT

This study was funded by the National Natural Science Foundation of China (NSFC) (grant number 51576036).

5 NOMENCLATURE

e	whirl radius of rotor, [m]
$\dot{x}(t)$	velocity in the x direction, [m/s]
$\dot{y}(t)$	velocity in the y direction, [m/s]
Ω	Whirl velocity, [rad/s]
ω	Rotational velocity, [rad/s]
θ_0	Initial angle, [rad]
t	Time, [s]
F	Steam exciting force, [N]
k	Stiffness, [N/s]
c	Damping, [N·s/m]
C_E	Effective damping, [N·s/m]
$x(t)$	Displacement in the x direction, [m]
$y(t)$	Displacement in the y direction, [m]
h	Cavity depth, [mm]
t_h	Teeth thickness, [mm]
T	Temperature, [K]
l	Convex plate height, [mm]
C_r	Seal tip clearance, [mm]
d	Displacement in frequency domain, [mm]

Subscripts:

x	x direction in cartesian coordinates
y	y direction in cartesian coordinates
i	five whirl velocities; (750, 1500, 2250, 3000, 3750) r/min
xx	from x to x direction in cartesian coordinates
yy	from y to y direction in cartesian coordinates
xy	from x to y direction in cartesian coordinates
yx	from y to x direction in cartesian coordinates
a	forward whirl motion
b	backward whirl motion

5 REFERENCES

[1] Alford, J.S. (1965). Protecting turbomachinery from self-excited rotor whirl. *Journal of Engineering for Gas Turbines and Power*, vol. 87, no. 4, p. 333-343, **DOI:10.1115/1.3678270**.

[2] El-Gamal, H.A., Awad, T.H., Saber, E. (1996). Leakage from labyrinth seals under stationary and rotating conditions. *Tribology International*, vol. 29, no. 4, p. 291-297, **DOI:10.1016/0301-679X(95)00043-4**.

[3] Kim, H.S., Cho, M., Song, S.J. (2002). Stability analysis of a turbine rotor system with Alford forces. *Journal of Sound & Vibration*, vol. 258, no. 4, p. 777-790, **DOI:10.1006/jsvi.2002.5189**.

[4] Ha, T.W., Lee, Y.B., Kim, C.H. (2002). Leakage and rotordynamic analysis of a high pressure floating ring seal in the turbo pump unit of a liquid rocket engine. *Tribology International*, vol. 35, no. 3, p. 153-161, **DOI:10.1016/S0301-679X(01)00110-4**.

[5] Vance, J.M., Laudadio, F.J. (1984). Experiment measurement of Alford's force in axial-flow turbomachinery. *Journal of Engineering for Gas Turbines & Power*, vol. 106, no. 3, p. 585-590, **DOI:10.1115/1.3239610**.

[6] Zhang, W.F., Yang, J.G., Tian, Y.W., Cao, h., Gu, J.G. (2013). Research on the leakage and dynamic characteristics of a new kind of radial annular seal and comparisons with labyrinth seals. *Proceedings of the Institution of Mechanical Engineers, Part A: Journal of Power and Energy*, vol. 227, no. 3, p. 261-271, **DOI:10.1177/0957650912474388**.

[7] Iwatsubo, T., Ishimaru, H. (2010). Consideration of whirl frequency ratio and effective damping coefficient of seal. *Journal of System Design & Dynamics*, vol. 4, no. 1, p. 177-188, **DOI:10.1299/jsdd.4.177**.

[8] Duan, W., Chu, F., Kim, C.H., Lee, Y.B. (2007). A bulk-flow analysis of static and dynamic characteristics of floating ring seals. *Tribology International*, vol. 40, no.3, p. 470-478, **DOI:10.1016/j.triboint.2006.04.010**.

[9] Ding, X.J., Yang, Y.L., Chen, W., Huang, H., Zheng, C.G. (2006). Calculation method of efficiency factor in Alford's force. *Proceedings of the Institution of Mechanical Engineers, Part A: Journal of Power and Energy*, vol. 220, no. 2, p. 169-177, **DOI:10.1243/095765006X75983**.

[10] Rhode, D.L., Hensel, S.J., Guidry, M.J. (1993). Three-dimensional computations of rotordynamic force distributions in a labyrinth seal. *Tribology Transactions*, vol. 36, no. 3, p. 461-469, **DOI:10.1080/10402009308983184**.

[11] Xia, P., Liu, Z., Yu, X., Zhao, J. (2018). A transient bulk flow model with circular whirl motion for rotordynamic coefficients of annular seals. *Chinese Journal of Aeronautics*, vol. 31, no. 05, p. 1085-1094, **DOI:10.1016/j.cja.2018.02.011**.

[12] Tam, L.T., Przekwas, A.J., Muszynska, A., Hendricks, R.C., Braun, M.J., Mullen, R.L. (1987). Numerical and analytical study of fluid dynamic forces in seals and bearings. *Journal of Vibration and Acoustics*, vol. 110, no. 3, p. 315-325, **DOI:10.1115/1.3269519**.

[13] Sun, D., Wang, S., Xiao, Z., Meng, J., Wang, X., Zheng, T. (2015). Measurement versus predictions of rotordynamic coefficients of seal with swirl brakes. *Mechanism and Machine Theory*, vol. 94, p. 188-199, **DOI:10.1016/j.mechmachtheory.2015.08.009**.

[14] Li, J., Li, Z.G. (2011). Review of the leakage flow and rotordynamic characteristics of pocket damper seals. Advances in Mechanics, vol. 41, no. 5, p. 519-536, **DOI:10.6052/1000-0992-2011-5-lxjzJ2011-028**.

[15] Ishii, E., Kato, C., Kikuchi, K., Ueyama, Y. (1997). Prediction of rotordynamic forces in a labyrinth seal based on three-dimensional turbulent flow computation. *JSME International Journal. Series C: Mechanical Systems, Machine Elements and Manufacturing*, vol. 40, no. 4, p. 743-748, **DOI:10.1299/jsmec.40.743**.

[16] Hirano, T., Guo, Z., Kirk, R.G. (2003). Application of CFD analysis for rotating machinery: Part 2—Labyrinth seal analysis. *ASME Turbo Expo: Power for Land, Sea, and Air*, p. 661-667, **DOI:10.1115/gt2003-38984**.

[17] Subramanian, S., Sekhar, A.S., Prasad, B.V.S.S.S. (2016). Rotordynamic characteristics of rotating labyrinth gas turbine seal with centrifugal growth. *Tribology International*, vol. 97, p. 349-359, **DOI:10.1016/j.triboint.2016.01.003**.

[18] Yan, X., Li, J., Feng, Z.P. (2011). Investigations on the rotordynamic characteristics of a hole-pattern seal using transient CFD and periodic circular orbit model. *Journal of Vibration & Acoustics*, vol. 133, no. 4, p. 783-789, **DOI:10.1115/1.4003403**.

[19] Zhang, L.Y., He, L., Stüer, H. (2013). A numerical investigation of rotating instability in steam turbine last stage. *ASME Journal of Turbomachinery*, vol. 135, no. 1, p. 011009, **DOI:10.1115/1.4006330**.

[20] El-Marhomy, A.A., Abdel-Sattar, N.E. (2004). Stability analysis of rotor-bearing systems via Routh-Hurwitz criterion. *Applied Energy*, vol. 77, no. 3, p. 287-308, **DOI:10.1016/S0306-2619(03)00139-9**.

[21] Ma, W., Huang, H., Feng, G., Chen, Z., Kirk, R.G. (2015). Labyrinth seals diameter and length effect study on nonlinear dynamics. *Procedia Engineering*, vol. 99, p. 1358-1364, **DOI:10.1016/j.proeng.2014.12.670**.

[22] Li, Z.G., Li, J., Feng, Z.P. (2015). Comparisons of rotordynamic characteristics predictions for annular gas seals using the transient computational fluid dynamic method based on different single-frequency and multifrequency rotor whirling models. Journal of Tribology, vol. 138, p. 011701, **DOI:10.1115/1.4030807**.

Strojniški vestnik - Journal of Mechanical Engineering 66(2020)3, 175-183

DOI:10.5545/sv-jme.2019.6294 Original Scientific Paper
Received for review: 2019-08-24
Received revised form: 2019-12-29
Accepted for publication: 2020-02-07

Experimental Analysis of Process Parameter Effects on Vibrations in the High-Speed Grinding of a Camshaft

Tao Liu[1,2] – Zhaohui Deng[1,2,*] – Lishu Lv[1,2] – Shuailong She[1,2] – Wei Liu[1,2] – Chengyao Luo[1,2]

[1] Hunan University of Science and Technology, Hunan Provincial Key Laboratory of High Efficiency and Precision Machining of Difficult to Machine Material, China

[2] Hunan University of Science and Technology, Intelligent Manufacturing Institute, China

The capacity to minimize vibrations in grinding by the selection of appropriate process parameters is a significant benefit in the process optimization of cam grinding. This paper presents survey methods to characterize and quantify the vibrations and waviness in a camshaft grinding application. First, a modal analysis was conducted to study the dynamic characteristic of a camshaft grinding machine. Then, developed methods were applied to study the influences of various parameters on vibrations in the high-speed grinding of a camshaft. Furthermore, the influence of each grinding process condition on surface waviness in high-speed camshaft grinding was studied. The results show that the vibrations and the surface waviness change with the increase of grinding depth, and an appropriate grinding wheel speed combined with a workpiece speed has, for most grinding conditions, a reducing effect on vibration magnitudes and waviness. Finally, the specific indications about the optimal grinding process parameters in terms of dynamic characteristics of the grinding machine were given, and the speed ratio=1.2 is a novel choice.

Keywords: vibrations, high-speed grinding, surface waviness, frequency spectrum, camshaft

Highlights

- *An experimental method to analyse the process parameters effects on vibrations in the high-speed grinding of a camshaft is presented.*
- *The modal analysis enables choosing the favourable frequency range.*
- *The significant relationships between the features of the process parameters and dynamic characteristic of the camshaft grinder are effectively obtained.*
- *The optimal grinding process parameters in terms of the dynamic characteristics of the grinding machine are given.*

0 INTRODUCTION

The camshaft, as a key component in creating a prescribed motion in the contacting element (follower), has been widely used in many industrial fields. Computer numerical control (CNC) camshaft grinders and cubic boron nitride (CBN) wheels have advanced dramatically in recent years and significantly influenced the progress of the high-speed grinding of camshafts [1].

High-speed grinding is often accompanied by complicated vibration behaviours [2]. The cam grinding process is regarded as a typical discontinuous grinding mechanism that includes rapid entries and exits of the grinding wheel into the camshaft accompanied by dynamic grinding depth over the engagement. Vibrations in such conditions are inevitable in the high-speed grinding of a camshaft. Various parameters, including grinding speed, grinding depth, camshaft profile, and machining conditions, play critical roles for the vibrations, while the vibrations in processing acutely affect the wheel life and the ultimate grinding quality. In general, increased vibration magnitude leads to a reduction in grinding wheel life and higher surface waviness.

Two types of vibrations can arise in the high-speed grinding of camshaft: the first type is forced vibrations that originate from the variation in grinding depth and the unbalance of the wheel [3]. These vibrations cause troubles in the grinding processing if their vibration frequency matches one of the natural modes of the machine tool-workpiece system. The second type, known as “chatter”, may arise in grinding due to the regenerative and frictional effects of the machine tool-workpiece. An unstable grinding process occurs due to these self-excited vibrations, and the results of grinding wheel wear [4], unacceptable surface finish, and increased noise would arise. In practice, the two types of vibrations above are often present in any grinding operation at the same time even if their impacts on the final result differ.

Much research has been done concerning experimental and analytical grinding vibrations to identify the vibration form during grinding. Robles-Ocampo et al. [5] presented a novel nonlinear model for centreless grinding which describes the dynamic behaviour of the process. Zhang et al. [6] proposed

*Corr. Author’s Address: Hunan University of Science and Technology, Intelligent Manufacturing Institute, Xiangtan, China, edeng0080@vip.sina.com

a non-linear dynamic model to research the dynamic characteristics of the grinding process and the different vibrations resulting in the qualitative behaviour of the grinding machine was demonstrated. Mohammadi and Ahmadi [7] presented an update to the widely used multi-frequency solution of regenerative chatter by modelling the tool dynamics as a linear time-periodic system. In order to investigate the nonlinear, non-autonomous vibration characteristics of a cylindrical traverse grinding process, Jung et al. [8] performed nonlinear analyses applied to a spatially periodic wavy surface. On the basis of mechanical analysis, Zhu et al. [9] researched the chatter stability of grinding thin-walled parts based on the modal experiments of titanium alloy workpiece and grinding head. Denkena et al. [10] presented a system for chatter detection and elimination for external cylindrical grinding machines. Thomazella et al. [11] proposed a new digital processing technique for the monitoring of the chatter phenomenon during the grinding of AISI 1045 steel with various grinding wheels.

It can be seen from the above research that the identification method of vibration form has become essentially mature. However, the vibration behaviour of different processing methods is variational, so the experimental analysis is necessary for exploring the specific form of vibration.

In contrast, the grinding process parameters affect the grinding force and machine dynamic behaviours, and then change the form of vibration and surface waviness. To better establish the relationship between grinding process parameters and stable grinding conditions, the investigations of the grinding vibration mechanism are critical. Cao et al. [12] established a new model for the surface topography of the grinding process to discuss the effects of the wheel vibration amplitude, wheel grit number, as well as process parameters on the surface waviness and roughness. Leonesio et al. [13] presented a novel frequency domain approach for identifying the process parameters, exploiting in-process system response, which measured via impact testing. Liu et al. [14] analysed the process parameters and stability grinding conditions affecting the grinding stability of the blisk-blade belt. Rao et al. [15] estimated the influence of various input process parameters on machine tool life by determining the roughness on a machined surface and amplitude of workpiece vibration. Therefore, given that the lessening of vibration is profitable for grinder life and processing precision, it is researching the effects of grinding process parameters and grinding conditions on the dynamic behaviours is necessary.

However, few studies related to the vibrations in high-speed grinding of camshaft have been made. This paper aims to effectively quantify vibration magnitudes and surface waviness, which make it possible to research the effects of the process parameters on the dynamic characteristics in the high-speed grinding of camshaft.

In the following sections, the measurement methods and experimental setup are described. Next, experimental results are presented and discussed. In the final section, conclusions and recommendations are given.

1 EXPERIMENTAL METHODOLOGY

The vibration and surface waviness with different grinding speeds and grinding depths have been investigated. The experiments were set to three setups: First, the sampling frequency and analysis spectral line of each test instrument were set, and the interference of the external vibration source to the test signal was observed and eliminated. Second, the vibration acceleration signal of the processing system was collected when the machine was idling with different grinding process parameters, which was compared with the subsequent experimental research. Third, the vibration signal and surface waviness were sampled with different grinding process parameters in the actual machining.

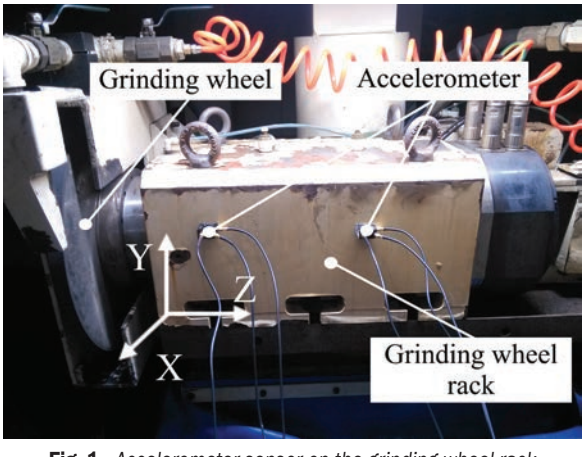

Fig. 1. *Accelerometer sensor on the grinding wheel rack*

1.1 Measurement Methods

The acceleration signal measurements were conducted in a camshaft grinding machine with a three-direction EA-YD-152 piezoelectric acceleration sensor (Econ, China), as shown in Fig. 1. The acceleration sensor

was glued on the grinding wheel rack. The test platform of vibrations the machine-tool-workpiece system in the high-speed grinding of camshaft is shown in Fig. 2. Acceleration signals in *X*, *Y*, and *Z* directions were measured during grinding. The grinding force was measured with a cylindrical grinding dynamometer. The ANVAT Signal Automatic Gathering and Analysis System (Econ, China), and the sample frequency used in the signal collection system was set to 2 kHz, which was applied to monitor the vibration of machine tools in the grinding process and gathered data of idling, steadily and occurs chatter in the high-speed grinding process. The surface waviness was detected by MarSurf M300 Surface Roughometer (Mahr, German). The arithmetical mean deviation of the waviness profile was selected as the characteristic parameter of the waviness. The measurement direction of the waviness was parallel to the grinding direction.

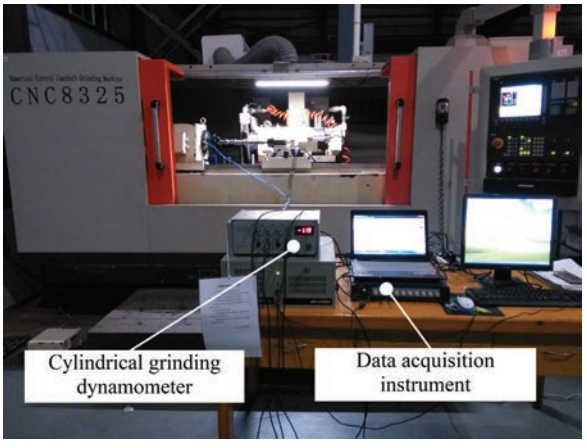

Fig. 2. *The test platform of vibrations in high-speed grinding of camshaft*

1.2 Modal Analysis

Modal analysis of the processing system was accomplished to aid in the in-depth understanding of the dynamic characteristic. The frequency response functions (FRFs) of the processing system were acquired by impact hammer tests. In the tests, modal parameters such as the equivalent mass (m), the stiffness coefficient (k), the structural damping ratio (ζ), and the natural frequency (w_n) of the processing system were obtained. The acceleration sensor was installed in the feed direction of the grinding machining, and a hammering test was conducted using hammer beats.

The impacting point was located in the grinding wheel rack of the grinding machine while the measuring points were set according to Fig. 1. The three directions were excited, and the corresponding response was measured. From the data shown in Table 1, it is obvious that the dynamic stiffnesses of the grinding wheel rack in the *X* direction and *Z* direction is far less than the dynamic stiffness in the *Y* direction. The natural modes at 51.8 Hz, 77.2 Hz, 146.6 Hz, and 176 Hz are found in the *X* direction. The mode of the poorest stiffness is the fourth mode in the *X* direction at 176 Hz, for which the dynamic stiffness is 14100 N/m.

Table 1. *Dynamic stiffness of grinding wheel rack*

Mode [Hz]	Dynamic stiffness [N/mm]		
	X direction	Y direction	Z direction
51.8	–	75900	15500
77.2	28600	34500	–
105.7	18600	33400	19200
146.6	27100	65600	–
176.0	14100	61900	8471.5

1.3 Parameters of Experiments

The experiments were conducted on an ultra-high-speed precision combined grinder (type CNC8325) manufactured by the Hunan Hicam Engineering Technology Research Co. Ltd, China. The grinding wheel is a 70# CBN grinding wheel with the highest linear speed up to 200 m/s, and the diamond roller is used for dressing, the dressing parameters are shown in Table 2.

Table 2. *Dressing parameter*

Dressing speed [r/min]	Grinding wheel taper compensation [°]	Grinding wheel radius [mm]	Value of dressing [mm]	Idle speed of grinding wheel [mm/min]
800	0	200	0.003	1500

Table 3. *Grinding test conditions*

Project	Parameter
grinding wheel	φ 400 × 25 mm, CBN
camshaft specimen	chilled cast iron
grinding-wheel speed, v_s	60 m/s to 150 m/s
workpiece speed, n_w	90 r/min to 180 r/min
grinding depth, a_p	0.01 mm to 0.04 mm

A typical cam is used as a sample. The radius of the base circle is 15.5 mm, the workpiece material is chilled cast iron. The grinding conditions used in the experiments are from the production data of the manufacturer, as shown in Table 3, and a series of experiments were conducted with the fractional

factorial design. The feeding speed of the grinding wheel was set to 4500 mm/min.

2 RESULTS AND DISCUSSIONS

2.1 Vibration Characteristics of Machine Tools

The vibration signal was collected in the time domain for all directions. The frequency spectrum analysis method was applied to characterize the acceleration signal in the frequency domain [16]. The frequency spectrum of the vibration signal of idling test and actual process is shown in Fig. 3.

As seen from Fig. 3, A is the maximum vibration amplitude, and f is the frequency when the vibration amplitude is maximum; there are the more intensive low-rising value vibration spectrum peak under the grinding wheel spindle rotation frequency high frequency area. The frequency of vibration amplitude could also increase gradually to more obvious impact on vibration of the processing system with the change of the grinding wheel speed.

The forced vibration is the main vibration source of the processing system, and the vibration force produced by the rotating unbalance of the grinding wheel spindle system is the most important factor that affects vibration of the processing system [17], and which is positively related to grinding velocity. The excitation amplitude is maximum when the grinding velocity v_s = 140 m/s, and the rotation of the grinding wheel spindle system frequency is 112.5 Hz, which is close to the third-order natural frequency of the camshaft high-speed grinding system (105.7 Hz); therefore, the main vibration amplitude of the processing system is greater.

Table 4. *Comparison of camshaft grinding idling test and actual grinding test (n_w = 90 r/min, a_p = 0.01 mm)*

Level	Grinding speed [m/s]	Frequency [Hz]	Maximum vibration amplitude [G]	
			Actual process	Idling test
1	60	48.34	1.33	1.483
2	90	77.63	1.424	1.79
3	120	95.21	1.512	1.912
4	140	112.79	2.518	2.675
5	150	120.12	1.72	2.191

The comparison of the spectral analysis obtained from the test of idling and actual grinding process is shown in Table 4. Because the effects of grinding damping in the actual grinding [18], the main vibration amplitude of actual process is smaller than the main vibration amplitude of the idling test. However, there

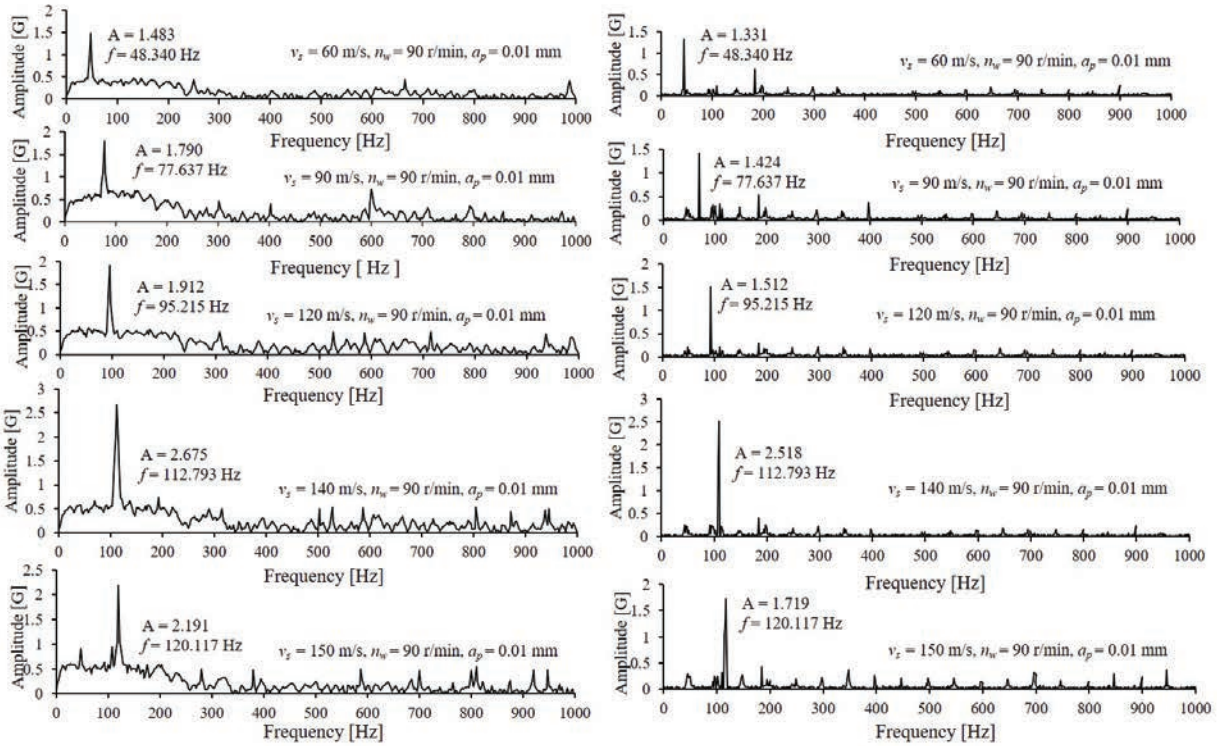

Fig. 3. *Frequency spectrum of vibration signal for a) idling test, and b) actual process*

is not much difference between the main vibration frequency in the idling test and actual process, and the value of vibration frequency of both are close to exciting frequency that caused by rotation imbalance of the grinding wheel spindle system.

2.2 Parameter Effects

The dynamic characteristic of the processing system changes with the grinding process parameters. The vibration signal of different status of processing system is shown in Fig. 4.

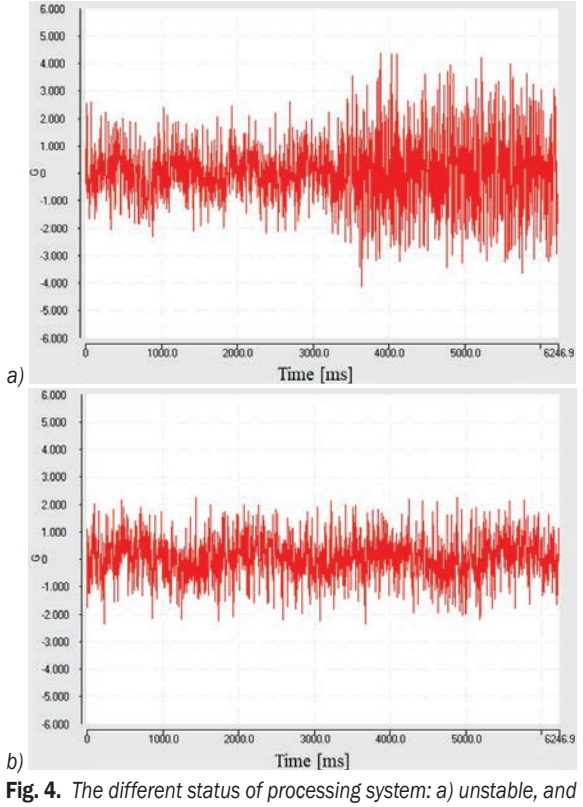

Fig. 4. *The different status of processing system: a) unstable, and b) stable*

The grinding stability lobes diagram of camshaft was derived, and the grinding process parameters (as shown in Table 5) of vibration testing were marked out with red dots, as shown in Fig. 5.

As shown in Fig. 5, the points of experiments No. 3, 4, 10 ,11, and 12 are above the lobe's envelope of stability in the diagram, which is the instability zone in the grinding process. While the points of experiments No. 1, 5, 6, and 9 are in the inferior of the lobe's envelope that is the stable grinding zone in the grinding process. The points of experiments No. 2, 7, and 8 are located on a critical line of the stability zone and the instability zone in the grinding.

From Fig. 6, it can be seen that forced vibration was dominant in experiments No 1, 2, 5, 6, 7, 8, and 9. The vibration of the processing system is combined with the forced vibration and self-excited vibration in experiments No. 3, 4, 10, 11, and 12, and the influence of self-excited vibration is more significant with the change of the grinding speed and grinding depth. As seen from Table 1, the mode of poorest stiffness is the fourth mode in the *X* direction at 176 Hz, which the dynamic stiffness is 14100 N/m, so the chatter is most likely to happen near the fourth mode. According the frequency spectrum analysis, the chatter frequency is 187.5 Hz, which slightly higher than natural frequency of the fourth mode in the *X* direction, as mentioned in [19].

Table 5. *The experimental parameters*

Experiment No.	Factors			Feeding speed [mm/min]
	Grinding speed [m/s]	Workpiece speed [r/min]	Grinding depth [mm]	
1	60	90	0.01	4500
2	60	90	0.02	4500
3	60	90	0.03	4500
4	60	90	0.04	4500
5	120	90	0.01	4500
6	120	90	0.02	4500
7	120	90	0.03	4500
8	120	90	0.04	4500
9	140	90	0.01	4500
10	140	90	0.02	4500
11	140	90	0.03	4500
12	140	90	0.04	4500

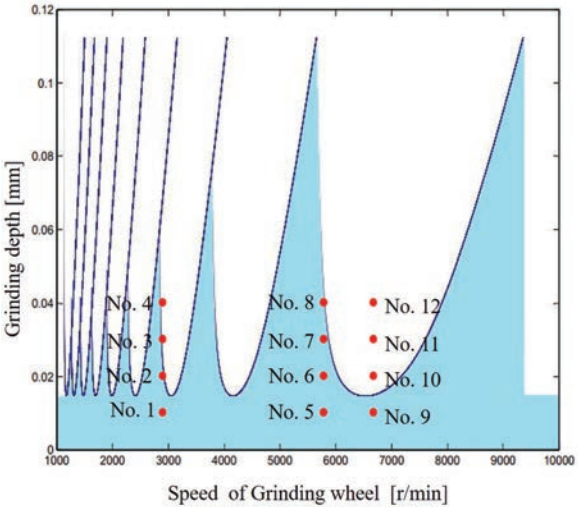

Fig. 5. *Grinding stability lobes diagram*

The acquired results indicate a clear difference in vibrational characteristic rest with the grinding

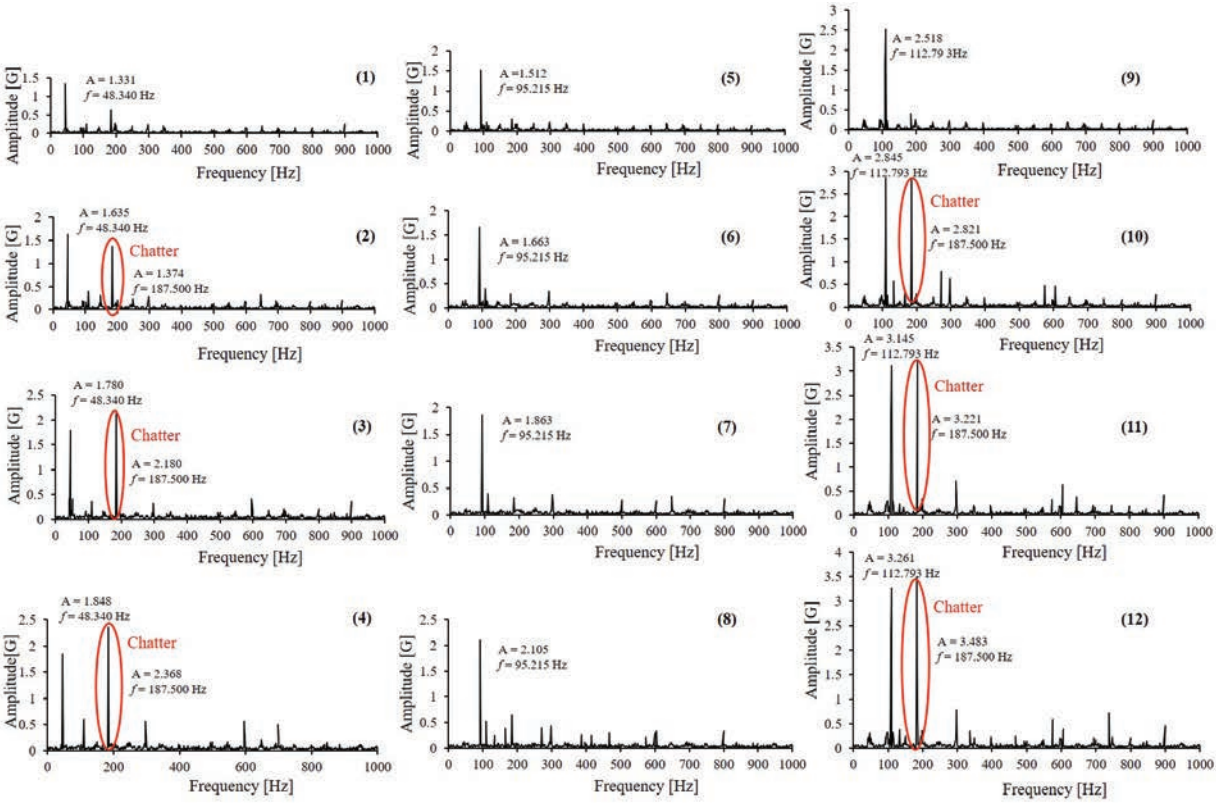

Fig. 6. *Vibration signal spectrum of camshaft grinding*

process parameters. Although vibration is inevitable during machining, machining process parameters could be reasonably selected to reduce self-excited vibration and resonance in the high-speed grinding process of camshaft.

2.3 Surface Waviness

The vibrations of the grinding wheel system are the main reason for surface waviness in grinding. The variation of the grinding process parameters leads to the change of system grinding force, geometric interference, dynamic stiffness, etc., and then affects the surface waviness of the workpiece. To study the influence of each grinding process conditions on surface waviness in high-speed camshaft grinding, in this paper, a Motif algorithm was used to evaluate the surface topography after obtaining the original contour information of surface topography, and the separation calculation of surface waviness of the workpiece was completed.

The average depth of corrugation on the curve was as the evaluation index of the surface waviness (W) of high-speed grinding of camshaft, and its numerical calculation is shown in Eq. (1):

$$W = \frac{1}{2n}\sum_{j=1}^{2n} W_j, \tag{1}$$

where W_j is corrugation value of point j, $j = 1, 2, ..., 2n$. The maximum value of waviness is usually above the grain direction of grinding. Therefore, the surface topography of the camshaft after high-speed grinding was measured along the grain direction, and its original contour curve was obtained, as shown in Fig. 7.

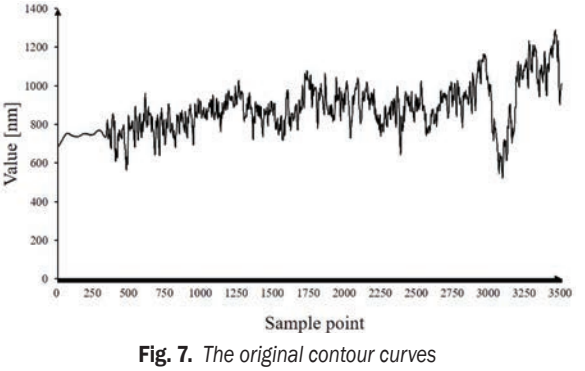

Fig. 7. *The original contour curves*

Fig. 8 shows that the camshaft surface roughness quality obtained by grinding with the grinding

process parameters in this test meets the processing requirements and the surface waviness values of experiments No. 3, 4, 10, 11, and 12 are much higher than that of experiments No. 1, 5, 6, and 9, while the waviness values of experiments No. 2, 7, and 8 are in the middle range. According to vibration spectrum analysis in the process of grinding system and stability lobes diagram analysis, the tests of experiments No. 1, 5, 6, and 9 are in the stable zone of grinding, and the self-excited vibration does not occur, so the quality of grinding surface is good. and values of the surface waviness are less than 0.5 microns.

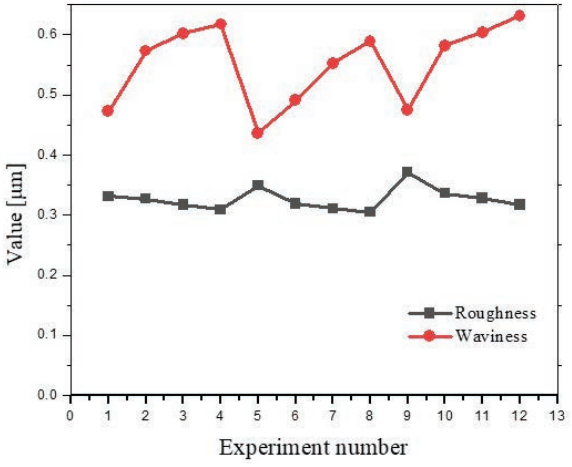

Fig. 8. *Test results of roughness and waviness*

To further analyse the influence of different grinding process parameters (grinding speed, workpiece speed, and grinding depth) on surface waviness, orthogonal tests with three factors and four levels were carried out on the representative process parameters in the stability lobe diagram. The degree of influence of the three factors were investigated with range analysis and variance analysis.

The comparative analysis of the mean value (α_i, β_i, γ_i, δ_i) in Table 6 indicated that the range of the influence of the grinding parameters to the surface waviness is grinding depth, grinding velocity, and workpiece speed, where α_i, β_i, γ_i, δ_i represents the average value of the surface waviness corresponding to Level 1, 2, 3, and 4 of column i in the orthogonal table and R_i is the range of the surface waviness . The value of F (ratio of the variance of the sample mean and the error variance, which represent the significance level) and value of significance level in Table 7 shows the same conclusion as in Table 6.

Surface waviness is a positively correlated relationship with grinding depth, and the influence mechanism of the grinding velocity and workpiece speed on surface waviness is more complicated [20]; there is obvious interaction between the grinding velocity and workpiece rotational speed.

Table 6. *Result of test and range analysis*

Project	Grinding speed [m/s]	Workpiece speed [r/min]	Grinding depth [mm]	Waviness [μm]
1	90	90	0.01	0.445
2	90	120	0.02	0.494
3	90	150	0.03	0.558
4	90	180	0.04	0.649
5	120	90	0.02	0.491
6	120	120	0.01	0.429
7	120	150	0.04	0.597
8	120	180	0.03	0.567
9	140	90	0.03	0.604
10	140	120	0.04	0.625
11	140	150	0.01	0.460
12	140	180	0.02	0.578
13	150	90	0.04	0.619
14	150	120	0.03	0.595
15	150	150	0.02	0.488
16	150	180	0.01	0.437
α_i	0.5365	0.5397	0.4428	
β_i	0.5210	0.5357	0.5228	
γ_i	0.5667	0.5257	0.5810	
δ_i	0.5347	0.5577	0.6225	
R_i	0.0458	0.032	0.1798	

Table 7. *Test variance analysis*

Factor	Sum of squares	DOF	Mean square	F	Sig.
Grinding speed	0.0044645	3	0.0014882	3.67	0.082
Grinding depth	0.0747485	3	0.0249162	61.47	0.000
Workpiece speed	0.0024320	3	0.0007147	1.76	0.254

Via matching process parameters with machine dynamics, more stable machining results can be obtained [21] and [22]. Fig. 9 shows the change of surface waviness in the grinding process with different linear speeds (v_s = 90 m/s, v_s = 120 m/s, v_s = 140 m/s, and v_s = 150 m/s) and the grinding depth remains unchanged, a_p = 0.01 mm. The speed ratio is the ratio of grinding speed to workpiece speed, which is dimensionless.

It is seen from Fig. 9, with the increased speed ratio, the surface waviness value decreases firstly and then increases; it reaches the optimal value when the speed ratio is 1.2. It is thought that when the workpiece speed continues to increase, the grinding wheel acceleration and jerk become greater because the complexity of non-circular profile shapes, the

overcut or undercut may be happened in the tangential point tracing grinding process. In particular, the linear speed of grinding wheel is above 140 m/s, this phenomenon is more obvious, and the vibration of the processing system intensifies, which leads to higher waviness on the surface of camshaft machining.

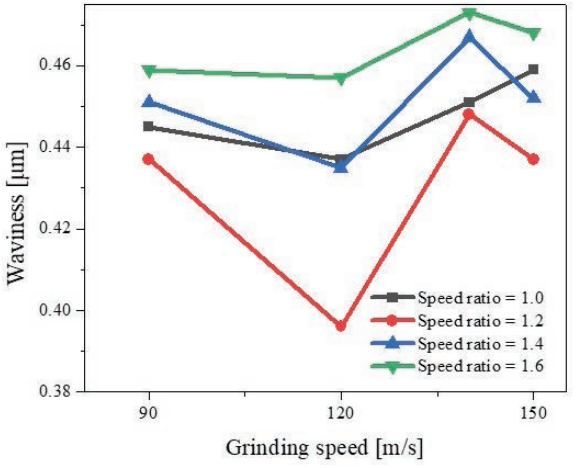

Fig. 9. *Results under different speed ratio*

At the same grinding speed ratio, with the grinding speed in a certain range (90 m/s to 120 m/s) increasing, normal grinding force is reduced and the grinding processing system is in a stable condition, so the surface waviness become lower. With speed of grinding wheel at 130 m/s to 140 m/s, although the normal grinding force has diminished constantly, but the frequency of grinding wheel spindle system is close to the natural frequency, so vibration amplitude of grinding process system increases, and the surface waviness value becomes larger. As the grinding speed increases to 150 m/s, the surface waviness is lower due to the grinding wheel frequency being away from the natural frequency of the processing system.

The above investigations have significance for the optimization of processing parameters based on efficient and stable targets. In the actual grinding processing of the camshaft, the following process condition optimization strategies can be adopted to control the waviness:

- In the high-speed camshaft grinding, the grinding speed is recommended to be selected within the range near 120 m/s and as far as possible to avoid natural frequency of the processing system.
- The rotation speed of the workpiece should be selected appropriately, appropriate grinding wheel speed combined with a relatively workpiece speed has a reducing effect on vibration magnitudes and waviness for the most of grinding conditions, and the speed ratio 1.2 is a novel choice.

3 CONCLUSIONS

An experimental method to analyse the process parameters effects on vibrations in high-speed grinding of camshaft is presented. The modal analysis enables choosing the favourable frequency range. The significant relationships between the features of the process parameters and the dynamic characteristic of the camshaft grinder are effectively obtained, i.e. the influence of the different grinding speeds and grinding depths on vibration magnitudes and surface waviness. The obtained results strongly demonstrate that the presented methods can be available in evaluation of grinding process parameters in order to lessen vibrations in camshaft grinding. The quantization of vibration magnitudes and surface waviness for the different process parameters used in the tests identify the best selection for specific grinding parameters. It also demonstrates that the grinding speed v_s = 120 m/s gives lowest vibrations in the experiments and higher vibrations with the increasing of grinding depth. It is confirmed by the survey of the frequency domain in which it was shown that a lower dynamic stiffness can, under some conditions, exhibit an unstable appearance which causes increased vibration magnitudes. The most significant factor of grinding surface waviness is the grinding depth. The result of speed ratio grinding test is a vital guideline for the design of process schemes. Additional research is needed to determine whether the different profiles of camshaft have a significant effect on vibration amplitudes. Further investigations are necessary to clarify the impact of grinding wheel wear in relation to vibrations and surface waviness.

4 ACKNOWLEDGEMENTS

This research was financially supported by the project of Hunan Provincial Innovation Foundation for Postgraduate (Grant No. CX20190792), the Natural Science Foundation of Hunan province (Grant No. 2017JJ4007) and the National Science and Technology Major Project (Grant No. 2018ZX04035002-005).

5 REFERENCES

[1] Tang, H., Deng, Z.H., Guo, Y.S., Qian, J., Reynaerts, D. (2014). Research on constant grinding depth model for cam grinding. *The International Journal of Advanced Manufacturing*

Technology, vol. 74, no. 1-4, p. 351-359, **DOI:10.1007/s00170-014-5993-2**.

[2] Wegener, K., Bleicher, F., Krajnik, P., Hoffmeister, H.W., Brecher, C. (2017). Recent developments in grinding machines. *CIRP Annals*, vol. 66, no. 2, p. 779-802, **DOI:10.1016/j.cirp.2017.05.006**.

[3] Zhang, S., Yu, J., To, S., Xiong, Z. (2018). A theoretical and experimental study of spindle imbalance induced forced vibration and its effect on surface generation in diamond turning. *International Journal of Machine Tools and Manufacture*, vol. 133, p. 61-71, **DOI:10.1016/j.ijmachtools.2018.06.002**.

[4] Aleksandrova, I.S. (2019). Multi-objective optimization of the dressing parameters in fine cylindrical grinding. *Strojniški vestnik - Journal of Mechanical Engineering*, vol. 65, no. 2, p. 87-102, **DOI:10.5545/sv-jme.2018.5677**.

[5] Robles-Ocampo, J.B., Jauregui-Correa, J.C., Krajnik, P., Sevilla-Camacho, P.Y., Herrera-Ruiz, G. (2012). Nonlinear model for the instability detection in centerless grinding process. *Strojniški vestnik – Journal of Mechanical Engineering*, vol. 58, no. 12, p. 693-700, **DOI:10.5545/sv-jme.2012.649**.

[6] Zhang, N., Kirpitchenko, I., Liu, D.K. (2005). Dynamic model of the grinding process. *Journal of Sound and Vibration*, vol. 280, no. 1-2, p. 425-432, **DOI:10.1016/j.jsv.2003.12.006**.

[7] Mohammadi, Y., Ahmadi, K. (2019). Frequency domain analysis of regenerative chatter in machine tools with linear time periodic dynamics. *Mechanical Systems and Signal Processing*, vol. 120, p. 378-391, **DOI:10.1016/j.ymssp.2018.10.029**.

[8] Jung, J., Kim, P., Kim, H., Seok, J. (2015). Dynamic modeling and simulation of a nonlinear, non-autonomous grinding system considering spatially periodic waviness on workpiece surface. *Simulation Modelling Practice and Theory*, vol. 57, p. 88-99, **DOI:10.1016/j.simpat.2015.06.005**.

[9] Zhu, L., Yang, Z., Li, Z. (2019). Investigation of mechanics and machinability of titanium alloy thin-walled parts by CBN grinding head. *The International Journal of Advanced Manufacturing Technology*, vol. 100, no. 9-12, p. 2537-2555, **DOI:10.1007/s00170-018-2795-y**.

[10] Denkena, B., Ortmaier, T., Bergmann, B., Schreiber, P., Ahrens, M., Damm, J. (2019). Suitability of integrated sensors for the determination of chatter characteristics in a cylindrical grinding machine. *The International Journal of Advanced Manufacturing Technology*, vol. 102, no. 5-8, p. 2339-2344, **DOI:10.1007/s00170-019-03323-y**.

[11] Thomazella, R., Lopes, W.N., Aguiar, P.R., Alexandre, F.A., Fiocchi, A.A., Bianchi, E.C. (2019). Digital signal processing for self-vibration monitoring in grinding: A new approach based on the time-frequency analysis of vibration signals. *Measurement*, vol. 145, p. 71-83, **DOI:10.1016/j.measurement.2019.05.079**.

[12] Cao, Y., Guan, J., Li, B., Chen, X., Yang, J., Gan, C. (2013). Modeling and simulation of grinding surface topography considering wheel vibration. *The International Journal of Advanced Manufacturing Technology*, vol. 66, no. 5-8, p. 937-945, **DOI:10.1007/s00170-012-4378-7**.

[13] Leonesio, M., Parenti, P., Bianchi, G. (2017). Frequency domain identification of grinding stiffness and damping. *Mechanical Systems and Signal Processing*, vol. 93, p. 545-558, **DOI:10.1016/j.ymssp.2017.02.028**.

[14] Liu, Y., Li, Q., Xiao, G., Huang, Y. (2019). Study of the vibration mechanism and process optimization for abrasive belt grinding for a blisk-blade. *IEEE Access*, vol. 7, p. 24829-24842, **DOI:10.1109/ACCESS.2019.2899495**.

[15] Rao, K.V., Murthy, B.S.N., Mohan Rao, N. (2015). Experimental study on surface roughness and vibration of workpiece in boring of AISI 1040 steels. *Proceedings of the Institution of Mechanical Engineers, Part B: Journal of Engineering Manufacture*, vol. 229, no. 5, 703-712, **DOI:10.1177/0954405414531247**.

[16] Thaler, T., Potočnik, P., Kopač, J., Govekar, E. (2014). Experimental chatter characterization in metal band sawing. *Strojniški vestnik - Journal of Mechanical Engineering*, vol. 60, no. 4, p. 265-273, **DOI:10.5545/sv-jme.2013.1515**.

[17] Badger, J., Murphy, S., O'Donnell, G. (2011). The effect of wheel eccentricity and run-out on grinding forces, waviness, wheel wear and chatter. *International Journal of Machine Tools and Manufacture*, vol. 51, no. 10-11, p. 766-774, **DOI:10.1016/j.ijmachtools.2011.06.006**.

[18] Muhammad, B.B., Wan, M., Feng, J., Zhang, W.H. (2017). Dynamic damping of machining vibration: a review. *The International Journal of Advanced Manufacturing Technology*, vol. 89, no. 9-12, p. 2935-2952, **DOI:10.1007/s00170-016-9862-z**.

[19] Shrivastava, Y., Singh, B. (2019). A comparative study of EMD and EEMD approaches for identifying chatter frequency in CNC turning. *European Journal of Mechanics-A/Solids*, vol. 73, 381-393, **DOI:10.1016/j.euromechsol.2018.10.004**.

[20] Parenti, P., Leonesio, M., Cassinari, A., Bianchi, G., Monno, M. (2015). A model-based approach for online estimation of surface waviness in roll grinding. *The International Journal of Advanced Manufacturing Technology*, vol. 79, no. 5-8, p. 1195-1208, **DOI:10.1007/s00170-015-6864-1**.

[21] Chen, Y., Chen, X., Xu, X., Yu, G. (2018). Effect of energy consumption in the contact zone on machining condition optimization in precision surface grinding. *Strojniški vestnik - Journal of Mechanical Engineering*, vol. 64, no. 4, p. 233-244, **DOI:10.5545/sv-jme.2017.4995**.

[22] Wang, C., Zhang, X., Yan, R., Chen, X., Cao, H. (2019). Multi harmonic spindle speed variation for milling chatter suppression and parameters optimization. *Precision Engineering*, vol. 55, p. 268-274, **DOI:10.1016/j.precisioneng.2018.09.017**.

Strojniški vestnik - Journal of Mechanical Engineering 66(2020)3, 184-192

DOI:10.5545/sv-jme.2019.6474 Original Scientific Paper
Received for review: 2019-11-19
Received revised form: 2020-01-27
Accepted for publication: 2020-02-13

Experimental Investigation of the Micro-hardness of EN-31 Die Steel in a Powder-Mixed Near-Dry Electric Discharge Machining Method

Sanjay Sundriyal[1] -Vipin[1] – Ravinderjit Singh Walia[2,*]
[1]Delhi Technological University, India
[2]Punjab Engineering College, India

The Powder-Mixed Near-Dry Electric Discharge Machining (PMND-EDM) methodology has proven to be efficient in terms of machining rate, surface morphology, and environmental friendliness, unlike traditional EDM. In this study, the presence of a conductive metallic powder (zinc) in the dielectric medium was responsible for changing the topography of the workpiece (EN-31) and resulted in a higher micro-hardness value of the machined component. In this research, an approach has been made to optimize the significant process parameters by using a Taguchi L_9 orthogonal array (OA) to obtain machined components with higher values of micro-hardness, which was measured in terms of Vickers hardness HV. The selected process parameters were tool diameter, mist flow rate, metallic powder concentration, and dielectric mist pressure. By introducing foreign particles (metallic powder), the topography of the machined products has been improved, and the micro-hardness value was found to be enhanced. The confirmation experiment was performed for optimal process parameter settings, and the enhanced micro-hardness value was found to be 506.63 HV in the machined EN-31 die steel.

Keywords: electric discharge machining, powder, near-dry, micro-hardness, optimization

Highlights

- *The PMND-EDM method of machining at optimum input process parameters leads to the generation of machined parts with higher micro-hardness values.*
- *It was observed that optimum parameter condition at A1, B2, C3, and D3 were most dominant in achieving the maximum micro-hardness of the machined EN-31 Die steel workpiece. Confirmation experiments revealed that the highest value of micro-hardness was found to be 506.63 HV at the optimized input process parameters.*
- *The predicted optimal range of confidence interval of conformation experiments (CICE) for micro-hardness was: 445.05 < micro-hardness < 596.35. The 95 % conformation interval of the predicted mean for micro-hardness was: 482.88 < micro-hardness < 558.52.*
- *A layer of hard zinc carbide hard was deposited over the surface of the machined sample, which leads to a higher value of micro-hardness. The experimental results were validated by the confirmation of experiments, and the obtained output results were within the permissible results.*

0 INTRODUCTION

Electric discharge machining (EDM) is a well-recognized non-conventional machining method and has been widely used in creating complex geometries in dies and moulds. EDM uses electric-thermal energy conversion to remove material from the workpieces that were difficult to be machined by any other non-conventional machining method. Although EDM has been globally accepted in the manufacturing industries, undesirable characteristics such as pores, cracks, surface pits and holes in the machined components make this process quite inferior in terms of surface morphology. Several research works have been done to improve the morphology and micro-hardness values of the machined components using powder-additive EDM methodologies. There was an improvement in the capabilities of the EDM process via the addition of powder in the dielectric fluid of EDM [1]. The feasibility of a new type of hybrid powder-mixed near-dry electric discharge machining (PMND-EDM) was confirmed for the first time [2]. The die steel surface was modified with tungsten powder additives in the dielectric medium of EDM [3]. The surface morphology was improved with the addition of metallic powder as there was carbon deposition in the plasma, which also increased the micro-hardness by 100 %. The micro-hardness of SS (stainless steel) was enhanced using powder-mixed electric discharge machining [4]. It was seen that 25 g/l concentration of titanium carbide (TaC) powder in dielectric medium of EDM enhanced the surface characteristics and micro-hardness value of 1200 HV was achievable. There was an improvement in the EDM performance on machining of Ti-6Al-4V by dispersing SiC particles (abrasives) in the dielectric medium with magnetic stirring mechanism [5].Other researchers successfully achieved improved hardness

*Corr. Author's Address: Punjab Engineering College, Vidya Path, Chandigarh, India, waliaravinder@yahoo.com

of the specimen surface due to the formation of TiC and $TiSi_2$. A Cu-Mn tool made with powder metallurgy was used for machining die steel with the EDM process utilizing the Taguchi technique [6]. Micro-hardness was increased substantially for the machined samples under optimum experimental conditions. Evaluation for micro-hardness was carried out by using different powder metallurgy tools (Cu and Mn). There was an improvement in micro-hardness by 93.7 % by the formation of cementite, ferrite and manganese carbide phases in the machined workpiece samples by utilizing a composite tool. Experiments were performed based on the L25 orthogonal array design of experiment at five different levels [7]. The machining performances were evaluated in terms of micro-hardness of the EDMed Inconel 718 end product. In this paper, a novel optimization route (combining satisfaction function, a distance measure approach in conjugation with Taguchi's philosophy) has been introduced. Graphite powder-mixed dielectric was utilized to improve machining performance on Inconel 625 [8]. The micro-hardness of AISI H13 tool steel workpiece was improved by using a molybdenum-powder-mixed dielectric medium in the EDM process [9]. The migration of molybdenum and carbon particles leads to the formation of a white layer over the machined surface in the form of Fe-Mo and MoxC, which was responsible for improved micro-hardness. A Taguchi L27 OA (orthogonal array) was utilized for optimization of process parameters and utilized chromium powder additive for experimentation on H-11 die steel in order to increase micro-hardness of machined surface via powder-mixed EDM [10]. Analysis of variance (ANOVA) was utilized along with empirical model for the optimization and prediction of micro-hardness. The Taguchi method was followed to obtain a combination of six process variables for achieving the best micro-hardness [11]. Under favourable conditions for micro-hardness, noteworthy enhancement in the percentages of carbon and tungsten was observed. The presence of hard tungsten carbide (W_2C) and cementite (Fe_3C) on the machined surface was related to the observed substantial increase in micro-hardness (~150 %). A study on the machined surface of Inconel 718 by EDM was performed and observed that the powder-mixed EDMed machined surface was enriched more with carbon element in comparison to normal EDM (without powder) [12]. This carbon enrichment further increased the micro-hardness of the machined component. The impact of SiC powder on the topography of the machined surface was studied, as was the deposition of particles and subsurface structures in PM-EDM of Ti-6Al-4V-ELI workpiece [13]. A unique material transfer mechanism exhibited better subsurface properties, such as harder and resolidified layer structure. The discharges established at the machining gap were very well balanced due to the introduction of powder particles, which resulted in improved surface properties. Taguchi's L18 mixed OA (orthogonal array) was utilized for the planning of experiments and selected machine process as well as tool parameters for study [14].Nanoparticles' high reactive surface area made better surface alloying in comparison to other tool materials and has displayed positive influence on micro-hardness on the machined surface. The generated carbides over the surface increased the micro-hardness to 912 HV. It was stated that the pyrolysis of the dielectric media was responsible for significant carbon migration at the machined surface [15]. Therefore, the EDMed specimen shows the existence of a carbon-rich surface (carbide layer). The formation of such a carbide layer results in increased micro-hardness of the specimen in comparison to that of the "as-received" parent material.

Although significant research have been performed regarding powder-mixed EDM, very limited research has been conducted in terms of parameter optimization for micro-hardness in field of PMND-EDM. Therefore a hybrid setup was developed to carry out the experiments for the desired output results. Taguchi L_9 OA was utilized for the design of experiments, which comprise four parameters at three different levels. The selected process parameters were tool diameter, mist flow rate, metallic powder concentration, and dielectric mist pressure. These selected parameters were selected based on previous literature review and their significance which affects the machining characteristics [16] and [17].

1 METHOD AND EXPERIMENTAL

The experimental setup was developed at Delhi Technological University, Delhi, India, as shown in Fig. 1. This developed setup was integrated with a Sparkonix 35A EDM machine. The setup comprises of mixing chamber (stainless steel) along with dielectric flow meter (0 ml/min to 20 ml/min) and pressure regulators. An air compressor (2H.P) has been used for the supply of pressurized dielectric mist. The mixing chamber was used for preparing a dielectric mixture of metallic conductive powder along with a minute amount of dielectric oil and high-pressure air supplied from the compressor.

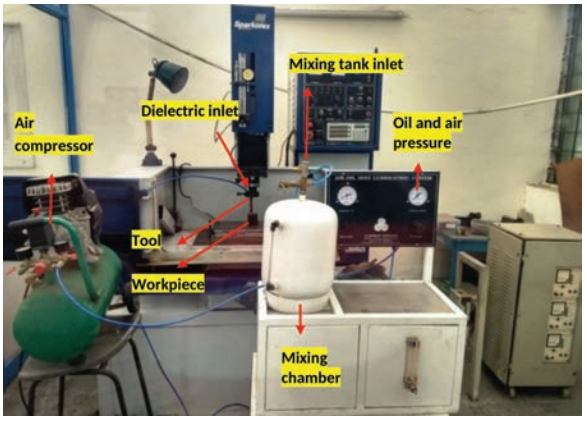

Fig. 1. *Experimental setup for PMND-EDM*

Table 1. *Experimental conditions of selected process parameters*

Symbol	Process parameters	Unit	Level 1	Level 2	Level 3
A	Tool diameter	mm	2	3	4
B	Mist flow rate	ml min^{-1}	5	10	15
C	Metallic powder concentration	g l^{-1}	15	20	25
D	Mist Pressure	MPa	0.4	0.5	0.6

*Values of other constant parameters:

Machining time 10 min; T_{on} 500 μs; T_{off} 75 μs; Discharge current 12 A; Tool electrode Copper; Workpiece EN-31, Metallic zinc powder

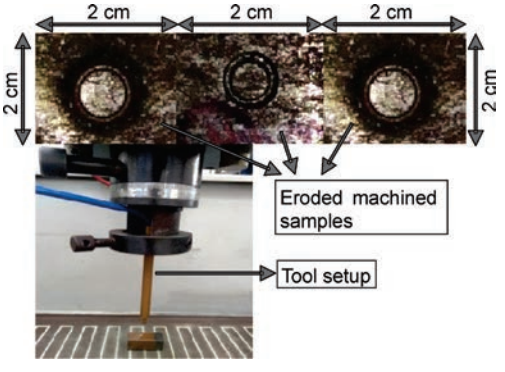

Fig. 2. *Machined samples and tool setup for PMND-EDM*

Table 2. *Chemical composition and physical properties of workpiece (EN-31)*

Chemical properties		Mechanical properties	
Element	[%]	Thermal conductivity [W $m^{-1}K^{-1}$]	44.5
Carbon	0.90 to 1.20	Hardness (HRC)	63
Silicon	0.10 to 0.35	Yield stress [MPa]	450
Manganese	0.30 to 0.75	Tensile strength [MPa]	750
Sulphur	0.050	Density [kg m^{-3}]	7850
Phosphorus	0.050	Melting point [°C]	1540

The experimental conditions for achieving maximum micro-hardness by PMND-EDM (Table 1) shows the tool specifications and selected process parameters values at different levels. The copper tool and the machined sample by PMND-EDM is shown in Fig. 2 while Table 2 shows the chemical composition and mechanical properties of the workpiece selected for experimentation.

2 RESULTS AND DISCUSSION

Micro-hardness testing for machined EN-31 samples was measured with the a Fischerscope instrument (HM2000S model) made in the USA. This instrument comprises an indenter (carbide), which indents the sample to be tested with respect to the load applied. Taguchi L_9 OA was utilized for the design of experiments and the tests for micro-hardness were performed thrice for repeatability. In Taguchi analysis, signal-to-noise (*S/N*) ratios were calculated for desired and undesired values. These output characteristics are generally of two types: higher-the-better (HB) and lower-the-better (LB). Since this study our aim aimed to increase the micro-hardness of the workpiece, the criteria to be considered is HB. The output signal to noise (*S/N*) ratio considered for HB is given by Eq. (1) while the S/N values along with output micro-hardness are given in Table 3.

S/N is a technique of measurement in science and engineering to analyse the effect on output response relative to the target or nominal value under different noise conditions[dB]. In this study, the goal is to measure micro-hardness; therefore, the noise conditions are involved during experimentation.

A total of twenty-seven experiments were performed (three repeated for each set of process parameter condition):

$$S/N\ ratio = -log_{10}\left(\frac{1}{n}\sum_{i=1}^{n}\frac{1}{y_{ij}^2}\right), \quad (1)$$

where n is number of replications; and y_{ij} observed response value.

The main effects and *S/N* ratio for average micro-hardness and pooled ANOVA are given in Tables 4 and 5, respectively, for different process parameters. The effect of input parameters at different levels on micro-hardness value (average) was plotted, as shown in Fig. 3. It was observed that process parameters at A_1, B_2, C_3, and D_3 were most significant in enhancing the micro-hardness of an EN-31 workpiece machined by PMND-EDM.

Table 3. *The experimental results for micro-hardness by PMND-EDM as per Taguchi L_9 OA*

Exp. No.	Parameter trial condition				Micro-hardness			S/N [dB]
	A	B	C	D	R1	R2	R3	
1	2	2	15	0.4	175	100.25	338.93	41.52
2	2	5	20	0.5	450	350.78	345.08	49.69
3	2	8	25	0.6	505.63	501.78	540.89	52.47
4	3	5	15	0.6	59.37	45.96	50.26	32.39
5	3	8	20	0.4	112.23	259	189	42.13
6	3	2	25	0.5	132.23	55.63	62.38	34.96
7	4	8	15	0.5	148.96	192.85	200.56	43.15
8	4	2	20	0.6	237	215	350.22	46.23
9	4	5	25	0.4	201	222.37	245	45.11

Overall mean Vickers micro-hardness ($\overline{HV}$) = 232.86
load of micro-hardness measurements 300 N / 20 s

The force applied for micro-hardness testing was 300 N / 20 s with the Fischer micro-hardness machine. The other results obtained were indentation modulus, mean value, confidence interval, and range for micro-hardness value. Parameter A (Tool type) at Level 1 was most significant in increasing the micro-hardness value of the machined EN-31 sample, as shown in Fig. 3a. At this level, the dielectric medium dispersion from the tool tip was found to be very suitable. Due to this proper dispersion, stable discharging was observed at the inter-electrode gap (IEG), which results in higher values of micro-hardness. The signal-to-noise ratio (*S/N*) in the graph also shows the same trend. Furthermore, the flow rate was found to be most influential at 2nd level in increasing the micro-hardness value, as shown in Fig. 3b. At this level, the flow rate of the dielectric medium at 10ml/min was optimum in providing suitable normal discharges at the machining zone along with powder additives, which results in a higher value of micro-hardness. The micro-hardness value was found to be highest at the 3rd level of powder additive (metallic) concentration (25 g/l), as shown by the trend of plot in Fig. 3c. The micro-hardness value increased with respect to the increase in metallic powder concentration, which can be observed in Fig. 3c. A zinc carbide (ZnC) hard layer was formed over the top surface of the workpiece due to rich amount of zinc deposition at the melting and resolidification zone over the surface of the sample (Fig. 4). As stated, the pyrolysis of dielectric results in diffusion of oxygen and carbon, which also results in the formation of hard carbides and oxides over the top layer of the machined workpiece [18]. All these factors resulted in achieving the best micro-hardness value at the 3rd level of the process parameter. Dielectric mist pressure at the 3rd level (0.6 MPa) was most

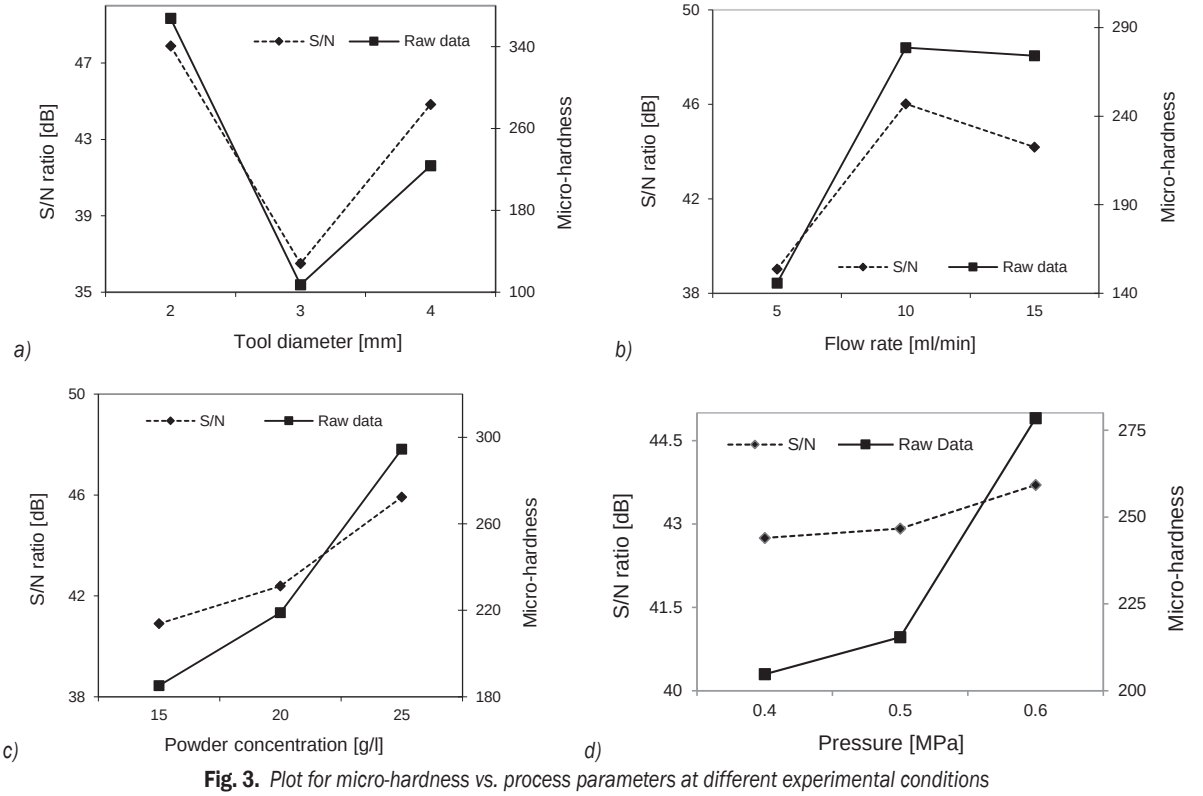

Fig. 3. *Plot for micro-hardness vs. process parameters at different experimental conditions*

significant in enhancing the micro-hardness value, as shown in Fig. 3d, and the *S/N* also shows the same trend in the plot. The trend displayed shows that the micro-hardness value increased with increase in the mist flow pressure. The excellent debris removal and cooling effect over the machined sample at this mist pressure resulted in achieving the maximum micro-hardness value at the sample surface.

The microstructure of the machined workpiece changes with there-crystallization phenomenon due to rapid heating and cooling during the machining process [19]. The shape of the material grains and, subsequently, the surface properties of the machined workpiece are determined by the heating and cooling rates.

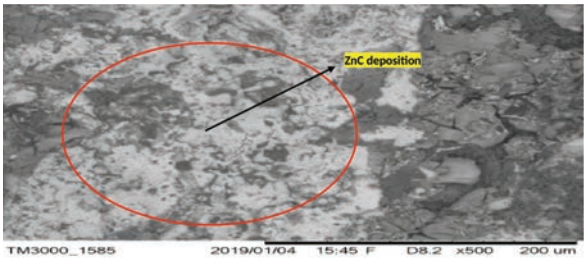

Fig. 4. *ZnC layer formation over the machined sample*

The average depth of the measured eroded holes (60 µm) of the machined workpiece was measured with the help of vision inspection instrument. The cross-section of the machined surface was also analysed for the study of micro-hardness. Fig. 5 shows the recast layer at the top altered surface due to the melting and resolidification of the molten material. Due to changes in chemical composition and rapid cooling by flushing, there was a metallurgical structural change. A heat-affected zone was found below the recast layer due to heat generated by the plasma at the inter-electrode gap (IEG).

The white layer indicated the metallographic phase due to adequate carbon present, which results in the formation of ZnC deposits (10 µm) along with the solidified molten material while comparison was also made with the machined sample without metallic powder, and there was a negligible metallurgical transformation as shown in Fig. 6.

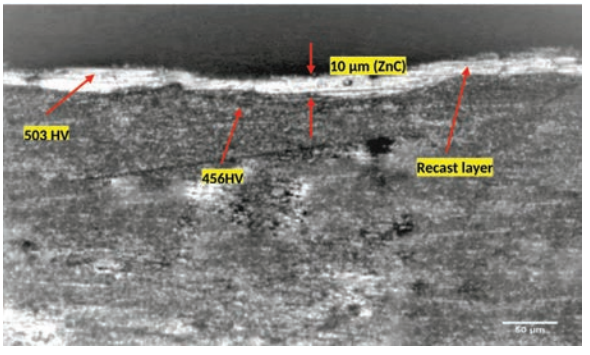

Fig. 5. *SEM micrograph of cross section with average values of micro-hardness*

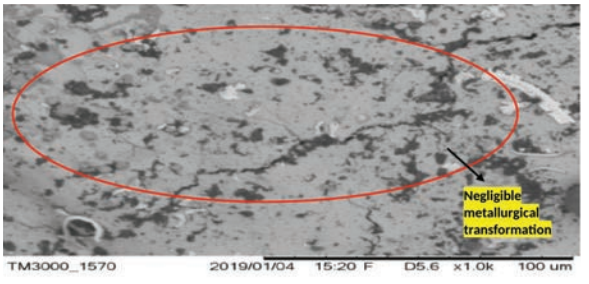

Fig. 6. *SEM micrograph of machined sample by EDM without metallic powder*

Scanning electron microscopy was performed for further analysis of the machined workpieces. Zinc metallic powder deposits at the resolidification process over the machined surface can be seen in Fig. 7 at different magnification factors. Metallic powder (zinc) in the dielectric and molten material migration

Table 4. *Main effects table for micro-hardness*

Process parameter	Level	Tool diameter (A)		Flow rate (B)		Powder concentration (C)		Pressure(D)	
Type of data		S/N Ratio	Raw data	S/N Ratio	Raw data	S/N Ratio	Raw data	S/N Ratio	Raw data
Average values (% micro-hardness)	L1	47.8	367.5	39	145.7	40.9	185.1	42.9	204.7
	L2	36.4	107.3	46	278.7	42.3	218.8	42.6	215.3
	L3	44.8	223.6	44.1	274.1	45.9	294.5	43.7	278.4
Main effects (% micro-hardness)	L2 – L1	–11.3	–260.2	6.9	132.9	1.4	33.6	–0.3	10.6
	L3 – L2	8.3	116.3	–1.8	–4.6	3.5	75.6	1.0	63.0
Differences (L3 – L2) – (L2 – L1)		19.7	376.5	–8.8	–137.5	2.0	41.9	1.4	52.4

*L1, L2, L3 represent levels 1, 2 and 3 respectively of parameters. (L2 – L1) is the average main effect when the corresponding parameter changes from Level 1 to Level 2. (L3 – L2) is the main effect when the corresponding parameter changes from Level 2 to Level 3.

Table 5. *Pooled ANOVA raw data and S/N data for micro-hardness*

Source	SS raw	SS S/N	DOF raw	DOF S/N	V raw	V S/N	F-ratio Raw	F-ratio S/N	SS' raw	SS' S/N	P% raw	P% S/N
Tool diameter	305936.46	208.81	2	2	152968.2	104.40	42.21	109.04	298690.1	206.90	53.46	62.78
Flow rate	102445.57	79.03	2	2	51222.78	39.51	14.13	41.27	95199.25	77.12	17.04	23.40
Powder concentration	56465.03	39.77	2	2	28232.52	19.88	7.79	20.76	49218.71	37.85	8.81	11.48
Pressure	28569.57	*	2	*	14284.79	*	3.94	-	21323.25	*	3.81	*
Error	65216.86	1.91	18	2	3623.15	0.95	-	-	94202.14	7.65	16.86	2.32
Total	558633.51	329.54	26	8	-	-	-	-	558633.5	329.54	100	100

* Significant at 95 % confidence level, F critical (raw) = 3.55 (tabular value), F critical (S/N) =19 (tabular value), SS – Sum of Squares, DOF – Degree of Freedom, V – Variance, SS' – Pure sum of Squares P – Probability of obtaining the observed results of a test

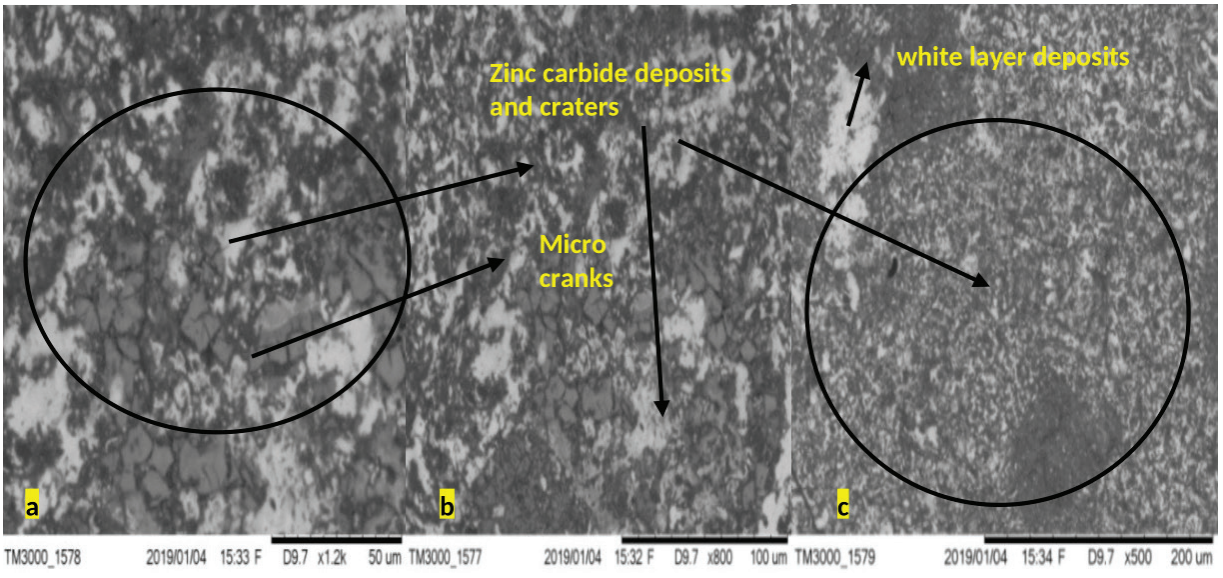

Fig. 7. *SEM images of zinc deposits over the machined EN-31 sample by PMND-EDM at different magnification factors*

from the tool electrode was also responsible for changes in the microstructure. Another observation was that the crater size was greater over the machined surface. A white layer of ZnC was formed and remained stable over the machined surface. This fine-grained hard white layer was alloyed with molten material deposited from the tool electrode.

The hardest dark layer was seen at the top surface of the machined sample (Fig. 7). Dendritic features confronts that the phase transformation was also observed beneath the dark layer [13]. The alpha (α) phase of white layer occurred in the molten liquid phase. Primary discharges led to the formation of large craters, and pebble-type features were developed due to secondary discharges. Further increases in powder concentration also lead to the formation of small craters.

2.1 Estimation of Performance Characteristics (Micro-Hardness)

Micro-hardness response characteristics can be determined using Eq. (2), [20] and [21] as:

$$Micro-hardness = \overline{A}_1 + \overline{B}_2 + \overline{C}_3 + \overline{D}_3 - 3\overline{HV} = 520.7\ HV. \quad (2)$$

The confidence interval of confirmation experiments can be determined using Eq. (3):

$$CI_{CE} = \sqrt{F_\alpha(1, f_e)V_e\left[\frac{1}{n_{eff}} + \frac{1}{R}\right]} = 75.65. \quad (3)$$

The confidence interval of the population can be determined by Eq. (4):

$$CI_{pop} = \sqrt{F_\alpha(1, f_e)V_e / n_{eff}} = 37.82, \quad (4)$$

where, $F_\alpha(1, f_e)$ is the F ratio at the confidence level of $(1 - \alpha)$ against DOF 1.

$$F_{0.05}(1, 18) = 3.5546 \text{ (Tabulated)},$$

$$n_{eff} = \frac{N}{1 + \left[\begin{array}{c}\text{DOF associted in the estimate} \\ \text{of mean response}\end{array}\right]} = 9,$$

where N is the total number of experiments (N = 27)*;* treatment is 9, repetition 3, and sample size for confirmation experiments, R = 3.

V_e, error variance = 3623.15 (Table 5),

f_e, error DOF = 18 (Table 5),

F = 3.5546 (tabulated F value),

where

$$F = \frac{\text{Variation between sample means}}{\text{Variation within the samples}}.$$

This F value is compared with the F limit for respective DOF. If F value is equal to or greater than the F-limit value (seen in Table 5), it can be said that significant differences exist between the sample means.

Therefore, micro-hardness is 520.7,

$CI_{CE} = \pm 75.65$, $CI_{POP} = \pm 37.82$

The predicted optimal range of confidence interval of conformation experiments (CI_{CE}) is:

$$\left[\begin{array}{c}\text{Mean} \\ \text{micro-} \\ \text{hardness}\end{array}\right] - CI_{CE} < \left[\begin{array}{c}\text{micro-} \\ \text{hardness}\end{array}\right] < \left[\begin{array}{c}\text{Mean} \\ \text{micro-} \\ \text{hardness}\end{array}\right] + CI_{CE},$$

i.e. 445.05 < micro-hardness < 596.35.

The 95 % conformation interval of the predicted mean is:

$$\left[\begin{array}{c}\text{Mean} \\ \text{micro-} \\ \text{hardness}\end{array}\right] - CI_{POP} < \left[\begin{array}{c}\text{micro-} \\ \text{hardness}\end{array}\right] < \left[\begin{array}{c}\text{Mean} \\ \text{micro-} \\ \text{hardness}\end{array}\right] + CI_{POP},$$

i.e. 482.88 < micro-hardness < 558.52.

The confirmation tests for micro-hardness were performed by setting machining conditions at the optimal process parameters values given below:

- Tool diameter at level 1 (2 mm);
- Flow rate at level 2 (10 ml/min);
- Powder concentration at level 3 (25 g/l);
- Dielectric mist pressure at level 3 (0.6 MPa);

The confirmation tests were run thrice to obtain the average value in order to reduce the percentage error in experimentations. The micro-hardness values achieved were 449.30 HV, 510.39 HV, and 560.21 HV respectively for the three trials and the average value was 506.63 HV.

(ISO standard: Vickers hardness numbers are reported as 506.63 HV 300 N / 20 seconds, where C (loading time) = 5 s indicates the time if it differs from 10 s to 15 s).

2.2 Confirmation Experiments

The confirmation test was performed for micro-hardness at A_1, B_2, C_3, and D_3 experimental conditions. The mean micro-hardness calculated was 506.21 HV which lies within the confidence interval of predicted micro-hardness.

2.3 Analysis for TWR

The decrease in TWR was 18.80 % by PMND-EDM as compared to near dry EDM (i.e., without metallic powder), as shown in Fig. 8.

The TWR (mg/min) was measured with the formula:

$$TWR = (T_i - T_f) / T_{m,}$$

where T_i is the initial weight of the tool, T_f is the final weight of tool, and T_m is the machining time.

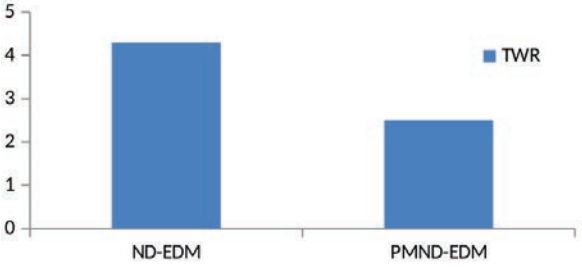

Fig. 8. *Comparison for TWR between near dry EDM and PMND-EDM*

The addition of conductive metallic powder leads to reduced breakdown voltage and increase in the interspace between the electrodes for electric discharge **[22]**. This phenomenon improves the stability of the machining process that caused a reduction in TWR. The dielectric fluid (LL-221) with added conductive powder has improved the efficiency of electrical discharging at the spark gap, preventing the tool electrode tip from further wear, as shown in Fig. 9.

Heat dissipation was improved because the phenomena of abnormal discharge and short circuit were minimized. The amount of heat conducted to the tool was also reduced due to proper heat dissipation. This makes the material temperature go below its melting point, which consequently reduces TWR [16].

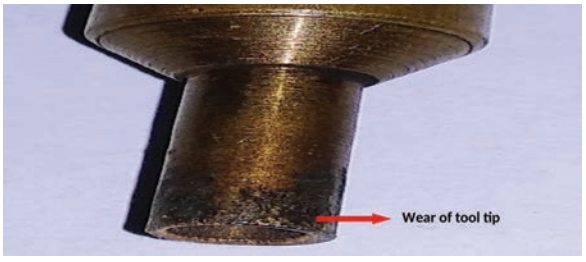

Fig. 9. *Wear of tool electrodes tip after PMND-EDM process*

3 CONCLUSIONS

This paper included investigations on micro-hardness of machined EN-31 samples by utilizing Taguchi L_9OA; a further ANOVA technique was implemented to study the effects of different process parameters on output response micro-hardness. The conclusions drawn after the research are as follows:

- It was concluded that the PMND-EDM method of machining at optimum input process parameters leads to the generation of machined parts with higher micro-hardness values.
- The requirement of a large quantity of dielectric oil was eliminated as only a minute amount of dielectric oil was required for machining hard metals.
- It was observed that optimum parameter condition at A1, B2, C3, and D3 were most dominant in achieving the maximum micro-hardness of machined EN-31 die steel workpiece.
- Confirmation experiments revealed that the highest value of micro-hardness was found to be 506.63 HV at optimized input process parameters.
- The predicted optimal range of confidence interval of conformation experiments (CICE) for micro-hardness was: 445.05 < micro-hardness < 596.35.
- The 95 % conformation interval of the predicted mean for micro-hardness was: 482.88 < micro-hardness < 558.52.
- A layer of hard zinc carbide hard was deposited over the surface of the machined sample which leads to a higher value of micro-hardness.
- The experimental results were validated by confirmation of experiments, and the obtained output results were within the permissible results.
- The metallic powder additives aids in the generation of a stable and more energized spark due to increased thermal conductivity at the inter-electrode gap.

4 REFERENCES

[1] Zhao, W.S., Meng, Q.G.,Wang, Z.L. (2002). The application of research on powder mixed EDM in rough machining. *Journal of Materials Processing Technology*, vol. 129, no. 1-3, p. 30-33, **DOI:10.1016/S0924-0136(02)00570-8**.

[2] Gao, Q., Zhang, Q.H., Zhang, J.H. (2009). Experimental study of powder-mixed near dry electrical discharge machining. *Chinese Journal of Mechanical Engineering,* vol. 45, no. 1, p.169-175, **DOI: 10.3901/JME.2009.11.169**.

[3] Kumar, S., Batra, U. (2012). Surface modification of die steel materials by EDM method using tungsten powder-mixed dielectric. *Journal of Manufacturing Processes*, vol. 14, no. 1, p. 35-40, **DOI:10.1016/j.jmapro.2011.09.002**.

[4] Zain, Z.M., Ndakiman, M.B., Khan, A.A., Ali, M.Y. (2014). Improving micro-hardness of stainless steel through powder-mixed electrical discharge machining. *Proceedings of the Institution of Mechanical Engineers, Part C: Journal of Mechanical Engineering Science*, vol. 228, no. 18, p. 3374-3380, **DOI:10.1177/0954406214530872**.

[5] Li, L., Zhao, L., Li, Z.Y., Feng, L., Bai, X. (2016).Surface characteristics of Ti-6Al-4V by SiC abrasive-mixed EDM with magnetic stirring. *Materials and Manufacturing Processes*, vol. 32, no. 1, p. 83-86, **DOI:10.1080/10426914.2016.1151043**.

[6] Gill, A.S., Kumar, S. (2016). Surface roughness and micro-hardness evaluation for EDM with Cu-Mn powder metallurgy tool. *Materials and Manufacturing Processes*, vol. 31, no. 4, p. 514-521, **DOI:10.1080/10426914.2015.1070412**.

[7] Rahul, Datta, S., Biswal, B.B., Mahapatra, S.S. (2017). A novel satisfaction function and distance-based approach for machining performance optimization during electro-discharge machining on super alloy Inconel 718. *Arabian Journal for Science and Engineering*, vol. 42, no. 5, p. 1999-2020, **DOI:10.1007/s13369-017-2422-5**.

[8] Talla, G., Gangopadhyay, S., Biswas, C.K. (2017). Influence of graphite powder mixed EDM on the surface integrity characteristics of Inconel 625. *Particulate Science and Technology*, vol. 35, no. 2, p. 219-226, **DOI:10.1080/02726351.2016.1150371**.

[9] Amorim, F.L., Dalcin, V.A., Soares, P., Mendes, L.A. (2017). Surface modification of tool steel by electrical discharge machining with molybdenum powder mixed in dielectric fluid. *The International Journal of Advanced Manufacturing Technology*, vol. 91, no. 1-4, p. 341-350, **DOI:10.1007/s00170-016-9678-x**.

[10] Tripathy, S., Tripathy, D.K. (2017). An approach for increasing the micro-hardness in electrical discharge machining by adding conductive powder to the dielectric. *Materials Today:*

Proceedings, vol. 4, no. 2, p. 1215-1224, **DOI:10.1016/j.matpr.2017.01.140**.

[11] Gill, A.S., Kumar, S. (2018). Investigation of micro-hardness in electrical discharge alloying of En31 tool steel with Cu–W powder metallurgy electrode. *Arabian Journal for Science and Engineering*, vol. 43, no. 3, p. 1499-1510, **DOI:10.1007/s13369-017-2960-x**.

[12] Sahu, S.K., Jadam, T., Datta, S., Dhupal, D., Nandi, G. (2018). Application of SiC power added in kerosene dielectric media for electro-discharge machining of Inconel 718 super alloys: effect of powder concentration. *Materials Today: Proceedings*, vol. 5, no. 9, p. 20297-20305, **DOI:10.1016/j.matpr.2018.06.402**.

[13] Öpöz, T.T., Yaşar, H., Ekmekci, N., Ekmekci, B. (2018). Particle migration and surface modification on Ti6Al4V in SiC powder mixed electrical discharge machining. *Journal of Manufacturing Processes*, vol. 31, p. 744-758, **DOI:10.1016/j.jmapro.2018.01.002**.

[14] Chundru, V.R., Koona, R., Pujari, S.R. (2018). Surface modification of Ti6Al4V alloy using EDMed electrode made with nano- and micron-sized TiC/Cu powder particles. *Arabian Journal for Science and Engineering*, vol. 44, no. 2, p. 1425-1436, **DOI:10.1007/s13369-018-3561-z**.

[15] Kumar, M., Datta, S., Kumar, R. (2019). Electro-discharge machining performance of Ti–6Al–4V alloy: Studies on parametric effect and phenomenon of electrode wear. *Arabian Journal for Science and Engineering*, vol. 44, no. 2, p. 1553-1568, **DOI:10.1007/s13369-018-3632-1**.

[16] Bai, X., Zhang, Q.H., Yang, T., Zhang, J.H., Tan, J. (2013). Research on tool wear rate of powder mixed near dry electrical discharge machining. *Advanced Materials Research*, vol. 652-654, p. 2222-2227, **DOI:10.4028/www.scientific.net/AMR.652-654.2222**.

[17] Yuvaraj, T., Suresh, P. (2019). Analysis of EDM process parameters on Inconel 718 using the grey-Taguchi and TOPSIS methods. *Strojniški vestnik – Journal of Mechanical Engineering*, vol. 65, no. 10, p. 557-564, **DOI:10.5545/sv-jme.2019.6194**.

[18] Talla, G., Gangopadhyay, S., Biswas, C.K. (2016).Effect of powder- suspended dielectric on the EDM characteristics of Inconel 625. *Journal of Material Engineering and Performances*, vol. 25, no. 2, p. 704-717, **DOI:10.1007/s11665-015-1835-0**.

[19] Singh, G., Singh, G., Singh, K., Singla, A. (2017). Experimental studies on material removal rate, tool wear rate and surface properties of machined surface by powder mixed electric discharge machining. *Materials Today: Proceedings*, vol. 4, no. 2, p. 1065-1073, **DOI:10.1016/j.matpr.2017.01.121**.

[20] Walia, R.S., Shan, H.S., Kumar, P. (2006). Multi-response optimization of CFAAFM process through Taguchi method and utility concept. *Materials and Manufacturing Processes*, vol. 21, no. 8, p. 907-914, **DOI:10.1080/10426910600837814**.

[21] Brar, B.S., Walia, R.S., Singh, V.P. (2015). Electrochemical-aided abrasive flow machining (ECA2 FM) process: a hybrid machining process. *International Journal of Advanced Manufacturing Technology*, vol. 79, no. 1-4, p. 329-342, **DOI:10.1007/s00170-015-6806-y**.

[22] Jeswani, M.L. (1981). Effects of the addition of graphite powder to kerosene used as the dielectric fluid in electrical discharge machining. *Wear*, vol. 70, no. 2, p. 133-139, **DOI:10.1016/0043-1648(81)90148-4**.Valibunu estiust arbit. Viverimur potebus octus, nont? Urorbis, nos, quit. Ivivena,

Strojniški vestnik - Journal of Mechanical Engineering 66(2020)3, 193-202

DOI:10.5545/sv-jme.2019.6302 Original Scientific Paper
Received for review: 2019-08-29
Received revised form: 2019-12-27
Accepted for publication: 2020-02-13

Power-Following Control Strategy of a Wheel-Drive Hydraulic Hybrid Vehicle

Tao Zhang – Qiang Wang – Xiao-Hui He* – Si-Sheng Li – Xin-Min Shen
PLA Army Engineering University, College of Field Engineering, China

Energy management strategy is a critical technology for improving the fuel economy of wheel-drive hydraulic hybrid vehicles. For driving, a power-following control strategy is proposed in this study by adding several working points of the engine in the optimal fuel economy power curve. For braking, the "I" curve distribution strategy based on critical braking strength z_{min} was adopted. A test bench was constructed according to the quarter of the prototype vehicle. Taking the typical working conditions of Federal Urban Driving Schedule (FUDS) and the self-set extra-urban driving schedule (EUDC-1) cycle condition into consideration, the energy management strategy was studied. The torque and speed of the simulated engine and pressure of the accumulator were obtained. The test fuel consumption in this research was compared with the original fuel consumption of the prototype vehicle. It was found that the proposed energy management strategy could effectively improve the fuel economy by more than 24 % under the requirement of satisfying the dynamic performance of the whole vehicle.
Keywords: wheel-drive hydraulic hybrid vehicle, power-following control strategy, braking force distribution strategy, drive cycle, fuel economy

Highlights

- *A power-following control strategy was proposed by adding several working points of the engine in the optimal fuel economy power curve.*
- *The "I" curve distribution strategy based on the critical braking strength zmin was adopted.*
- *The energy management strategy in this study satisfied the dynamic performance of the whole vehicle.*
- *Results showed that the proposed energy management strategy could improve the fuel economy by more than 24 % in the test bench.*

0 INTRODUCTION

The secondary regulation technology for the constant pressure network was introduced and applied to a hybrid tactical vehicle including the series connections of an internal combustion engine (ICE), hydraulic pump, and the novel hydraulic pump/motor. The wheel-drive technology was used to improve the ground clearance of vehicle chassis [1], and the fuel economy of the vehicle could be improved by using the appropriate energy management strategy.

Currently, most of the energy management strategies of the hydraulic hybrid vehicles come from related research about hybrid electric vehicles [2] to [8]. Because of being controlled simply and applied conveniently, the rule-based energy management strategy is the most widely used one among them. The main idea of the strategy is to judge the working area of the ICE and switch the working modes of the vehicle, in order to make the ICE run in an efficient manner corresponding to controller variables (including the power demand, speed of the vehicle, and the accumulator state of charge (*SOC*), etc.) [2]. For a wheel-drive hydraulic hybrid vehicle (WDHHV), because of the small energy density and high power density of the accumulator, the engine usually worked in the frequent start-stop state, which hindered the improvement of the fuel economy of the vehicle [3]. For the control strategy of the accumulator *SOC*, according to the characteristics of the low power density of the accumulator, the main parameter accumulator SOC_{max} and SOC_{min} of this strategy were optimized, and it was found that when the parameters were 0.7 and 0.1, respectively, the fuel economy could be increased by more than 30 %, although the dynamic performance of the system was not so good [4]. For the control strategy of the engine state, the power-following control strategy was proposed by Song et al. for a series of electric drive bulldozers based on typical operating conditions [5]. The results indicated that not only was the dynamic performance of the bulldozer satisfied, but the fuel economy also was increased by 13.1 %.

1 METHODS

In this study, according to their characters, two control strategies were selected for WDHHV. For driving, a power-following control strategy was proposed for adding several engine working points in the optimal fuel economy power curve of the ICE. For braking, considering the minimum braking force that could be

*Corr. Author's Address: PLA Army Engineering University, Nanjing, China, gcbhxh@qq.com

provided through the variable displacement motor/pump and *SOC* of the accumulator [6], the "I" curve distribution strategy based on critical braking strength z_{min} was adopted to fully recover the braking energy. At present, most of the research on the energy management strategy of the WDHHV has remained in the simulation stage [3], [7] to [9], which is not sufficiently credible for practical application. To conduct the study, a test bench was built, on which an electric motor was used to simulate the ICE. Meanwhile, the motor energy consumption was converted into the ICE fuel consumption, measuring on one-hundred-kilometres and was compared with that of the prototype vehicle.

2 CONFIGURATION

Configuration of the WDHHV was shown in Fig. 1. It included ICE (diesel engine), constant pressure variable pump, high-voltage accumulator, low-voltage accumulator (replace tank), direction control valves, hydraulic variable displacement motor/pump, wheels, vehicle controller, and so on.

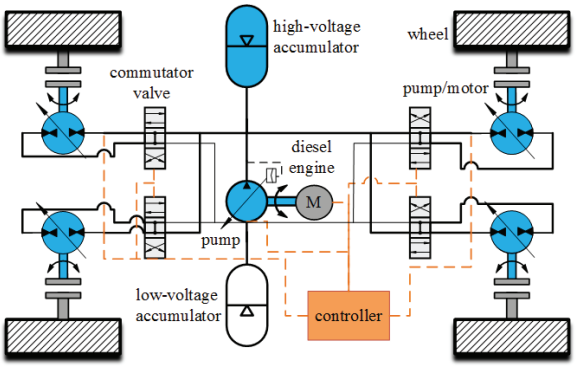

Fig. 1. *Configuration of the WDHHV*

The ICE directly drives the pump, which adjusts the displacement to maintain the constant pressure of the system [10]. Therefore, the ICE working condition is independent of the external load to work in the area with high fuel economy [11]. Each wheel is driven independently by a hydraulic motor/pump, which can work in four quadrants. In the driving phase, the accumulator acts as the auxiliary power source. The hydraulic motor/pump is working in the "motor" state and converts the hydraulic energy into the mechanical energy, and the vehicle can achieve infinite speed regulation by adjusting the displacement of the hydraulic motor/pump. In the braking phase, the hydraulic motor/pump works in the "pump" state and converts the kinetic energy of the vehicle into the hydraulic energy stored in the accumulator, which can be released and reused in the driving phase [12].

3 CONTROL SYRATEGIES

3.1 Drive Strategy

According to the configuration of WDHHV in Fig. 1, there are two power sources (the engine and the accumulator) and two braking methods (regenerative braking and friction braking). We can make six working modes of the vehicle, which are shown in Table 1 [13].

Table 1. *Working modes of the vehicle*

	Working modes
1	Accumulator drive mode
2	Engine drive mode
3	Accumulator+ Engine drive mode
4	Friction braking
5	Regenerative braking
6	Friction+ Regenerative braking

The engine model adopts the experimental modelling, and brake-specific fuel consumption (BSFC) is obtained by the interpolation based on the actual engine experimental data provided by the manufacturer. Fuel consumption of the engine can be obtained according to Eq. (1) [14].

$$B = \int g_e P_e dt = \int T_e n_e f(T_e, n_e) dt, \tag{1}$$

where B is the fuel consumption [g], P_e is the engine power [kW], and g_e is fuel consumption rate [g/(kW·h)].

According to the real-time state of the vehicle (power demand, vehicle speed, accumulator *SOC*) and energy allocation strategy, the target required power of the engine can be obtained at each sampling time. Since there is an energy coupling relationship between the engine and load, there is no longer a direct mechanical relationship between the engine speed and the vehicle speed. Therefore, the engine can work in the optimal fuel consumption curves preset according to the power demand and the universal characteristic of engine [15]. The strategy could effectively avoid the frequent ICE dynamic switching, so that the ICE works on the minimum fuel consumption curve and switches to a reasonable mode of the operation. The engine regulation rules are shown in Fig. 2.

In Fig. 2 P_{req} and P_{max} are the power required and the maximum power of the engine, respectively. P_{BSFC} are the candidate operating points in Fig. 3.

IF: $SOC < SOC_{min}$,
Then: *engine* = on
IF: $SOC > SOC_{max}$,
Then: *engine* = false
IF: *engine* = on,
Then $P_{req} = P_{BSFC}$;
IF: ($P_{req} > P_{max}$) &&
($SOC < SOC_{min}$)
Then: $P_{req} = P_{max}$
Or else: $P_{req} = 0$

Fig. 2. *Engine regulation rules*

At the same time, many studies [16] to [19] on the hybrid vehicles showed that the engine works in the start-stop mode, which was beneficial to fuel economy. Therefore, the engine start-stop mode was selected. The optimal fuel economy curve of the engine was shown in Fig. 3.

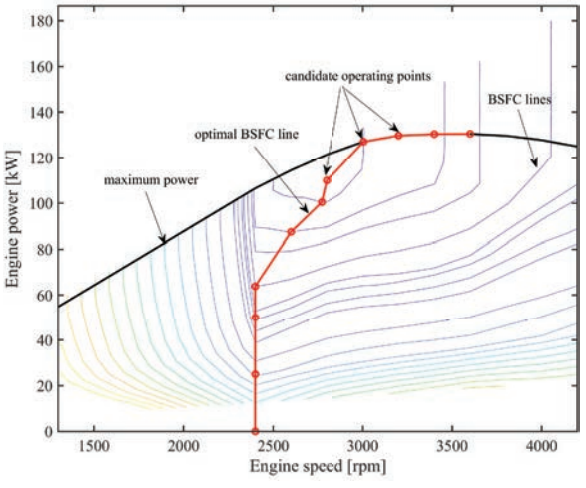

Fig. 3. *Optimal fuel economy curve of the engine*

3.2 Braking Strategy

There are two kinds of braking modes in the WDHHV: regenerative braking and friction braking [20]. Regenerative braking is to make hydraulic motor/pump work in the "pump" state to achieve energy recovery and braking. Friction braking sheets are used to brake the vehicle in the form of heat dissipation. The braking strategy is to reasonably configure the two braking modes to fully recover the braking energy under the premise of satisfying the braking performance requirement of the vehicle [21].

In this study, an "I" curve control strategy based on the critical braking strength z_{min} was adopted [22]. The top-level block diagram of the braking control strategy is shown in Fig. 4.

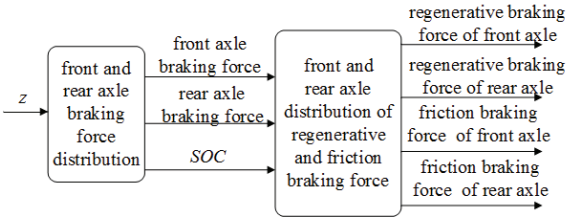

Fig. 4. *Schematic diagram of braking control strategy*

The ideal relationship curve of the front and rear wheel braking force was called the "I" curve, that is, the ideal braking power distribution curve, as shown in the Fig. 5. At this time, the braking stability and adhesion conditions were better utilized [23], and the front and rear axle braking force are shown in Eqs. (2) and (3) respectively.

$$G\varphi = F_{\mu 1} + F_{\mu 2}, \tag{2}$$

$$\frac{F_{\mu 1}}{F_{\mu 2}} = \frac{b + \varphi h_g}{a - \varphi h_g}, \tag{3}$$

$$F_{\mu 2} = \frac{1}{2}\left[\frac{G}{h_g}\sqrt{b^2 + \frac{4h_g L}{G}F_{\mu 1}} - \left(\frac{Gb}{h_g} + 2F_{\mu 1}\right)\right], \tag{4}$$

where $F_{\mu 1}$ and $F_{\mu 2}$ are the front and rear axle braking force respectively [N]; G is gravity of the vehicle [N]; h_g is the height of mass centre [m]; a and b are the distance from mass centre to rear axle and to front rear, respectively [m]; L is the distance between the shafts [m] and φ is the adhesion coefficient on road surface [-].

The actual braking forces of the front and rear axle were generally composed of the friction braking force and regenerative braking force. To maximize the recovery of braking energy, the variable motor/pump braking mode should be considered first. If requirements of the front (or rear) shaft were less than the motor braking force, the variable displacement motor/pump acted as a pump while mechanical braking did not work, as shown in point in Fig. 5. If the demand braking force of the front (or the rear) shaft was larger than that of the braking force of the motor/pump, the latter produced the maximum braking force, and the remaining part of the braking force was supplemented by friction braking, as shown of point c in the Fig. 5.

$$F_m = \frac{T_w}{r}, \tag{5}$$

$$T_w = \frac{\Delta PV}{2\pi}, \tag{6}$$

where F_m is the brake force of wheels [N]; T_w is the brake torque of wheels, [N·m]; ΔP is the pressure drop of the variable displacement motor/pump [Pa]; V is the displacement of the motor/pump [m^3/r], and r is the radius of wheels [m].

Then the minimum regenerative braking power of the front axle is shown in Eq. (7):

$$F_{\mu 1} = \frac{\Delta PV}{\pi r}. \tag{7}$$

With this method, Eqs. (8) and (9) could be obtained.

$$\frac{F_{\mu 1}}{G} = 0.18, \tag{8}$$

$$\frac{F_{\mu 2}}{G} = 0.17. \tag{9}$$

Thus, the critical braking strength is z_{min} = 0.35, as is shown in point b in Fig. 5.

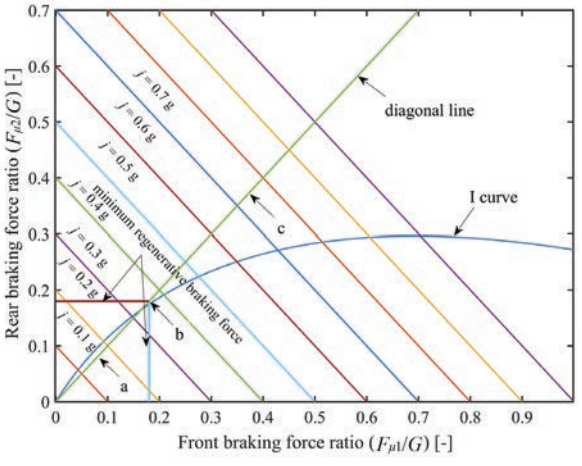

Fig. 5. *Ideal front and rear axle braking force distribution curve*

Combined with critical braking strength z_{min}, the braking strategy based on the "I" curve is distributed as follows.

(1) z < 0.35, regenerative braking. Friction braking did not participate in the work, and the front and rear braking forces were distributed according to the "I" curve.

$$\begin{cases} Gz = F_{\mu 1} + F_{\mu 2} \\ \dfrac{F_{\mu 1}}{F_{\mu 2}} = \dfrac{b + \varphi h_g}{a - \varphi h_g} \end{cases}, \tag{10}$$

$$\begin{cases} F_{\mu 1m} = 0 \\ F_{\mu 2m} = 0 \end{cases}, \tag{11}$$

where $F_{\mu 1m}$ and $F_{\mu 2m}$ are the front and rear axle friction braking force, respectively [N].

(2) 0.35 < z < 0.7, mixed braking. Firstly, considering regenerative braking, the insufficient part was supplied by friction braking.

$$\begin{cases} Gz = F_{\mu 1} + F_{\mu 2} \\ \dfrac{F_{\mu 1}}{F_{\mu 2}} = \dfrac{b + \varphi h_g}{a - \varphi h_g} \end{cases}, \tag{12}$$

$$\begin{cases} F_{\mu 1m} = F_{\mu 1} - F_{\mu 1p/m} \\ F_{\mu 2m} = F_{\mu 2} - F_{\mu 2p/m} \end{cases}, \tag{13}$$

where $F_{\mu 1m/p}$ and $F_{\mu 2m/p}$ are the front and rear axle regenerative braking force, respectively [N].

(3) z > 0.7, friction braking. Take the maximum friction braking force with the ground adhesion coefficient 0.7, and the front and rear braking force were distributed according to the "I" curve.

$$\begin{cases} G \times 0.7 = F_{\mu 1} + F_{\mu 2} \\ \dfrac{F_{\mu 1}}{F_{\mu 2}} = \dfrac{b + \varphi h_g}{a - \varphi h_g} \end{cases}, \tag{14}$$

$$\begin{cases} F_{\mu 1p/m} = 0 \\ F_{\mu 2p/m} = 0 \end{cases}. \tag{15}$$

The maximum braking force of the front axle was 8748 N, and the maximum braking force of the rear axle was 5760 N.

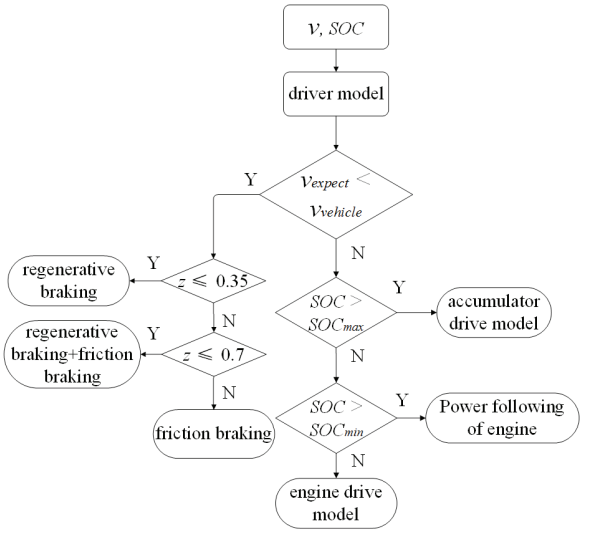

Fig. 6. *Energy management control strategy*

The ICE adjustment strategy and working modes switching rules were shown in Fig. 6. In the flowchart, z was the braking strength.

$$z = \frac{a_1}{g}, \tag{16}$$

where a_1 is the brake deceleration [m/s²]; g is the gravity acceleration [m/s²]. The upper and lower limits of the accumulator SOC_{max} and SOC_{min} are 0.6 and 0.2, respectively [4].

$$SOC = \frac{P_c - P_{\min}}{P_{\max} - P_{\min}}, \tag{17}$$

where P_c is the current pressure of the air cavity of the accumulator [bar]; $P_{\max}$ and $P_{\min}$ are the maximum and minimum allowable working pressures of the accumulator respectively [bar].

4 EXPERIMENTAL

The adopted test method was the cyclic fuel consumption method, which referred to the fuel consumption of the vehicle at a certain speed, as well as acceleration and deceleration on a specified typical road section. The test bench used the motor instead of the ICE as the power source. Therefore, the electric power consumption of the motor must be converted into ICE fuel consumption on a one-hundred-kilometre route and then compared with the prototype vehicle.

4.1 Test Bench

The test bench was based on one quarter of the prototype vehicle, and the hydraulic system was shown in Fig. 7.

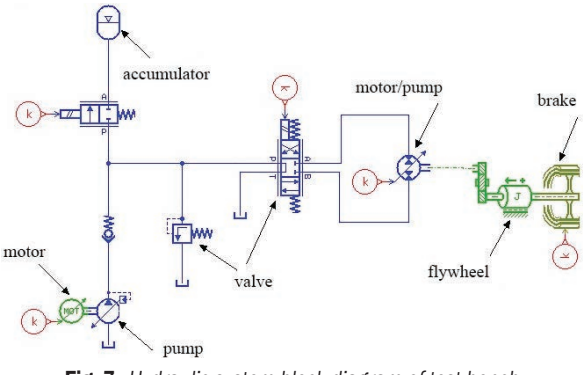

Fig. 7. *Hydraulic system block diagram of test bench*

The test bench is shown in Fig. 8. It was composed of an electric motor (instead of an ICE), a constant pressure variable pump, accumulators, a variable displacement hydraulic motor/pump, magnetic powder brake (to simulate the friction braking), flywheels (the inertia moment of the flywheel simulates inertia moment of a quarter of the vehicle), and the control system. The selected parameters for the test bench were shown in Table 2.

Fig. 8. *Test bench; a) internal connection of test bench; and b) control panel of test bench*

Table 2. *Parameter configuration of test bench*

Parameters	value
Motor rated power, [kW]	75.0
Variable pump displacement, [mL/r]	46.0
Inertial flywheel moment of inertia, [kg·m²]	6.578
Overflow valve setting pressure, [bar]	250.0
Accumulator pre-charge pressure, [bar]	160.0
Gear ratio [-]	1:4
Variable motor/pump displacement, [mL/r]	180.0
Accumulator volume, [L]	63.0

4.2 Breaking Test

The brake strength was z = 0.35, which was the critical braking strength. The system pressure was 180 bar. The test process: accelerate flywheel to 200 rpm (equal to vehicle speed at 18 m/s) and maintain its speed; set the hydraulic motor/pump displacement to 180 mL/r, and keep working in the hydraulic pump state; brake flywheel until the speed was 0 rpm, while energy was transformed into hydraulic energy to charge the accumulator. The obtained test curve is shown in Fig. 9.

The brake strength was z = 0.5, which was in mixed braking mode. The system pressure was 180

bar. Test process: accelerate the flywheel to 200 rpm and maintain the speed stability; set the hydraulic motor/pump displacement to 180 mL/r and work in the hydraulic pump state; According to brake pedal signal, the central controller calculates the friction braking torque 235 N·m; brake flywheel until the speed was 0 rpm, while the energy was converted into the hydraulic energy to charge the accumulator. The test curve is shown in Fig. 10.

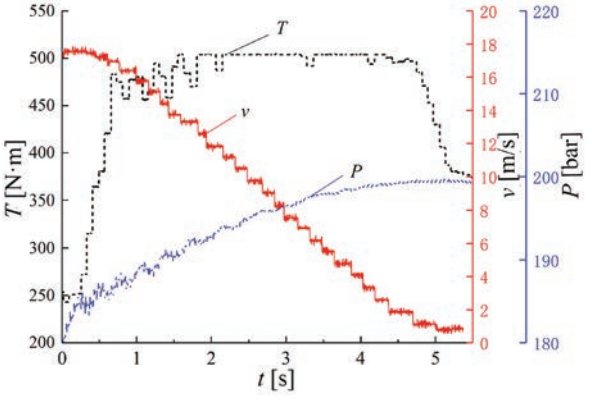

Fig. 9. *Profile of regenerative braking torque, vehicle speed and accumulator pressure*

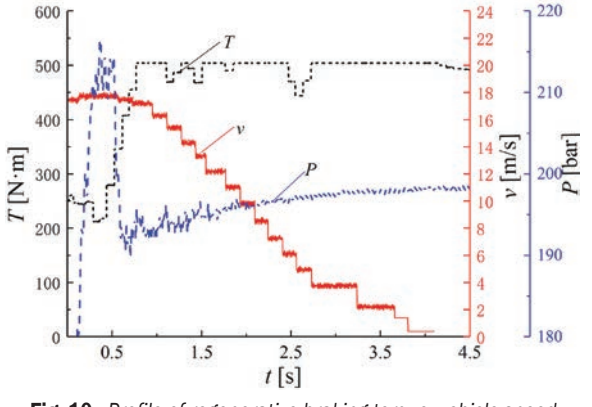

Fig. 10. *Profile of regenerative braking torque, vehicle speed and accumulator pressure*

The test results indicated that the bench could meet the requirement of test and verify the correctness of the control strategy as well.

4.3 Cycle Conditions Test

4.3.1 Drive Cycle

The test was carried out in two cycle conditions (the FUDS cycle and the EUDC-1 cycle), considering the actual operating characteristics of the WDHHV. According to the national standard (GB 14671.1-93) "vehicle test operating conditions" and technical specifications of tactical vehicles, the EUDC-1 cycle was designed from 0 km/h to 130 km/h, including multiple accelerations deceleration stages to simulate the driving characters of the tactical vehicles on the off-road. The speed profile of driving conditions are shown in Figs. 11 and 12, respectively.

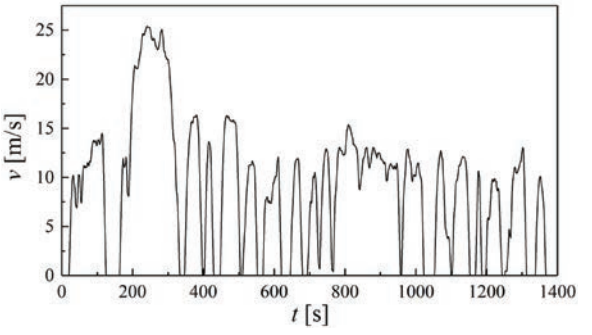

Fig. 11. *FUDS cycle condition*

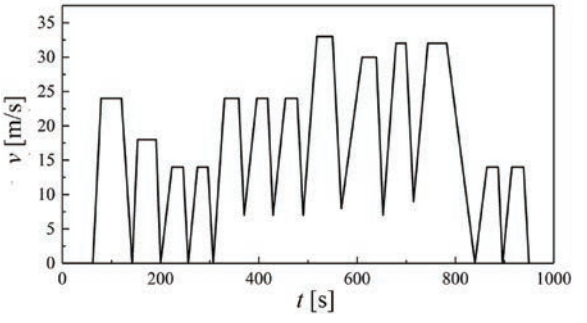

Fig. 12. *EUDC-1 cycle condition*

4.3.2 Calculation of Fuel Economy

The test bench in this study uses a motor instead of an engine. From the perspective of providing energy, using a motor instead of an engine, we obtained the electrical energy consumption of the motor and converted it into corresponding fuel consumption, in which fuel economy can be compared [24]. The simulation procedure of ICE by using an electric motor is shown in Fig. 13.

The motor energy consumption represents the ICE consumption of the whole system. The torque and speed of the motor could be measured by the test bench, which could be used to calculate the motor power, as shown in the Eq. (18).

$$P_m = \frac{T_m \cdot n_m}{9550}, \tag{18}$$

where P_m is the motor power [kW], T_m the motor torque [N·m] and n_m the motor speed [rpm].

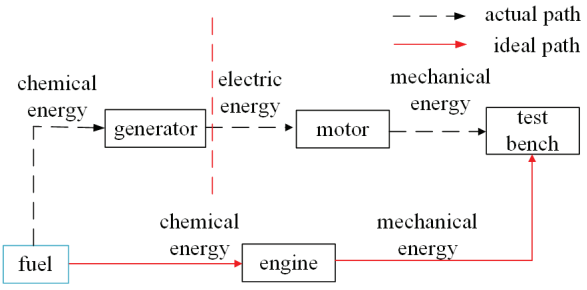

Fig. 13. *The simulation procedure of ICE by using an electric motor*

The power curve of the motor was obtained, and the energy consumption W under the cycle condition could be obtained by the time integral of the power curve. The total fuel consumption could be obtained by origin software in the study. Similarly, making integral for the speed curve can obtain the mileage S of the cycle condition. Therefore, the power consumption of one hundred kilometres M was shown in Eq. (19).

$$M = \frac{W}{S} \times 100. \tag{19}$$

Since the test bench simulated the load of a quarter of vehicle, the power consumption on one-hundred-kilometre M was converted to fuel consumption.

$$F = \frac{M}{m_{\text{oil}} b_{\text{oil}} \eta} \times k, \tag{20}$$

where F is the fuel consumption per hundred kilometres. m_{oil} is the mass of 1 L diesel oil. b_{oil} is the calorific value of 4.6×10^7 J/kg. η is the fuel efficiency of 0.31, and k is 4.0.

4.3.3 Test Results

Under FUDS cycle conditions, the profiles of vehicle speed, electric motor speed, motor torque, motor power and system pressure are shown in Fig. 14.

Fig. 14a represented the speed profile. Compared with Fig. 11, it was clear that there was some error between the speed profiles, but it would not affect the experimental results. Fig. 14b represented the electric motor speed profile. It could be seen that there were three different stages of motor speeds, which was corresponding to three different motor working points and effectively reducing the motor's frequent start-stop in the 0 s to 400 s to reduce energy consumption. Fig. 14d was the motor power profile, and the energy consumption was 1433.28 kJ. Integrating Fig. 14a could attain the entire cycle mileage 6.1 km. Fig. 14e represented the pressure profile of the hybrid system.

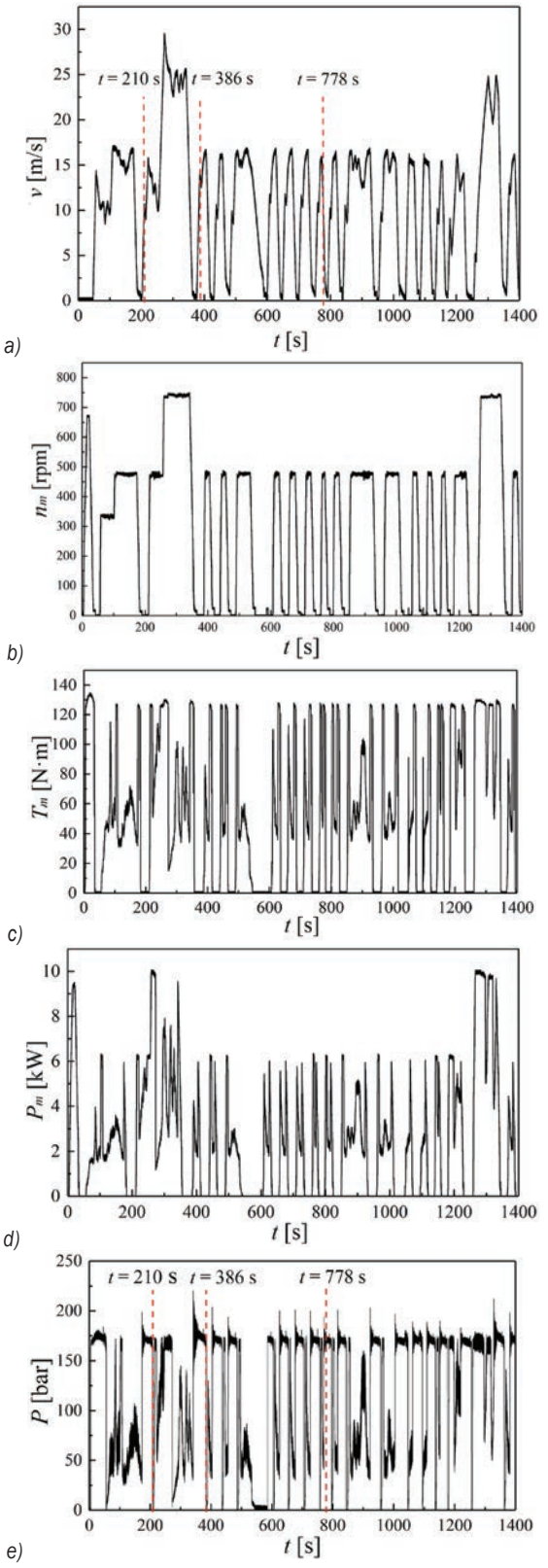

Fig. 14. *Variation of parameters under FUDS cycle; a) vehicle speed profile, b) electric motor speed profile, c) motor torque profile, d) motor power profile, and e) loop pressure profile*

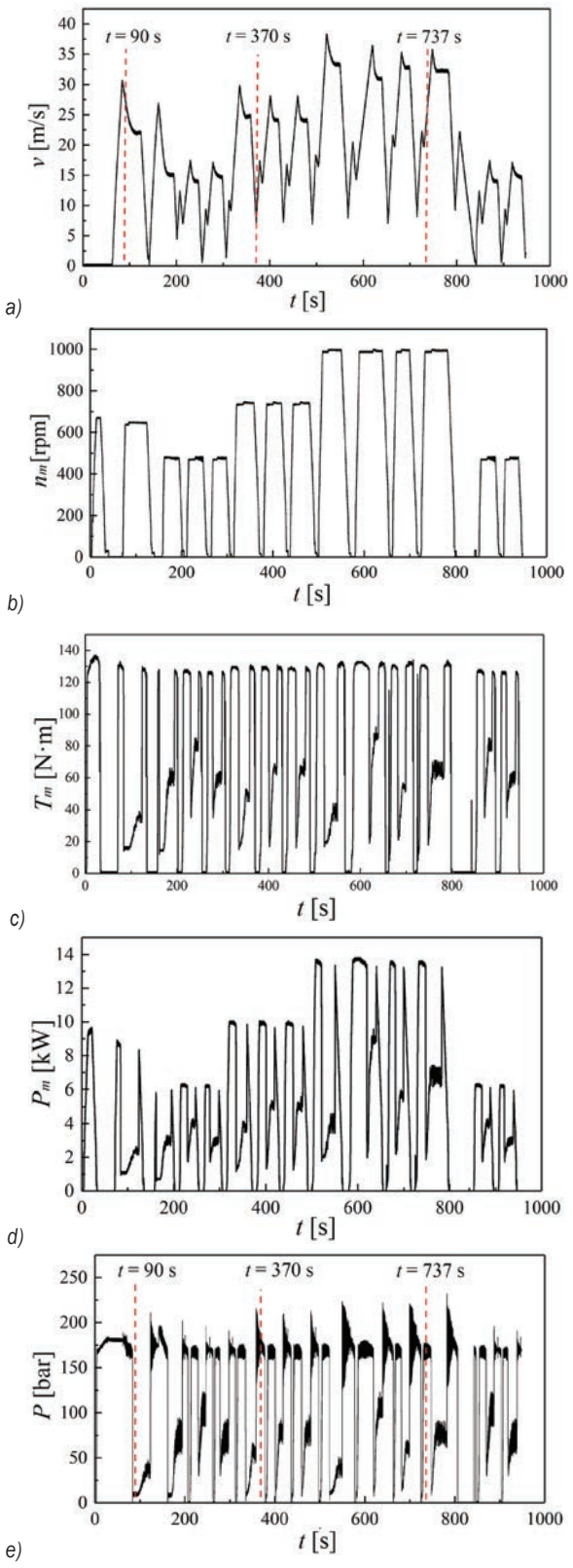

Fig. 15. *Variation of parameters under EUDC-1 cycle; a) vehicle speed profile, b) electric motor speed profile, c) motor torque profile, d) motor power profile, and e) loop pressure profile*

Compared with Fig. 14a, it could be seen that at 210 s, 386 s, 778 s, and other time points, the system pressures and speed change time were basically the same, indicating that the accumulator could realize the recovery and reuse of the vehicle braking energy.

Under the EUDC-1 cycle condition, the change of the vehicle speed, electric motor speed, motor torque, motor power and system pressure are shown in Fig. 15.

Fig. 15a was the vehicle speed profile. Compared with Fig. 12, the speed profile was basically consistent with that of the cycle condition curve. Fig. 15b was the electric motor speed profile. It was obvious that there were four different stages of motor speed, which represented four different motor working points and be greatly reducing the motor frequent start-stop and energy consumption. For Fig. 15d and Fig. 15a, the energy consumed by the integral of the whole cycle was 2003.84 kJ, and the mileage was 8.3 km, respectively. Fig. 15e was the pressure profile of the hybrid system. Compared with Fig. 15a, it could be seen that at 90 s, 370 s, 737 s, and other time points, the system pressures and speed change time were basically the same, and the accumulator could realize the recovery and reuse of vehicle braking energy.

The above test results were brought into Eqs. (18) and (19), respectively, and the improvement of fuel economy us shown in Table 3.

Table 3. *Improvement of fuel economy*

Working condition	test, L/100 km	prototype, L/100 km	Improvement [%]
FUDS	7.80	11	29.09
EUDC-1	8.32		24.36

5 CONCLUSIONS

1) The working principle of the WDHHV was analysed. For driving, a power-following control strategy was designed based on the optimal fuel economy power curve. On the braking hand, the "I" curve distribution strategy based on the critical braking strength z_{min} was adopted. The control strategy was tested under the cycle condition of FUDS and EUDC-1, and finally be compared with fuel consumption of the prototype vehicle.
2) The test results showed that under the two cycle conditions the energy management strategy proposed in this research could meet the vehicle dynamic performance requirements, and the fuel

economy could be increased by more than 24 % compared with the prototype vehicle, which verified the effectiveness of the proposed energy management strategy.

3) On the test bench, the fuel economy of the FUDS cycle condition could be increased by 4.73 % compared with the EUDC-1 cycle, which was due to the frequent start-stop stages of FUDS cycle. Thus, the energy could be fully recovered and reused, and fuel consumption of the engine was effectively reduced.
4) The test bench built in this study had certain errors due to using the motor to simulate the ICE, so further research of the control strategy will be conducted on real vehicles.

6 ACKNOWLEDGEMENTS

This work was supported and funded by a grant from National Natural Science Foundation of China (Grant No. 51505498), a grant from Natural Science Foundation of Jiangsu Province (Grant No. BK20150714), and a grant from National Key R & D Program of China (Grant No. 2016YFC0802900).

7 NOMENCLATURES

B	fuel consumption, [g]
P_e	engine power, [kW]
g_e	fuel consumption rate, [g/(kW·h)]
T_e	engine torque, [N·m]
n_e	engine speed, [rpm]
t	time, [s]
P_{req}	power required of engine, [kW]
$P_{\max}$	maximum power of engine, [kW]
P_{BSFC}	candidate operating points of the ICE, [kW]
$F_{\mu 1}$	front axle braking force, [N]
$F_{\mu 2}$	rear axle braking force, [N]
G	gravity of vehicle, [N]
h_g	height of mass centre, [m]
a, b	distance from mass centre to rear axle and front rear respectively, [m]
L	distance between shafts, [m]
φ	adhesion coefficient on road surface
F_m	brake force of wheels, [N]
T_w	brake torque of wheels, [N·m]
ΔP	pressure drop of variable displacement motor/pump, [Pa]
V	displacement of motor/pump, [m^3/r]
r	radius of wheels, [m]
z	braking strength, [-]
$z_{\min}$	critical braking strength, [-]
$SOC_{\max}$	upper limit of the accumulator SOC, [-]
$SOC_{\min}$	lower limit of the accumulator SOC, [-]
$F_{\mu 1m}$	front axle friction braking force, [N]
$F_{\mu 2m}$	rear axle friction braking force, [N]
$F_{\mu 1p/m}$	front axle regenerative braking force, [N]
$F_{\mu 2p/m}$	rear axle regenerative braking force, [N]
a_1	brake deceleration, [m/s^2]
g	gravity acceleration, [m/s^2]
P_c	current pressure of the air cavity of the accumulator, [bar]
$P_{\max}$	maximum allowable working pressures of the accumulator respectively, [bar]
$P_{\min}$	minimum allowable working pressures of the accumulator respectively, [bar]
T_m	the motor torque, [N·m]
P_m	the motor power, [kW]
n_m	the motor speed, [rpm]
P	the accumulator pressure, [bar]
F	fuel consumption of one hundred kilometres, [L]
W	energy consumption under the cycle condition, [kJ]
M	power consumption on one-hundred-kilometre route, [kJ]
S	mileage of the cycle condition, [km]
m_{oil}	mass of 1L diesel oil, [kg]
b_{oil}	calorific value, 4.6×10^7 J/kg
η	fuel efficiency, 0.31
k	conversion factor between bench and whole vehicle, 4.0

8 REFERENCES

[1] Shabbir, W., Evangelou, S.A. (2019). Threshold-changing control strategy for series hybrid electric vehicles. *Applied Energy*, vol. 235, p. 761-775, **DOI:10.1016/j.apenergy.2018.11.003**.

[2] Chen, J.-S. (2015). Energy efficiency comparison between hydraulic hybrid and hybrid electric vehicles. *Energies*, vol. 8, no. 6, p. 4697-4723, **DOI:10.3390/en8064697**.

[3] Feng, D., Huang, D., Li, D. (2011). Stochastic model predictive energy management for series hydraulic hybrid vehicle. *IEEE International Conference on Mechatronics & Automation*, p. 1980-1986, **DOI:10.1109/ICMA.2011.5986284**.

[4] Pfeffer, A., Glück, T., Kemmetmüller, W., Kugi, A. (2016). Mathematical modelling of a hydraulic accumulator for hydraulic hybrid drives. *Mathematical and Computer Modelling of Dynamical Systems*, vol. 22, no. 5, p. 397-411, **DOI:10.1080/13873954.2016.1174716**.

[5] Song, Q., Zeng, P., He, S., Wang, H. (2014). Power follow control strategy of series electric drive bulldozer based on typical operating conditions. *Journal of Mechanical Engineering*, vol. 50, no. 20, p. 136-142, **DOI:10.39001/JME.2014.20.136**.

[6] Hui, S. (2010). Multi-objective optimization for hydraulic hybrid vehicle based on adaptive simulated annealing genetic algorithm. *Engineering Applications of Artificial*

Intelligence, vol. 23, no. 1, p. 27-33, **DOI:10.1016/jengappai.7.2009.09.005**.

[7] Bravo, R.R.S., De Negri, V.J., Oliveira, A.A.M. (2018). Design and analysis of a parallel hydraulic – pneumatic regenerative braking system for heavy-duty hybrid vehicles. *Applied Energy*, vol. 225, p. 60-77, **DOI:10.1016/j.apenergy.2018.04.102**.

[8] Zhao, L.J., Li, N., Fang, T. (2012). Simulation analysis of control strategy for TLT wheel coordination based on constant pressure network. *Advanced Materials Research*, vol. 591-593, p. 1962-1967, **DOI:10.4028/www.scientific.net/AMR.591-593.1962**.

[9] Bender, F.A., Kaszynski, M., Sawodny, O. (2013). Drive cycle prediction and energy management optimization for hybrid hydraulic vehicles. *IEEE Transactions on Vehicular Technology*, vol. 62, no. 8, p. 3581-3592, **DOI:10.1109/TVT.2013.2259645**.

[10] Song, Y.P., Wang, W.T. (2014). Study on vehicle velocity controller for the energy regeneration system of the hydraulic hybrid vehicle. *Advanced Materials Research*, vol. 1051, p. 850-856, **DOI:10.4028/www.scientific.net/AMR.1051.850**.

[11] Chen, C.K., Vu, T.V., Hung, C.W., Lin, C.J. (2013). Modeling and simulation study of a series hydraulic hybrid vehicle. *Applied Mechanics & Materials*, vol. 284-287, p. 834-838, **DOI:10.4028/www.scientific.net/AMM.284-287.834**.

[12] Chen, C.K., Vu, T.V., Hung, C.W. (2014). A simulation study of power management for a series hydraulic hybrid vehicle. *In: Zelinka, I., Duy, V., Cha, J. (eds.) AETA 2013: Recent Advances in Electrical Engineering and Related Sciences. Lecture Notes in Electrical Engineering, Springer, Berlin, Heidelberg*, vol. 282, p. 413-422, **DOI:10.1007/978-3-642-41968-3_42**.

[13] Chen, Z., Xiong, R., Wang, C., Cao, J. (2017). An on-line predictive energy management strategy for plug-in hybrid electric vehicles to counter the uncertain prediction of the driving cycle. *Applied Energy*, vol. 185, p. 1663-1672, **DOI:10.1016/j.apenergy.2016.01.071**.

[14] Zhou, L., Wang, G., Sun, K., Li, X. (2019). Trajectory tracking study of track vehicles based on model predictive control. *Strojniški vestnik - Journal of Mechanical Engineering*, vol. 65, no. 6, p. 329-342, **DOI:10.5545/sv-jme.2019.5980**.

[15] Ji, C., Zhu, Y., Liang, C, Liu, X. (2013). Simulation study on the operating characteristics of a hybrid hydraulic passenger car with a power split transmission. *Vehicle System Dynamic*s, vol. 51, no. 10, p. 1518-1532, **DOI:10.1080/00423114.2013.812223**.

[16] Prater, G. Jr., Shahhosseini, A.M., Osborne, G.M., Zhang, S. (2010). Simulation studies for determining the response characteristics of a hydraulic hybrid powertrain subframe. *International Journal of Heavy Vehicle Systems*, vol. 17, no. 2, p. 99-118, **DOI:10.1504/IJHVS.2010.033191**.

[17] Baer, K., Ericson, L., Krus, P. (2018). Framework for simulation-based simultaneous system optimization for a series hydraulic hybrid vehicle. *International Journal of Fluid Power*, vol. 7, p. 1-13, **DOI:10.1080/14399776.2018.1527122**.

[18] Xi, P.Y., Chang, S.Q. (2010). Performance simulation and design of new series hydraulic hybrid bus. *Applied Mechanics & Materials*, vol. 37-38, p. 866-869, **DOI:10.4028/www.scientific.net/AMM.37-38.866**.

[19] Li, Q., Chen, W., Li, Y., Liu, S., Huang, J. (2012). Energy management strategy for fuel cell/battery/ultra-capacitor hybrid vehicle based on fuzzy logic. *International Journal of Electrical Power & Energy Systems*, vol. 43, no. 1, p. 514-525, **DOI:10.1016/j.ijepes.2012.06.026**.

[20] Trajkovski, J., Ambrož, M. (2018). The importance of friction coefficient between vehicle tyres and concrete safety barrier to vehicle rollover - FE analysis study. *Strojniški vestnik - Journal of Mechanical Engineering*, vol. 64, no. 12, p. 753-762, **DOI:10.5545/sv-jme.2018.5290**.

[21] Hegedüs, F., Bécsi, T., Aradi, S., Gáspár, P. (2019). Motion planning for highly automated road vehicles with a hybrid approach using nonlinear optimization and artificial neural networks. *Strojniški vestnik - Journal of Mechanical Engineering*, vol. 65, no. 3, p. 148-160, **DOI:/10.5545/sv-jme.2018.5802**.

[22] Naseri, F., Farjah, E., Ghanbari, T. (2017). An efficient regenerative braking system based on battery/supercapacitor for electric, hybrid, and plug-in hybrid electric vehicles with BLDC motor. *IEEE Transactions on Vehicular Technology*, vol. 66, no. 5, p. 3724-3738, **DOI:10.1109/TVT.2016.2611655**.

[23] Held, M., Flärdh, O., Mårtensson, J. (2019). Optimal speed control of a heavy-duty vehicle in urban driving. *IEEE Transactions on Intelligent Transportation Systems*, vol. 20, no. 4 p. 1562-1573, **DOI:10.1109/TITS.2018.2853264**.

[24] Denis, N., Dubois, M.R., Trovão, J.P.F., Desrochers, A. (2018). Power split strategy optimization of a plug-in parallel hybrid electric vehicle. *IEEE Transactions on Vehicular Technology*, vol. 67, no. 1, p. 315-326, **DOI:10.1109/TVT.2017.2756049**.

Strojniški vestnik - Journal of Mechanical Engineering 66(2020)3, 203-212

DOI:10.5545/sv-jme.2019.6461 Original Scientific Paper
Received for review: 2019-11-11
Received revised form: 2020-01-20
Accepted for publication: 2020-02-20

Effect of Gangue Distributions on Cutting Force and Specific Energy in Coal Cutting

Kao Jiang – Kuidong Gao – Lirong Wan*
Shandong University of Science and Technology, College of Mechanical and Electrical Engineering, China

Coal consists of diverse materials, and gangue is one of the most common ones. At present, most mathematical models about cutting force and specific energy in the cutting process have not taken gangue minerals in coal seams into consideration. The gangue distribution function is proposed to simulate situations in which gangue minerals are in different distributions. Moreover, the cutting force due to gangue mineral at different heights is also obtained with the finite element method. Combined with the gangue distribution function, the increased cutting force due to gangue minerals can be obtained for any gangue distribution. The present paper also proposes a new mathematical model to calculate the increased specific energy under different gangue distributions. The results show that the gangue distribution function is useful for simulating various situations of gangue distributions in coal seams. Under dispersive gangue distribution in coal seams, the increased mean cutting force, as well as the increased specific energy, is less influenced by gangue distribution, and it tends to be a constant. These results can be useful for the related research on coal cutting under complicated conditions.
Keywords: cutting force, specific energy, single cutter, gangue distributions

Highlights

- *We proposed the theoretical model for increased specific energy consumption on single cutter, in which gangue minerals in the coal seam and their distributions are firstly taken into consideration.*
- *It has been determined that the increased specific energy is closely related to the amount of gangue minerals in the coal seam and their distributions.*
- *It has been determined that the smaller mean and variance of gangue distributions are able to weaken the influence of traction speeds on the increased mean cutting force and specific energy consumption.*

0 INTRODUCTION

Coal is one of the most important fuels in the world, and it is not a homogeneous material [1]. Gangue minerals usually can be found in coal seams [2]. However, in previous research, the influence of gangue minerals, especially gangue distributions on the cutting performance, are usually ignored [3] and [4]. The differences in material parameters between coal and gangue minerals lead to different mechanical behaviours [5]. For instance, load on cutter usually performs with larger fluctuation when there are some gangue minerals in the coal seam, and this can be attributed to the differences of material parameters, such as hardness between coal and gangue minerals [6] and [7]. Working in this situation over a long time, the cutter tends to be subjected to different degrees of wear and tear [8] and [9]. Therefore, it is essential to study the influence of gangue minerals on cutting performance.

Recently, many approaches have been developed to deal with gangue minerals in coal seams. In earlier research, it was found that cutting load can be reduced when the traction speed decreases [10] and [11]. A method of manual intervention to change the speed is proposed when gangue minerals exist in the cutting process [12]. To reduce the burden on the workers, strategies of self-adaptive control proposed; such strategies will be pre-formulated on traction speed and rotation speed, and then autonomic decision-making will be achieved with the shearer drum according to the cutting conditions. Hu et al. [13] put forward some cutting strategies to deal with different suddenly changing loads. Liu et al. [14] proposed a control system to achieve the goal of self-adaptation. With the particle swarm optimization, the motion parameters can be optimized adaptively according to the variation of cutting resistance.

In addition, coal-rock recognition technology is also popular, and cutting load is no longer the only method to distinguish gangue minerals from coal. Acoustic wave detection technology [15] and image analysis technology [16] are also widely used in coal-rock recognition. Xu et al. [17] proposed a method in which the fuzzy C-means and hybrid optimization algorithm are applied.

Furthermore, other researchers proposed some coal-gangue models, and the positions of gangue minerals in these models satisfy different distributions such as normal distribution and long-tailed distribution [18] and [19]. With the proposed models, the cutting performance can be predicted in advance

*Corr. Author's Address: Shandong University of Science and Technology, Qianwangang Road 579, Qingdao, China, Wansdust@163.com

and some strategies, which are used to improve cutting performance, can be made under different complicated conditions.

Cutting load [20] and [21], specific energy consumption [22] and cutting productivity [23] are the critical parameters for the evaluation of cutting performance. Kurochkin [24] and Dogruoz et al. [25] explored the effect of mechanical properties of different materials on specific energy consumption. Gencay and Erkan [26] found that there is a significant relationship between specific energy and the physical and mechanical properties of rock. Tiryaki and Dikmen [27] found that Poisson's ratio, Brazilian tensile strength, Shore sclera scope hardness, and Schmidt hammer hardness showed very strong linear correlations against specific energy (SE) at confidence levels of 95 %.

At present, although there are many research studies about the specific energy consumption of coal cutting, most do not take gangue minerals and their distributions in coal seam into consideration. Based on this, the paper put forwards the new mathematical model of the increased specific energy, in which gangue minerals in coal seam will be taken into consideration. Then, combined with the number of gangue minerals and their distributions in coal seams, the increased mean cutting force (I_{MCF}) and increased specific energy (I_{SE}) can be obtained under different gangue distributions. Further, it will be useful to make strategies according to the gangue minerals and their distributions in coal seam.

1 METHODS

1.1 Model Simplification of Gangue Minerals in Coal Seams

Gangue minerals in coal seams appear in different shapes. However, the purpose of the present paper is mainly to explore the relationship between gangue distribution and cutting performance. Therefore. the shape of gangue minerals is not covered in this paper. Combined with the research purpose, the following assumptions on gangue minerals in coal need to be made at first:

(I) As the dimensions of gangue minerals are much smaller than that of the coal seam, the gangue in the coal seam will be simplified as a single point, as seen in Fig. 1a;

(II) The gangue minerals, only situated in the same plane, such as Section γ in Fig. 1b, will be considered and the amounts of these gangue

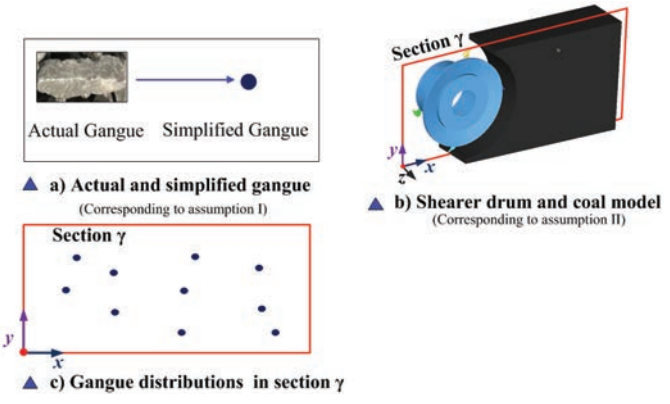

Fig. 1. *Simplified model of gangue minerals in a coal seam*

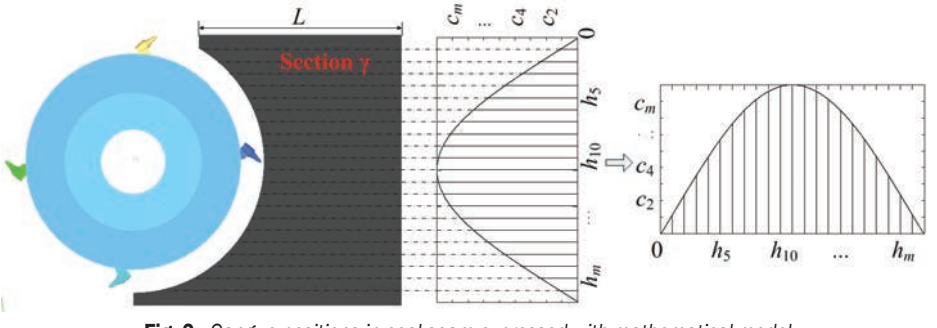

Fig. 2. *Gangue positions in coal seam expressed with mathematical model*

minerals at different heights, as shown in Fig. 1c, will be counted for the description of gangue distribution in the coal seam.

Based on the mentioned assumption, the positions of gangue minerals in the same plane can be marked with $[h_1, h_2, h_3, \ldots, h_i, \ldots, h_m]$, as Fig. 2 shows; the proportion of gangue minerals at the heights can be marked with $[c_1\%, c_2\%, c_3\%,..., c_i\%, \ldots, c_m\%]$; the increased mean cutting force due to single gangue mineral when they are at different heights can be marked with $[F_1, F_2, F_3, \ldots, F_N]$. According to hi and the corresponding F_i, the mathematical relationship between the increased mean cutting force due to single gangue mineral and the height of gangue mineral can be obtained using the fitting method, and the mathematics formula can be expressed in the following:

$$F_i = f_{(h_i)}. \tag{1}$$

According to Eq. (1), the increased mean cutting force due to single gangue mineral can be obtained when gangue minerals are at different heights and then the increased mean cutting force due to all gangue minerals in coal seam (namely I_{MCF}) can be expressed by Eq. (2) .

$$I_{MCF} = N \cdot \sum_{i=1}^{m} (c_i \cdot F_i), \tag{2}$$

where N is the total number of gangue minerals in coal seam at different heights.

1.2 Expression of Gangue Distributions with Mathematical Method

It is mentioned that the cutting force on the cutter due to gangue mineral can be obtained according to its position. Therefore, the I_{MCF} is calculable when the positions of all gangue minerals in the same plane are identified. However, to date, there is no reference on how to locate gangue minerals in a coal seam. Therefore, gangue distribution trends, instead of the precise positions, are used in the paper.

The normal distribution, which proves to be common distribution in nature and has become an important forecasting model in mathematics, physics and engineering areas, is employed for simulating gangue distribution; it is called "the gangue distribution" function in this paper and is shown in Eq. (3). By adjustment of the mean and variance of the gangue distribution function, the potential distributions of gangue minerals in a coal seam might be approximately simulated.

$$f(h_i) = \frac{1}{\sqrt{2\pi}\sigma} \exp^{\left(-\frac{(h_i-\mu)^2}{2\sigma^2}\right)}, \tag{3}$$

where μ is the mean in the normal distribution. In this paper, it is the mean height of gangue distribution in a coal seam; σ is the variance in a normal distribution. In this paper, it is the height variance of gangue distribution in a coal seam.

With the gangue distribution function, potential gangue distributions in coal seam can be simulated by adjustment to the mean and variance of the gangue distribution function. In this paper, the following gangue distributions on the influence of cutting performance will be studied: a) gangue minerals in concentrative distributions (σ=0.05 m); b) gangues in dispersive distributions (σ=0.90 m); c) most gangue minerals at the top of coal seam with different dispersions (μ=0.15 m); d) most gangue minerals at the middle of coal seam with different dispersions (μ=0.90 m).

1.3 Mathematical Model for Specific Energy Consumption

According to the previous conclusions, the formula for the specific energy consumption is as follows:

$$H_{WC} = 2.78 \times 10^{-4} W / V. \tag{4}$$

In the formula, H_{WC} is the specific energy consumption of the cutter in the cutting process [kW·h/m^3]; W is the mechanical energy of the cutter in the cutting process [kN·m]; V is the volume of coal crushed by the cutter in the cutting process, [m^3].

After simple calculation, the specific energy consumption in coal-cutting process without any gangue minerals H_{WC} and specific energy consumption in gangue-cutting process I_{SE} can be expressed in Eqs. (5) and (6).

$$H_{WC} = 2.78 \times 10^{-4} \frac{F_{C,ave} \cdot t_c}{H \cdot L}, \tag{5}$$

$$I_{SE} = 2.78 \times 10^{-4} \frac{N \cdot \sum_{i=1}^{m} (c_i \cdot F_i) \cdot t_R}{H \cdot L}. \tag{6}$$

2 RESULTS

2.1 Relations between Cutting Force and Gangue Positions

Gangue minerals in a coal seam usually lead to much larger cutting force on conical picks; in this paper, the cutting force increased due to single gangue F_i is

studied when gangue minerals are at different heights. For research, the rotary cutting model with a coal seam [4] is established with the finite element method. In the simulation, material similar to gangue minerals is added at different heights in the coal seam. Four kinds of gangue positions (0 m, 0.3 m, 0.6 m, and 0.9 m are selected. in the simulation, the traction speed of cutter is 0.06 m/s, 0.08 m/s, and 0.10 m/s. The diameter of the shearer drum is 2.2 m and the rotational speed is 3 rad/s. Fig. 3 shows the cutting force due to a single gangue mineral under different traction speeds and gangue positions. The increase of mean cutting force F_i due to a single gangue mineral is shown in Table 1, according to the results in Fig. 3.

From Table 1, the F_i increases with the traction speed, and it also increases when gangue minerals are closer to the middle of the coal seam. This is because, in these situations, the thickness of gangue chips separated from coal seam is larger, and there is a positive correlation between the cutting force and the thickness of separated chips. Therefore, high traction speed should be avoided, especially in the situations in which gangue minerals are closer to the middle of the coal seam.

Some gangue positions have been simulated with the finite element model and the corresponding cutting force due to gangue minerals can be obtained. However, with the limited groups of simulation, it is impossible to obtain the corresponding F_i when gangue minerals are at any positions. Therefore, with the results in Table 1, the mathematical model that reveals the relations between the F_i and h_i, is established with the data-fitting method. The fitting results are shown in Fig. 4. A power law relation between the F_i and h_i is shown, and the determination coefficients (the square of the correlation coefficient, referred to as [R^2]) in the mathematical model are all beyond 0.98. Eqs. (7) to (9) show the mathematical model between the F_i and the h_i under traction speeds of 0.06 m/s, 0.08 m/s and 0.10 m/s.

$$F_i = 47.69h_i^{0.4196}, \quad R^2 = 0.9903, \tag{7}$$

$$F_i = 55.37h_i^{0.4172}, \quad R^2 = 0.9946, \tag{8}$$

$$F_i = 62.51h_i^{0.4163}, \quad R^2 = 0.9895. \tag{9}$$

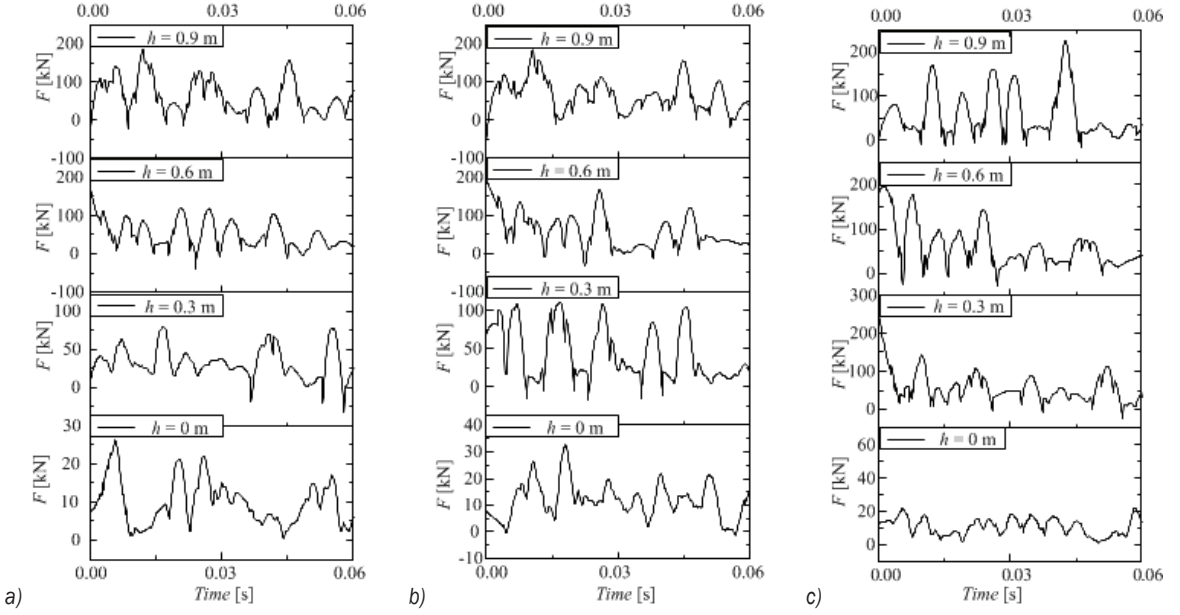

Fig. 3. *The increased cutting force due to single gangue mineral at different heights under different traction speeds; a) v = 0.06 m/s; and b) v = 0.08 m/s; and c) v = 0.10 m/s*

Table 1. *The increased mean cutting force due to single gangue mineral at different heights under different traction speeds*

v [m/s]	h_i [m]	F_i [kN]	v [m/s]	h_i [m]	F_i [kN]	v [m/s]	h_i [m]	F_i [kN]
0.06	0	9.52	0.08	0	10.84	0.10	0	11.85
	0.3	29.11		0.3	32.75		0.3	37.87
	0.6	37.82		0.6	45.33		0.6	45.88
	0.9	45.99		0.9	52.68		0.9	57.79

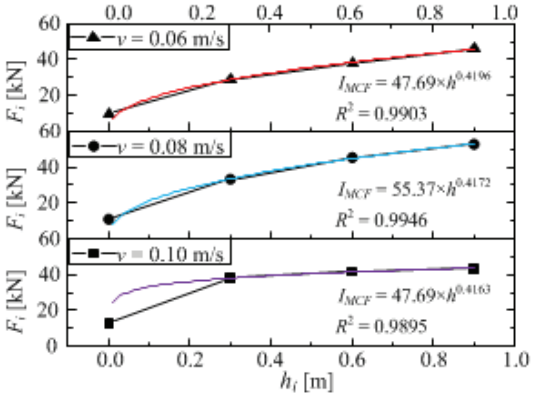

Fig. 4. *Relationship between the F_i and h_i under different traction speeds*

2.2 Relations between the increased mean cutting force and gangue distributions

2.2.1 *Effect of μ on I_{MCF}*

According to Eq. (2), the I_{MCF} is the sum of F_i, and it is not only related to gangue positions but also the total number of gangue minerals in the coal seam and gangue distributions. From Eq. (2), it is obvious that there is a non-linear relationship between the I_{MCF} and gangue distributions. Therefore, the study on the I_{MCF} under different gangue distributions is essential.

As mentioned, with the gangue distribution function, the simulation of the gangue potential distributions in a coal seam can made be possible by adjustments to the mean and variance of gangue distributions in the coal seam. Figs .5 and 6 show concentrative gangue distributions (σ=0.05 m) and dispersive gangue distributions (σ=0.90 m), and the corresponding I_{MCF}.

Fig. 5a shows the proportion of gangue minerals at different heights. Fig. 5b shows the I_{MCF} under the concentrative gangue distributions shown in Fig. 5a. When gangue minerals are in concentrative distributions, the I_{MCF} is influenced by the mean of gangue distributions. Because concentrative distribution means that most of the gangue minerals are at or around a certain position, which can be seen in Fig. 5a, and the F_i differs greatly when gangue minerals are at different positions. Therefore, when

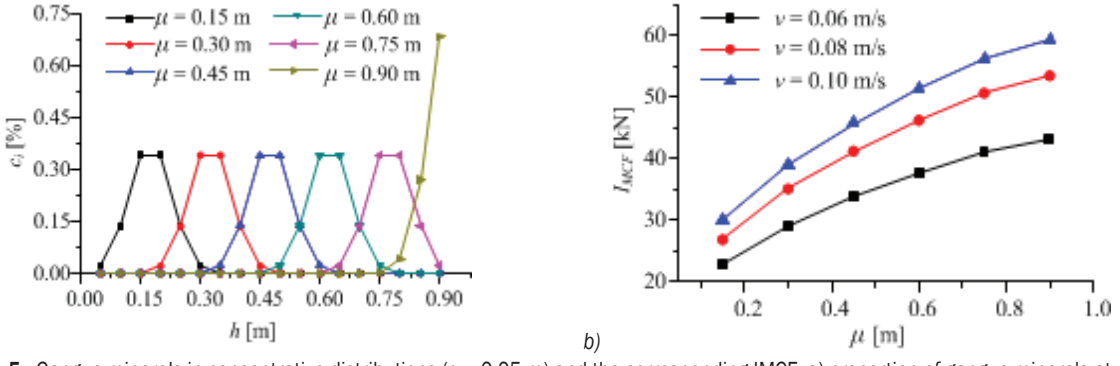

a) b)

Fig. 5. Gangue minerals in concentrative distributions (σ = 0.05 m) and the corresponding IMCF; a) proportion of gangue minerals at different heights; and b) the IMCF varied with the mean of gangue distributions

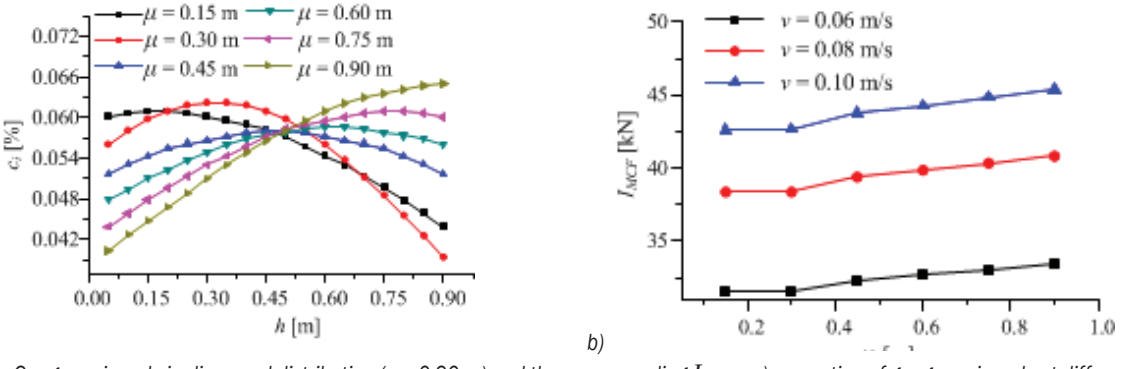

a) b)

Fig. 6. *Gangue minerals in dispersed distribution (σ = 0.90 m) and the corresponding I_{MCF}; a) proportion of gangue minerals at different heights; and b) the I_{MCF} varied with the mean of gangue distributions*

the mean of gangue distribution varies, the I_{MCF} also differs greatly.

When gangue minerals in a coal seam are dispersed as shown in Fig. 6a, the I_{MCF} is slightly influenced by the mean of gangue distributions, as Fig. 6b shows, because the larger dispersion means the number of gangue minerals at different heights is closer to each other. In this case, there is little difference in the number of gangue minerals at the same positions even if gangue minerals are in different distributions. Therefore, under dispersive distributions, it is pointless to study the influence of gangue positions on I_{MCF} and, in this case, the I_{MCF} will approach a certain result, which is only related with the traction speed of cutter and the total number of gangue minerals in the coal seam.

2.2.2 Effect of σ on I_{MCF}

The variance of gangue distributions is another variable reflecting the characteristics of gangue distributions in a coal seam. Fig. 7 shows the I_{MCF} under different variances when the mean of gangue distributions is smaller (μ=0.15 m). Fig. 8 shows the I_{MCF} under different variances when the mean of gangue distributions is larger (μ=0.90 m).

Fig. 7a shows the proportion of gangue minerals at different heights when relatively numerous gangue minerals are at the top of coal seam with different variances. Fig. 7b shows the I_{MCF} under the gangue distributions shown in Fig. 7a. From Fig. 7b, the I_{MCF} stops increasing until the variance of gangue distribution is beyond 0.6 m when the relatively numerous gangue minerals are at the top of the coal seam. The reasons can be found in Fig. 7a, in which there is little difference between the proportions of gangue minerals at different heights under different variances when the variance is beyond 0.6 m. Therefore, the I_{MCF} is close to each other in this condition.

Fig. 8a shows the proportion of gangue minerals at different heights when relatively numerous gangue minerals are at the middle of the coal seam with different variances. Fig. 8b shows the I_{MCF} under the gangue distributions shown in Fig. 8a. From Fig. 8b, I_{MCF} almost stops decreasing and remains constant after the variance is beyond 0.3 m, because, as shown in Fig. 8a, the relatively numerous gangue minerals

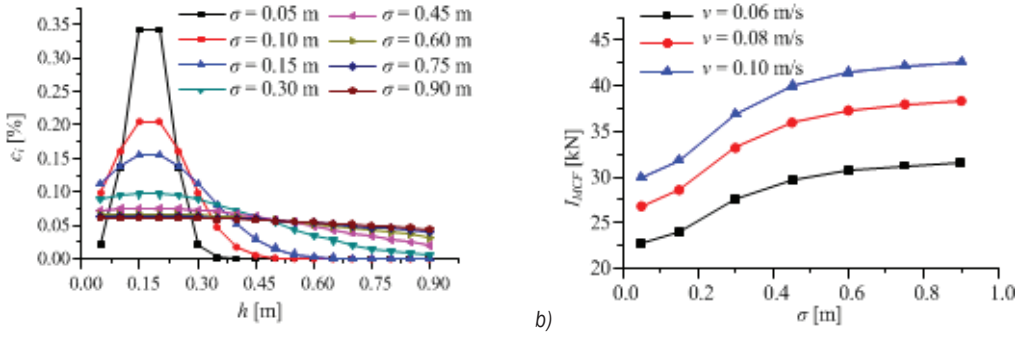

Fig. 7. *Gangue distributions with different variances under smaller mean (μ = 0.15 m) and the corresponding I_{MCF}; a) proportion of gangue minerals at different heights under different distributions; and b) the I_{MCF} varied with the variance of gangue distributions*

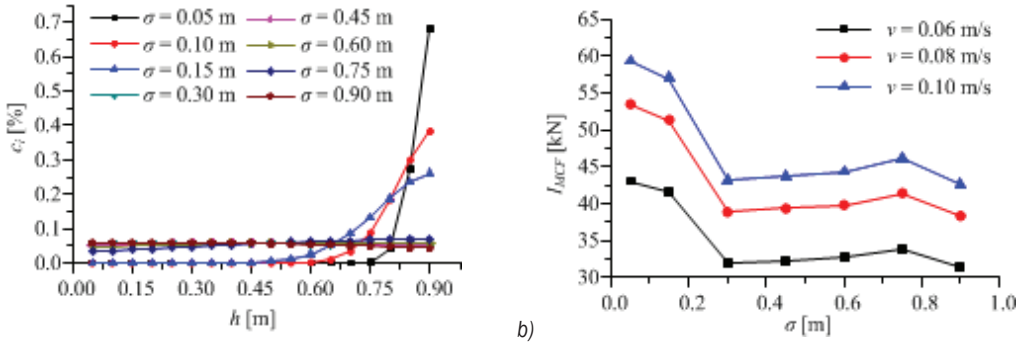

Fig. 8. *Gangue distributions with different variances under larger mean (μ = 0.90m) and the corresponding I_{MCF}; a) proportion of gangue minerals at different heights under different distributions; and b) the I_{MCF} varied with the variance of gangue distributions*

are at the middle of the coal seam when the variance is beyond 0.3 m. As mentioned the closer the gangue minerals are to the middle of coal seam, the larger the cutting force is. Therefore, the I_{MCF} is larger when the variance is beyond 0.3 m.

2.3 Relations between the Increased Specific Energy and Gangue Distributions

The increased specific energy consumption (referred to as I_{SE}) due to gangue cutting is also obtained in this paper. To study the I_{SE} under different gangue distributions, I_{SE}/H_{WC} is introduced, as shown in Eq. (10). H_{WC} is the specific energy consumption when there are not any gangue minerals in the coal seam.

$$\frac{I_{SE}}{W_{WC}} = \frac{N \cdot \sum_{i=1}^{n} (c_i \cdot F_i) \cdot t_R . v}{F_{C,ave} \cdot L}. \tag{10}$$

According to Eq. (10), I_{SE}/H_{WC} is the variable associated with many factors such as gangue distributions, the number of gangue minerals in the coal seam, traction speed of cutters, and the length of coal, which contains gangue minerals. For the convenience of research, further derivation is made on Eq. (10) and then Eq. (11) is obtained, as follows:

$$\frac{I_{SE}}{W_{WC}} = \frac{N \cdot t_R}{L} \cdot \frac{\sum_{i=1}^{n} (c_i \cdot F_i) \cdot v}{F_{C,ave}}. \tag{11}$$

According to Eq. (11), the I_{SE}/H_{WC} is divided into two main parts. One is related to the number of gangue minerals in a coal seam, the length of coal where gangue minerals distribute, and the average time of gangue cutting. There is a linear relation between I_{SE}/H_{WC} and $N{\cdot}t_R/L$. The other is related to gangue distribution, the traction speed of cutters, and the mean cutting force under coal cutting condition.

Fig. 9 shows I_{SE}/H_{WC} under different gangue distributions. Fig. 9a shows I_{SE}/H_{WC} when gangue minerals are as concentrated as shown in Fig. 5a. According to the figure, the I_{SE}/H_{WC} varies greatly with the mean of gangue distribution. The difference on the I_{SE}/H_{WC} under different mean of gangue

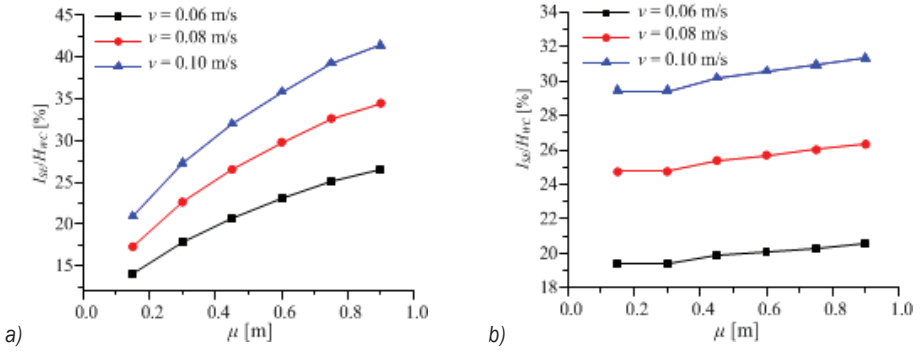

Fig. 9. *Relationship between I_{SE}/H_{WC} and gangue distributions; a) I_{SE}/H_{WC} varied with the mean of gangue distributions under concentrative gangue distributions (σ = 0.05 m); and b) I_{SE}/H_{WC} varied with the mean of gangue distributions under dispersed gangue distributions (σ = 0.90 m)*

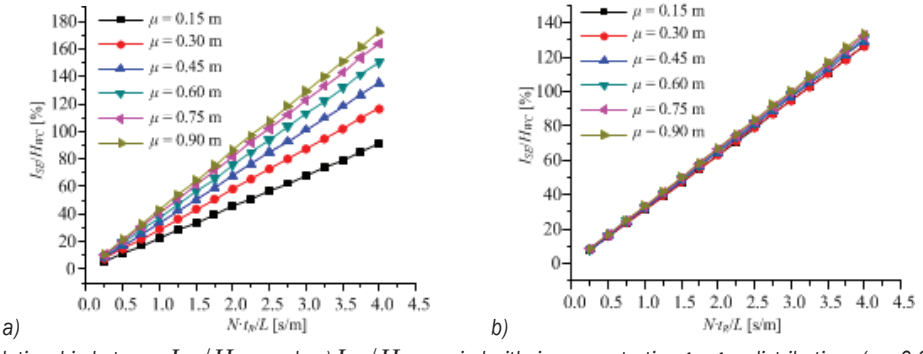

Fig. 10. *Relationship between I_{SE}/H_{WC} and ; a) I_{SE}/H_{WC} varied with in concentrative gangue distributions (σ = 0.05 m); and b) I_{SE}/H_{WC} varied with under dispersed gangue distributions (σ = 0.90 m)*

distributions is about 15 % to 20 %. Fig. 9b shows I_{SE}/H_{WC} when gangue minerals are in dispersive distributions, as shown in Fig. 6a. According to Fig. 9b, the I_{SE}/H_{WC} rarely varies with the mean of gangue distribution. The difference in the I_{SE}/H_{WC} under different means of gangue distributions is no more than 5 %. Therefore, when gangue minerals are dispersive, the results on the $\mathrm{I}I_{SE}/H_{WC}$ are close to each other wherever the most gangue minerals are in the coal seam.

According to Eq. (11), I_{SE}/H_{WC} is not only related with gangue distributions, but also the formula $N{\cdot}t_R/L$. Fig. 10 shows I_{SE}/H_{WC} varied with $N{\cdot}t_R/L$ under different gangue distributions. When gangue distributions are concentrated in a coal seam, the I_{SE}/H_{WC} under different $N{\cdot}t_R/L$ is shown in Fig. 10a. From Fig. 10a, it is evident that the I_{SE}/H_{WC} increases with the $N{\cdot}t_R/L$. When the relatively numerous gangue minerals are closer to the middle of coal seam, the I_{SE}/H_{WC} varies greatly with $N{\cdot}t_R/L$. Therefore, the length of coal seam and the total number of gangue minerals should be considered, especially when most gangue minerals are closer to the middle of coal seam.

When gangue minerals are dispersed in a coal seam, the I_{SE}/H_{WC} under different $N{\cdot}t_R/L$ is shown in Fig. 10b. Unlike the situations in Fig. 10a, there are few differences among the I_{SE}/H_{WC} under different gangue distribution even if most gangue minerals are at the top of the coal seam. Therefore, in dispersive gangue distribution, the I_{SE}/H_{WC} is determinable according to the formula $N{\cdot}t_R/L$ without considering the gangue distribution. Moreover, from the figure, I_{SE}/H_{WC} reaches more than 100 % as soon as the $N{\cdot}t_R/L$ is over 4 s/m. In other words, when the $N{\cdot}t_R/L$ is over 4 s/m, the I_{SE}/H_{WC} due to gangue cutting increases by 100 % compared with that due to coal cutting without any gangue minerals.

3 CONCLUSIONS

(1) Gangue distribution function in the paper is used to simulate potential gangue distributions in a coal seam. It can be achieved and simulated by adjustments to the mean and variance of the gangue distribution function in coal seam. The results show that gangue distribution function is suitable for simulation of the situations that gangue minerals at different heights are in different proportions.

(2) The increased mean cutting force due to gangue minerals I_{MCF} is closely related to the positions of the gangue minerals. The relationship between the increased mean cutting force and the positions at which they are can be obtained with the assistance of the finite element method. The results show that there is a strong correlation between the mentioned factors and that the correlation coefficient is more than 0.98. This might be helpful to obtain the positions of gangue minerals in the coal seam according to the cutting force.

(3) The increased mean cutting force I_{MCF} due to gangue minerals is closely related to gangue distribution. With the increase of gangue dispersion in the coal seam, the increased mean cutting load I_{MCF} tends to be a constant and not greatly influenced by gangue distribution. Therefore, when gangue minerals are dispersed in a coal seam, the increased mean cutting load I_{MCF} is calculable.

(4) The increased specific energy due to gangue minerals in a coal seam is also obtained under different gangue distributions, and it is a variable that is nonlinear with gangue distribution and linear with the length of coal seam and the number of gangue minerals in a coal seam. When gangue minerals in a coal seam are dispersed, and the $N{\cdot}t_R/L$ is larger than 4 s/m, the increased specific energy increases by 100 % compared with that due to coal cutting without any gangue minerals.

4 ACKNOWLEDGEMENTS

This work was supported by the Key Research and Development Project of China (Grant No.2017YFC0603000), the Innovative Team Development Project of Ministry of Education (Grant No. IRT_16R45), the National Natural Science Foundation of China (Grant No. 51704178), Natural Science Foundation of Shandong Province (Grant No. ZR2019MEE067), Natural Science Foundation of Shandong Province (Grant No. ZR2017MEE034), Natural Science Foundation of Shandong Province (Grant No. ZR2019BEE066), Science and Technology Innovation Project in Shandong University of Science and Technology (Grant No. SDKDYC190326).

5 NOMENCLATURES

I_{MCF}	the increased mean cutting force due to all gangue minerals, [kN]
I_{SE}	the increased specific energy due to all gangue minerals, [kW·h/m^3]
L	length of coal seam with gangue minerals, [m]

H height of coal seam with gangue minerals, [m]
μ the mean height of gangue distribution in a coal seam, [m]
σ the height variance of gangue distribution in a coal seam, [m]
h_i positions of gangue minerals in a coal seam, [m]
F_i the increased mean cutting force due to single gangue mineral, [kN]
N the total number of gangue minerals at the different heights, [-]
W the mechanical energy of a single cutter, [kN·m]
V the volume of coal crushed by a single cutter, [m^3]
v the linear velocity of a cutter, [m/s]
c_i the proportion of gangue minerals at different heights, [%]
$F_{C,ave}$ the mean cutting force on cutter due to coal, [kN]
t_C the total time taken in the coal-cutting process, [s]
t_R the average time taken in the gangue-cutting process, [s]
H_{WC} the specific energy consumption in the coal-cutting process, [kW·h/m^3]

6 REFERENCES

[1] Bakhtavar, E., Shahriar, K. (2013). Selection of a practicable shearer loader based on mechanical properties of coal for parvadeh mine. *Archives of Mining Sciences*, vol. 58, no. 1, p. 145-157, **DOI:10.2478/amsc-2013-0010**.

[2] Su, X.P. (2013). *Study on Key Technologies of Auto-Height Adjustment for Shearer*. PhD thesis, China University of Mining and Technology, XuZhou.

[3] Khair, A.W. (1996). The effect of bit geometry on rock cutting efficiency. *Applied Occupational & Environmental Hygiene*, vol. 11, no. 7, p. 695-700, **DOI:10.1080/1047322X.1996.10389959**.

[4] Wan, L.R., Jiang, K., Gao, K.D., Zeng, Q.L. (2018). Research of response difference on coal cutting load under different cutting parameters. *Strojniški vestnik - Journal of Mechanical Engineering*, vol. 65, no. 7-8, p. 420-429, **DOI:10.5545/sv-jme.2018.5940**.

[5] Yang, D.L., Li, J.P., Du, C.L., Zheng, K.H. Liu, S.Y. (2017). Particle size distribution of coal and gangue after impact-crush separation. *Journal of Central South University*, vol. 24, no. 6, p. 1252-1262, **DOI:10.1007/s11771-017-3529-2**.

[6] Bilgin, N., Demircin, M.A., Copur, H. Balcia, C., Tuncdemira H., Akcinc, N. (2006). Dominant rock properties affecting the performance of conical picks and the comparison of some experimental and theoretical results. *International Journal of Rock Mechanics and Mining Sciences*, vol. 43, no. 1, p. 139-156, **DOI:10.1016/j.ijrmms. 2005.04.009**.

[7] Poulsen, B.A., Adhikary, D.P. (2013). A numerical study of the scale effect in coal strength. *International Journal of Rock Mechanics and Mining Sciences*, vol. 63, p. 62-71, **DOI:10.1016/j.ijrmms.2013.06.006**.

[8] Dewangan, S., Chattopadhyaya, S., Hloch, S. (2015). Wear assessment of conical pick used in coal cutting operation. *Rock Mechanics and Rock Engineering*, vol. 48, no. 5, p. 2129-2139, **DOI:10.1007/s00603-014-0680-z**.

[9] Yang, D.L., Li, J.P., Wang, L.P., Gao, K., Tang, Y., Wang., Y. (2015). Experimental and theoretical design for decreasing wear in conical picks in rotation-drilling cutting process. *International Journal of Advanced Manufacturing Technology*, vol. 77, no. 9-12, p. 1571-1579, **DOI:10.1007/s00170-014-6472-5**.

[10] Liu, S.Y., Du, C.L., Cui, X.X. (2009). Research on the cutting force of a pick. *Mining Science and Technology (China)*, vol. 19, no. 4, p. 514-517, **DOI:10.1016/s1674-5264(09)60096-x**.

[11] Dahlman, P., Gunnberg, F., Jacobson, M. (2004). The influence of rake angle, cutting feed and cutting depth on residual stresses in hard turning. *Journal of Materials Processing Technology*, vol. 147, no. 2, p. 181-184, **DOI:10.1016/j.jmatprotec.2003.12.014**.

[12] Xu, J., Wang, Z.B., Tan, C., SI, L., Liu, X. (2015). A cutting pattern recognition method for shearers based on improved ensemble empirical mode decomposition and a probabilistic neural network. *Sensors*, vol. 15, no. 11, p. 27721-27737, **DOI:10.3390/s151127721**.

[13] Hu, J.J., Zha, J.L., Liu, C.Z., Sun, C.J. (2018). Research on drum shearer speed control strategies under sudden-changing load. *Journal of the Brazilian Society of Mechanical Sciences and Engineering*, vol. 40, no. 6, p. 323-333, **DOI:10.1007/s40430-018-1252-z**.

[14] Liu, Y., Hou, L., Qin, D.T., Zhang, Y. (2017). Self-adaptive control of shearer based on cutting resistance recognition. *The International Journal of Advanced Manufacturing Technology*, vol. 94, no. 9-12, p. 3553-3561, **DOI:10.1007/s00170-017-1199-8**.

[15] Purcell, D.D., Ben-Bassat, M. (1976). *Development of Signal Processing Algorithms for Ultrasonic Detection of Coal Seam Interfaces*. Perceptronics, Woodland Hills.

[16] Ralston, J.C., Strange, A.D. (2013). Developing selective mining capability for longwall shearers using thermal infrared-based seam tracking. *International Journal of Mining Science and Technology*, vol. 23, no. 1, p. 47–53, **DOI:10.1016/j.ijmst.2013.01.008**.

[17] Xu, J., Wang, Z.B., Wang, J.B. Tan, C., Zhang, L., Liu, X.H. (2016). Acoustic-based cutting pattern recognition for shearer through fuzzy c-means and a hybrid optimization algorithm. *Applied Sciences*, vol. 6, no. 10, **DOI:10.3390/app6100294**.

[18] Wang, H.J., Zhang, Q. (2019). Dynamic identification of coal-rock interface based on adaptive weight optimization and multi-sensor information fusion. *Information Fusion*, vol. 51, p. 114-128, **DOI:10.1016/j.inffus.2018.09.007**.

[19] Li, X.H., Yu, X.W. (2009). Simulation and study of hard parcel distribution on continuous miner coalface. *World Sci-Tech*

R&D, vol. 31, no. 33, p. 423-424, **DOI:10.16507/j.issn.1006-6055.2009.03.012**.

[20] Polini, W., Turchetta, S. (2004). Force and specific energy in stone cutting by diamond mill. *International Journal of Machine Tools & Manufacture*, vol. 44, no. 11, p. 1189-1196, **DOI:10.1016/j.ijmachtools.2004.04.001**.

[21] Zhang, M., Zheng, M., Jiang, B. (2018). Judging method of tooth damage behavior of the high speed milling cutter. *Strojniški vestnik - Journal of Mechanical Engineering*, vol. 64, no. 2, p. 130-143, **DOI:10.5545/sv-jme.2017.5061**.

[22] Atici, U., Ersoy, A. (2009). Correlation of specific energy of cutting saws and drilling bits with rock brittleness and destruction energy. *Journal of Materials Processing Technology*, vol. 209, no. 5, p. 2602-2612, **DOI:10.1016/j.jmatprotec.2008.06.004**.

[23] Anani, A., Nyaaba, W., Hekmat, A., Córdova, E.A. (2018). Optimizing cut-out distance for maximum coal productivity. *Simulation: Transactions of the Society for Modeling and Simulation*, vol. 95, no. 6, p. 545-559, **DOI:10.1177/0037549718811588**.

[24] Kurochkin, N.V. (1965). Effects of mechanical properties on the cutting rate and specific energy consumption in ultrasonic machining. Soviet Physics Doklady, vol. 9, p. 599.

[25] Dogruoz, C., Rostami, J., Keles, S. (2017). Study of correlation between specific energy of cutting and physical properties of rock and prediction of excavation rate for lignite mines in Çayırhan area, Turkey. *Bulletin of Engineering Geology and the Environment*, vol. 2017, no. 3, p. 1-7, **DOI:10.1007/s10064-017-1124-2**.

[26] Gencay, S., Erkan, Ö. (2018). Effects of natural rock properties on cutting forces, specific energy and specific cutting energy by four-axis machine. *Arabian Journal of Geosciences*, vol. 11, no. 5, p. 84, **DOI:10.1007/s12517-018-3424-7**.

[27] Tiryaki, B., Dikmen, A.C. (2006). Effects of rock properties on specific cutting energy in linear cutting of sandstones by picks. *Rock Mechanics and Rock Engineering*, vol. 39, no. 2, p. 89-120, **DOI:10.1007/s00603-005-0062-7**.

Vsebina

Strojniški vestnik - Journal of Mechanical Engineering
letnik 66, (2020), številka 3
Ljubljana, marec 2020
ISSN 0039-2480

Izhaja mesečno

Razširjeni povzetki

Osebne objave

Strojniški vestnik - Journal of Mechanical Engineering 66(2020)3, SI 19,

Prejeto v recenzijo: 2019-10-30
Prejeto popravljeno: 2020-01-07
Odobreno za objavo: 2020-01-22

Krmilni sistem naprave za natezne preizkuse z uporabo cenovno ugodne strojne opreme in odprtokodnega programja

Matej Kranjec* – Jernej Korinšek – Miha Ambrož – Robert Kunc
Univerza v Ljubljani, Fakulteta za strojništvo, Slovenija

Vsakodnevni izziv raziskovalcev je izvajanje eksperimentov z omejenimi sredstvi, zato stremimo k temu, da uporabljamo čimbolj cenovno ugodno opremo, ki je vseeno dovolj zanesljiva, da zagotavlja dovolj natančne in hitre meritve, kot jih zahtevajo protokoli. S predstavljeno raziskavo smo želeli preveriti, ali je možno razviti in izdelati cenovno ugoden sistem za zajemanje podatkov in krmiljenje kompleksnega sistema že obstoječe naprave za natezne preizkuse. Za nadgradnjo krmilnega sistema smo se odločili zaradi starosti in nepravilnega delovanja obstoječe krmilne opreme in opreme za zajemanje podatkov. Kot cenovno ugodno nadomestilo dragim komercialnim krmilnikom smo uporabili kartični računalnik Raspberry Pi 3B+. Na podlagi predhodnega nezanesljivega krmilnega sistema smo postavili seznam minimalnih zahtev, da bi zagotovili enako raven merilne natančnosti za dostopno ceno. Predlagana nadgradnja mora natančno krmiliti koračni motor ter zajemati podatke iz linearnega magnetnega enkoderja in natezne merilne celice.

Za povezavo vse potrebne opreme smo razvili povezovalno ploščo, dokupili pa smo tudi dodatno strojno opremo za zagotavljanje pravilnega delovanja celotnega krmilnega sistema. Za prenosnost krmilnega sistema smo poskrbeli tako, da smo vse njegove komponente postavili v ohišje s priključki za opremo naprave za natezne preizkuse. Programski del krmilne naprave vsebuje tri ključne funkcije: branje signala enkoderja, branje signala analogno digitalnega pretvornika in krmiljenje motorja. Vsaka od funkcij se, za izboljšanje zmogljivosti sistema, izvaja v svoji niti procesorja. Program za natezne preizkuse je spisan v programskem jeziku C++ z uporabo knjižnice Pigpio in je sestavljen iz več različnih protokolov. Vsa razvita programska oprema je odprta in prosto dostopna na svetovnem spletu.

Razviti krmilni sistem smo preverili s pomočjo nateznih preizkusov kovinskih vzmeti, rezultate meritev pa primerjali s komercialno dostopno napravo Instron 8802. Primerjava rezultatov je pokazala, da naša nadgrajena oprema zagotavlja primerljive rezultate meritev glede na komercialno dostopne naprave in je hkrati dovolj natančna, da jo lahko uporabimo v raziskovalne namene na področju karakterizacije materialnih lastnosti mehkih tkiv in drugih materialov.

Nadgradnja sistema je dobro uravnotežen kompromis med vloženimi viri in kakovostjo nastalega izdelka, saj smo drago in nezanesljivo obstoječo komercialno opremo zamenjali z rešitvijo, ki je približno 80 % cenovno ugodnejša, kot če bi kupili namenski komercialni krmilni sistem. Uporaba našega razvitega sistema je tako dostopna večini raziskovalcev na področju maloserijskega izvajanja nekomercialnih nateznih preizkusov. Čeprav je trenutni krmilni sistem omejen le za en namen, ga je mogoče enostavno preurediti za drugačne meritve ali pa ga prenesti v drug mehanični sistem.

V primerjavi s komercialnimi rešitvami na ključ smo za načrtovanje in razvoj naše rešitve porabili več časa, vendar je nadgradnja zato bolj vsestransko uporabna, cenejša in lahko prilagodljiva, hkrati pa ohranja primerljivo raven natančnosti. Razvoj te naprave je obogatil naše strokovno znanje na tem področju, kar nas je spodbudilo k razmišljanju o nadgradnji ali razvoju prihodnjih merilnih sistemov na podoben način.

Ključne besede: Raspberry Pi, krmilni sistem, merilna oprema, natezna naprava, odprtokodno, nizkocenovna strojna oprema.

*Naslov avtorja za dopisovanje: Univerza v Ljubljani, Fakulteta za strojništvo, Aškerčeva 6, 1000 Ljubljana, Slovenija, matej.kranjec@fs.uni-lj.si

Strojniški vestnik - Journal of Mechanical Engineering 66(2020)3, SI 20

Prejeto v recenzijo: 2019-08-09
Prejeto popravljeno: 2019-12-09
Odobreno za objavo: 2020-01-22

Dinamične lastnosti in napoved stabilnosti rotorja parne turbine na osnovi deformacije mreže

Heyong Si* – Lihua Cao – Pan Li
Severnovzhodna univerza za elektroenergetiko, Oddelek za energetiko in elektroenergetiko, Kitajska

Pretok pare ima pomembno vlogo pri stabilnosti rotorjev parnih turbin. Neenakomerna obodna zračnost na tesnilu zaradi ekscentričnosti rotorja povzroči neenakomerno porazdelitev pare, ta pa vibracije zaradi pretoka pare. To je glavni povzročitelj nestabilnosti rotorjev, ki pomembno vpliva na varnost parnih turbin. Analiza dinamičnih lastnosti rotorjev in stabilnosti rotorskih sistemov, vključno z vibracijami zaradi pretoka pare, je zato nujna za varno obratovanje parnih turbin.

Za preučitev mehanizma vzbujanja vibracij zaradi pretoka pare in njihovega vpliva na dinamične lastnosti rotorja parne turbine z močjo 300 MW je bila uporabljena računalniška dinamika fluidov (CFD). Izračunani so bili parametri pretočnega polja v predelu tesnila, vključno s temperaturo in tlakom. Nato je bila opravljena hitra Fourierjeva transformacija (FFT) in izračun dinamičnih koeficientov v okolju MATLAB.

Tridimenzionalno vrtinčno gibanje je bilo simulirano na osnovi deformacij mreže. Za pogon rotorja so bile vključene uporabniško definirane funkcije (UDF). Na osnovi vzbujalnih sil zaradi pretoka pare v časovni domeni in teorije majhnih motenj so bili pridobljeni podatki v frekvenčni domeni po metodi FFT. Končno so bili izračunani še dinamični koeficienti rotorja. Vplivi vrtinčnega polmera in frekvence, vrtilne hitrosti in tlačnega razmerja na dinamične lastnosti rotorja so bile analizirane z metodo krmiljene spremenljivke. Z analizo tlaka, tokovnic in kinetične energije turbulentnega tokovnega polja je bil razkrit mehanizem parametrov, ki vplivajo na vzbujanje vibracij zaradi pretoka pare.

Rezultati kažejo na nelinearno variabilnost vzbujalnih sil zaradi pretoka pare in dinamičnih koeficientov večfrekvenčnega vrtinčnega gibanja, vzbujalne sile zaradi pretoka pare pa se povečujejo z naraščanjem frekvence vrtinčenja. Dinamični koeficienti rotorja in efektivno dušenje se povečujejo z naraščanjem frekvence vrtinčenja. Vrtilna hitrost pri frekvenci vrtinčenja 24,41 Hz močno vpliva na dinamične koeficiente rotorja. Maksimalno odstopanje povprečne direktne togosti, navzkrižne togosti, direktnega dušenja in navzkrižnega dušenja znaša 8,1 %, 113,2 %, 45,8 % in 121,0 %. Efektivno dušenje močno niha pri vrednosti frekvence vrtinčenja in vrtilne frekvence 24,41 Hz. Direktna togost, direktno dušenje in efektivno dušenje se povečujejo z naraščanjem tlačnega razmerja, ki lahko izboljša stabilnost rotorja. Glavni povzročitelj vibracij, vzbujenih zaradi pretoka pare, so tlačna nihanja na površini rotorja. Z naraščanjem vrtilne frekvence se povečuje turbulentna kinetična energija in vrtinčno gibanje postane intenzivnejše. Mejo stabilnosti rotorja je mogoče natančno oceniti s pomočjo efektivnega dušenja.

Nelinearne dinamične lastnosti tesnil se razlikujejo pri različnih parametrih pare in konstrukcije tesnila, kar je bolj izraženo pri ultra-superkritičnih enotah. Obstoječa enačba za vrtinčenje ni uporabna za rotorje velikega premera (nad 800 mm) in zanje je potrebna izboljšana enačba za ultra-superkritične enote. Predmet prihodnjih raziskav bo lahko nelinearno gibanje rotorjev zaradi vibracij, ki jih vzbuja pretok pare.

V članku je predstavljen visokonatančen model vrtinčenja v skladu z dejanskim gibanjem rotorja, ki je bil postavljen po metodi CFD s funkcijami UFD. Preučen je vpliv obratovalnih parametrov na vibracije zaradi pretoka pare in dinamične lastnosti rotorja, ki ima velik pomen pri praktični izvedbi projektov.

Ključne besede: parna turbina, labirintno tesnilo, vzbujanje vibracij zaradi pretoka pare, dinamične lastnosti rotorja, deformacije mreže, stabilnost

*Naslov avtorja za dopisovanje: Severnovzhodna univerza za elektroenergetiko, Odd. za energetiko in elektroenergetiko, Jilin 132012, Kitajska, ssiheyong0927@163.com

Strojniški vestnik - Journal of Mechanical Engineering 66(2020)3, SI 21

Prejeto v recenzijo: 2019-08-24
Prejeto popravljeno: 2019-12-29
Odobreno za objavo: 2020-02-07

Eksperimentalna analiza vpliva parametrov procesa na vibracije pri visokohitrostnem brušenju odmičnih gredi

Tao Liu[1,2] – Zhaohui Deng[1,2,*] – Lishu Lv[1,2] – Shuailong She[1,2] – Wei Liu[1,2] – Chengyao Luo[1,2]

[1]Znanstveno-tehniška univerza v Hunanu, Državni laboratorij province Hunan za visokoučinkovito in natančno obdelavo materialov, težavnih za odrezavanje, Kitajska

[2]Znanstveno-tehniška univerza v Hunanu, Inštitut za inteligentno proizvodnjo, Kitajska

Sposobnost omejitve vibracij med brušenjem z izbiro ustreznih parametrov procesa je lahko v veliko pomoč pri optimizaciji procesa brušenja odmičnih gredi. Namen članka je kvantifikacija velikostnega razreda vibracij in valovitosti površine kot osnove za raziskave vpliva parametrov procesa na dinamične lastnosti pri visokohitrostnem brušenju odmičnih gredi, kakor tudi priprava smernic za optimizacijo parametrov obdelave na osnovi učinkovitih in stabilnih ciljnih vrednosti.

Najprej je bila opravljena modalna analiza za preučitev dinamičnih lastnosti stroja za brušenje odmičnih gredi. Sledila je eksperimentalna analiza vpliva parametrov procesa na vibracije pri visokohitrostnem brušenju odmičnih gredi. Preučen je bil tudi vpliv posameznih pogojev procesa brušenja na valovitost površin po brušenju.

Za poglobljeno razumevanje dinamičnih lastnosti je bil z udarnimi preizkusi določen frekvenčni odziv obdelovalnega sistema. Izveden je bil delni faktorski poskus, ki je obsegal en faktorski poskus in ortogonalni poskus. Za karakterizacijo signala pospeška v frekvenčni domeni ter preučitev vpliva različnih hitrosti in globine brušenja na velikost vibracij in valovitost površin je bila uporabljena metoda analize frekvenčnega spektra.

Rezultati jasno kažejo, da je predstavljena metoda primerna za vrednotenje parametrov procesa in zmanjšanje vibracij pri brušenju odmičnih gredi. Analiza v frekvenčni domeni je pokazala, da lahko manjša dinamična togost v določenih pogojih povzroči nestabilnost in povečanje vibracij. Najpomembnejši faktor za valovitost brušene površine je globina brušenja. Kvantifikacija vibracij in valovitosti površine za različne parametre procesa je omogočila identifikacijo najboljše izbire parametrov brušenja. Eksperimenti so pokazali, da so vibracije najmanjše pri hitrosti v_s = 120 m/s, povečujejo pa se z globino brušenja.

Potrebne bodo še dodatne raziskave za ugotavljanje tega, ali imajo različni profili odmičnih gredi pomemben vpliv na amplitudo vibracij. Z nadaljnjimi raziskavami bo mogoče razjasniti tudi vpliv obrabe brusilnih kolutov na vibracije in valovitost površin.

a. Z modalnim in vibracijskim preskusom so bile preučene vibracijske lastnosti pri visokohitrostnem brušenju neokrogle konture odmične gredi. Potrjena je bila domneva, da je frekvenca drdranja nekoliko večja od lastne frekvence sistema.

b. V ortogonalnem poskusu je bil preučen vpliv parametrov brušenja na valovitost površine in zabeležene so bile ustrezne ugotovitve.

c. Opravljenih je bilo več eksploratornih poskusov z ustrezno kombinacijo hitrosti brusilnega koluta in hitrosti obdelovanca. Potrjeno je bilo, da je mogoče s pravo kombinacijo parametrov in dinamike procesa doseči visokoučinkovito in stabilno brušenje. To bo obenem podlaga za optimizacijo parametrov procesa v naslednjem koraku.

Ključne besede: vibracije, visokohitrostno brušenje, modalna analiza, drdranje, valovitost površine, frekvenčni spekter, odmična gred

*Naslov avtorja za dopisovanje: Znanstveno-tehniška univerza v Hunanu, Inštitut za inteligentno proizvodnjo, Xiangtan, Kitajska, edeng0080@vip.sina.com

Strojniški vestnik - Journal of Mechanical Engineering 66(2020)3, SI 22

Prejeto v recenzijo: 2019-11-19
Prejeto popravljeno: 2020-01-27
Odobreno za objavo: 2020-02-13

Eksperimentalna raziskava mikrotrdote orodnega jekla EN-31 po skoraj suhi elektroerozijski obdelavi s primešanim prahom

Sanjay Sundriyal[1] -Vipin[1] – Ravinderjit Singh Walia[2,*]
[1]Tehniška univerza v Delhiju, Indija
[2]Tehniški kolidž v Punjabu, Indija

Razvita je bila hibridna konfiguracija elektroerozijske obdelave s primešanim prahom za izboljšanje mikrotrdote obdelanih preizkušancev. Uporabljena je bila zasnova preskusov L_9OA po Taguchiju s štirimi parametri obdelave na treh različnih ravneh. Izbrani procesni parametri so bili premer orodja, pretok in tlak meglice dielektrika ter koncentracija kovinskega prahu. Parametri so bili izbrani na osnovi pregleda literature in njihovega vpliva na obdelavo. Mikrotrdota obdelanih preizkušancev iz jekla EN-31 je bila izmerjena z inštrumentom Fischerscope HM2000S, izdelanim v ZDA. Inštrument ima karbidno konico, ki v preizkušancu naredi vtisk z določeno silo. Preskusi mikrotrdote so bili zaradi ponovljivosti opravljeni trikrat.

V Taguchijevi analizi je bilo izračunano razmerje med signalom in šumom (S/N) za želene in neželene vrednosti. Lastnosti izhodov se običajno delijo v dve vrsti: »več je bolje« (HB) in »manj je bolje« (LB). Cilj študije je bilo povečanje mikrotrdote obdelovancev, zato je bilo uporabljeno merilo »več je bolje«. Opravljenih je bilo 27 eksperimentov (po tri ponovitve za vsak nabor parametrov procesa). Članek poleg preiskave mikrotrdote preizkušancev iz jekla EN-31 po metodi Taguchi L_9OA predstavlja tudi analizo po metodi ANOVA za preučitev vpliva različnih parametrov procesa na izhodno mikrotrdoto.

Ugotovljeno je bilo, da postopek obdelave PMND-EDM z optimalnimi vhodnimi procesnimi parametri zagotavlja večjo mikrotrdoto izdelkov. Pri tovrstni obdelavi trdih kovin zadoščajo že majhne količine dielektričnega olja. Največja mikrotrdota obdelanega dela iz orodnega jekla EN-31 je bila dosežena pri optimalnih parametrih A1, B2, C3 in D3.

V potrditvenih preskusih je bila določena največja vrednost mikrotrdote 506,63 HV pri optimalnih parametrih. Napovedani optimalni interval zaupanja v potrditvenih preskusih (CI_{CE}) mikrotrdote je bil od 445,05 do 596,35. 95-odstotni interval napovedane srednje vrednosti mikrotrdote je bil od 482,88 do 558,52. Na površino obdelanih preizkušancev se je naložil sloj trdega cinkovega karbida, zaradi katerega se je povečala mikrotrdota. Rezultati eksperimentov so bili validirani s potrditvenimi poskusi.

Dodatek kovinskega prahu pomaga pri ustvarjanju stabilne iskre z večjo energijo zaradi povečane toplotne prevodnosti v notranji reži elektrode. Izhodne rezultate, kot so stopnja odvzema materiala, preostale napetosti in mikrotrdota, je mogoče validirati s simulacijami in modeliranjem. Čeprav se je elektroerozijska obdelava dobro uveljavila v proizvodni industriji po vsem svetu, je za ta postopek značilna nezadovoljiva morfologija nastale površine zaradi neželenih por, razpok, jamic in lukenj v obdelanih komponentah.

Elektroerozijska obdelava s primešanim prahom je dobro raziskana, do sedaj pa je bilo le malo pozornosti posvečene optimizaciji parametrov za mikrotrdoto po obdelavi s postopki PMND-EDM.

Ključne besede: elektroerozijska obdelava, prah, skoraj suha, mikrotrdota, optimizacija

*Naslov avtorja za dopisovanje: Tehniški kolidž v Punjabu, Indija, waliaravinder@yahoo.com

Strojniški vestnik - Journal of Mechanical Engineering 66(2020)3, SI 23

Prejeto v recenzijo: 2019-08-29
Prejeto popravljeno: 2019-12-27
Odobreno za objavo: 2020-02-13

Strategija vodenja s sledenjem moči za hidravlično hibridno vozilo s kolesnimi pogoni

Tao Zhang – Qiang Wang – Xiao-Hui He* – Si-Sheng Li – Xin-Min Shen
Tehniška univerza kitajske narodnoosvobodilne armade, Kolidž za terensko tehniko, Kitajska

Strategija upravljanja energije je ključnega pomena za zmanjšanje porabe goriva pri hibridnih vozilih in to je bil tudi predmet predstavljene raziskave. S teoretično in eksperimentalno analizo na preizkuševališču je bila zasnovana strategija upravljanja energije za hidravlična hibridna vozila s kolesnimi pogoni (WDHHV), ki prinaša zmanjšanje porabe goriva v primerjavi s prototipnim vozilom.

Na osnovi teoretične analize WDHHV sta bili zasnovani dve strategiji upravljanja energije: za režim vožnje in za režim zaviranja. Za režim vožnje je predlagana strategija vodenja s sledenjem moči, pri kateri je bilo na krivuljo moči motorja z notranjim zgorevanjem dodanih več delovnih točk za optimalno porabo goriva. Za režim zaviranja je bila ob upoštevanju minimalne zavorne sile glede na motor/črpalko s spremenljivo delovno prostornino in stanje napolnjenosti baterije izbrana strategija s porazdelitveno krivuljo »I« na osnovi kritične zavorne moči z_{min}, ki zagotavlja popolno rekuperacijo zavorne energije. Na preizkuševališču je bila uporabljena metoda ciklične porabe goriva pri določeni hitrosti, pospešku in pojemku na značilnem odseku poti.

Večina raziskav strategije upravljanja energije za WDHHV je danes še v fazi simulacij, kar pa ne zadošča za praktično uporabo. V predstavljeni raziskavi je bila zato zasnovana strategija upravljanja energije na osnovi teoretične analize WDHHV. Nato je bilo postavljeno preizkuševališče za določanje porabe goriva pri predlagani strategiji upravljanja energije. Motor z notranjim zgorevanjem je bil na preizkuševališču simuliran z elektromotorjem. Električna energija, ki jo je rabil motor, je bila pretvorjena v porabo goriva motorja z notranjim zgorevanjem na razdalji 100 kilometrov.

Poraba goriva, določena v tej raziskavi, je bila primerjana s porabo goriva prototipnega vozila. Za WDHHV je bilo ugotovljeno, da predlagana strategija upravljanja energije učinkovito zmanjša porabo goriva za več kot 24,0 %, ne da bi to vplivalo na dinamične zmogljivosti vozila. Poraba goriva v ciklu *Federal Urban Driving Schedule* (FUDS) je bila v primerjavi s ciklom *Extra Urban Driving Schedule* (EUDC-1) manjša za 4,73 % zaradi pogostih zagonov in zaustavitev, ki so značilne za cikel FUDS. Energijo je bilo mogoče v celoti rekuperirati in nato izkoristiti v naslednji fazi, poraba goriva pa se je efektivno zmanjšala.

Raziskava je imela tudi določene omejitve. Zasnova preizkuševališča uvaja določeno napako zaradi simulacije motorja z notranjim zgorevanjem z elektromotorjem. Za povečanje praktične uporabnosti raziskave bodo opravljene nadaljnje študije strategije upravljanja energije na realnih vozilih.

Za vozni režim WDHHV je bila zasnovana strategija vodenja s sledenjem moči na osnovi krivulje moči za optimalno porabo goriva. Za zavorni režim je bila izbrana strategija s porazdelitveno krivuljo »I« na osnovi kritične zavorne moči z_{min}. Rezultati poskusov kažejo, da predlagana strategija upravljanja energije v obeh režimih izpolnjuje zahteve glede dinamičnih zmogljivosti vozila, poraba goriva pa je v primerjavi s prototipnim vozilom manjša za 24,0 %, kar potrjuje učinkovitost predlagane strategije. Rezultati raziskave bodo tako dobra osnova za nadaljnje preskuse z realnimi vozili.

Ključne besede: hidravlično hibridno vozilo s kolesnimi pogoni, strategija vodenja s sledenjem moči, strategija porazdelitve zavorne sile, vozni cikel, poraba goriva, preizkuševališče

*Naslov avtorja za dopisovanje: Tehniška univerza kitajske narodnoosvobodilne armade, Kolidž za terensko tehniko, Kitajska, gcbhxh@qq.com

Strojniški vestnik - Journal of Mechanical Engineering 66(2020)3, SI 24

Prejeto v recenzijo: 2019-11-11
Prejeto popravljeno: 2020-01-20
Odobreno za objavo: 2020-02-20

Vpliv porazdelitve jalovine na rezalno silo in specifično energijo pri pridobivanju premoga

Kao Jiang – Kuidong Gao – Lirong Wan*
Znanstveno tehniška univerza v Shandongu, Kolidž za stojništvo in elektrotehniko, Kitajska

Danes obstaja veliko raziskav na temo učinkovitosti pridobivanja premoga, modeli premoga pa običajno ne vključujejo jalovine. Minerali v obliki jalovine so pogosti v premogovnih žilah in močno vplivajo na zmogljivost delovanja rezalnega orodja. Pričujoči članek zato obravnava zmogljivost rezalnega orodja pri različnih porazdelitvah jalovine v premogovni žili.

Raziskava vpliva jalovine in njene porazdelitve na zmogljivost rezanja se začne z analizo porazdelitve jalovine v premogovni žili. Ni veliko obstoječih raziskav, ki bi opisovale, kako pridobiti točne informacije o lokaciji jalovine v premogovni žili. Za nadaljnje študije je zato najprej treba določiti porazdelitveno funkcijo, ki bo pokrivala čim več potencialnih porazdelitev jalovine.

Za opis porazdelitve jalovine v premogovni žili je bila uporabljena Gaussova funkcija. Ta s prilagoditvijo srednje vrednosti in variance omogoča zajem različnih porazdelitev jalovine. Končno je določena še rezalna zmogljivost pri različnih porazdelitvah.

Rezultati in ugotovitve:

(1) V članku je uporabljena porazdelitvena funkcija za simulacijo potencialnih porazdelitev jalovine v premogovnih žilah. Rezultati kažejo, da je porazdelitvena funkcija primerna za simulacijo različnih deležev jalovine na različnih višinah.
(2) Povečanje srednje rezalne sile zaradi jalovine je tesno povezano z lokacijo jalovine. Rezultati kažejo močno korelacijo med povečanjem rezalne sile in lokacijo jalovine v premogovni žili – koeficient korelacije presega 0,98.
(3) Povečanje srednje rezalne sile zaradi jalovine se pri različnih porazdelitvah močno spreminja. Koncentrirana jalovina v premogovni žili povzroči znatno povečanje rezalnih sil, še posebej, če je koncentracija sredi premogovne žile.
(4) Izračunano je bilo tudi povečanje specifične energije zaradi jalovine v premogovni žili pri različnih porazdelitvah. Ta veličina je v nelinearni zvezi s porazdelitvijo jalovine ter v linearni zvezi z dolžino premogovne žile in s količino mineralov jalovine v njej.

Glede na izhodišča članka je bila preučena samo rezalna zmogljivost enega rezalnega orodja in ne celega rezalnega bobna. V prihodnje bo mogoče preučiti še rezalno zmogljivost rezalnega bobna pri različnih porazdelitvah jalovine.

Pričujoči članek je prvi, ki upošteva jalovino in njeno porazdelitev pri računanju rezalnih sil in specifične porabe energije v procesu pridobivanja premoga. Potencialna porazdelitev jalovine v premogovni žili je simulirana s prilagajanjem srednje vrednosti in variance porazdelitvene funkcije. Te porazdelitve so lahko v pomoč pri preučevanju rezalne zmogljivosti v zahtevnih pogojih.

Ključne besede: jalovina, porazdelitev jalovine, Gaussova porazdelitvena funkcija, rezalna sila, specifična poraba energije, eno rezalno orodje

*Naslov avtorja za dopisovanje: Znanstveno tehniška univerza v Shandongu, Kolidž za stojništvo in elektrotehniko, Kitajska, wansdust@163.com

Prof. dr. Franc Gologranc – starosta preoblikovanja – je dopolnil 100 let

Letos sredi februarja smo na Fakulteti za strojništvo praznovali visoki jubilej – stoletnico rojstva našega najstarejšega profesorja in hkrati tudi najstarejšega še živečega diplomanta Fakultete za strojništvo prof. dr. Franca Gologranca. Visoki jubilej smo proslavili s slovesnostjo, ki so se je udeležili številni aktivni in upokojeni profesorji Fakultete za strojništvo, nekdanji magistranti in diplomanti prof. Gologranca ter gost Univ.-Prof. Dr.-Ing. Dr. h. c. Mathias Liewald z Inštituta za preoblikovanje v Stuttgartu, kjer je prof. Gologranc doktoriral.

Profesor dr. Franc Gologranc se je rodil leta 1920 v Slovenskih Konjicah. Dijaška leta je preživljal v Mariboru in Celju, po maturi pa se je leta 1938 vpisal na elektrostrojni oddelek Tehniške fakultete v Ljubljani. Žal je njegov študij prekinila vojna, lahko ga je nadaljeval šele leta 1947 in februarja leta 1950 diplomiral kot šestnajsti diplomant Fakultete za strojništvo.

Po diplomi je prejel dekret za zaposlitev v Železarni na Jesenicah, a je bil takoj premeščen v Centralni konstrukcijski biro Ministrstva za težko industrijo v Ljubljani, kjer so projektirali opremo za železarne in strojne tovarne. Po ukinitvi biroja l. 1952 je bil kot konstrukter premeščen v Inštitut za mehansko tehnologijo na Oddelku za strojništvo Tehniške fakultete, nato pa izvoljen v naziv asistenta.

Želja in potreba po pridobivanju znanja in izkušenj na novem področju ga je kmalu vodila v tujino. V letih 1952 do 1958 je bil v intervalih dvakrat po eno leto na specializaciji v dveh velikih tovarnah težkih obdelovalnih strojev v ZR Nemčiji ter en semester na študiju na TVŠ Aachen. Do leta 1960 je bilo njegovo strokovno in pedagoško delo usmerjeno v širše področje mehanske tehnologije in obdelovalnih strojev. Ko pa je bil tega leta uveden tristopenjski študij strojništva s tremi usmeritvami, se je po 10 letih praktičnih izkušenj kot konstrukter in kot asistent prijavil na eno od razpisanih mest za učitelja v tehnološki smeri in bil spomladi 1961 habilitiran za docenta za tehniko preoblikovanja in teorijo plastičnega preoblikovanja - takrat novo vpeljani tehnološki disciplini na fakulteti.

V težnji po nenehnem izobraževanju je prof. Gologranc kmalu ugotovil, da na mestu docenta ne bo mogel biti brez doktorskega naziva. Ker v tistih

Profesor Gologranc na slavnostnem predavanju februarja 2020

časih na področju nekdanje Jugoslavije ni našel mentorja s področja takrat še mlade znanstvene vede preoblikovanja, je navezal stike z znanstveniki v ZRN, še posebej z Univerzo v Stuttgartu. Tam se je s predstojnikom novo ustanovljenega Inštituta za preoblikovalno tehniko prof. dr. Kurtom Langejem uspel dogovoriti za dolgoročno financirano raziskovalno delo, ki ga je moral združevati s svojimi pedagoškimi obveznostmi v Ljubljani.

Vztrajnost in raziskovalni duh sta ga gnala, da je s presledki od leta 1967 do 1974 v Stuttgartu razvil novo metodo določanja krivulje plastičnega tečenja materiala. Metodo je predstavil v tuji in domači literaturi in leta 1975 v Stuttgartu tudi doktoriral.

Prvi preizkusi vrednotenja preoblikovalnosti materiala z novo razvito metodo izbočevanja pločevine so zaradi pomanjkanja opreme v prvih razvojnih fazah bili za današnje pojme dokaj primitivni, saj so spremembe na pločevini merili z merilnimi uricami, te pa v enakomernih časovnih intervalih fotografirali kar s fotoaparatom. Prof. Gologranc je z leti metodo izpopolnil in že leta 1980 v Strojniškem vestniku predstavil celoten avtomatiziran sistem za vrednotenje plastičnih lastnosti pločevine [1].

Svojo pedagoško in znanstveno-raziskovalno pot je prof. Gologranc po zaključenem doktoratu nadaljeval na Fakulteti za strojništvo v Ljubljani, kjer je leta 1982 bil izvoljen v naziv rednega profesorja. Vsa leta delovanja od leta 1961 na Fakulteti za strojništvo se je intenzivno zavzemal za širjenje znanja o postopkih preoblikovanja in že sredi šestdesetih let

je uspešno zasnoval Laboratorij za preoblikovanje. V njem so kmalu stekle sistematične raziskave tako masivnega preoblikovanja kot tudi preoblikovanja pločevine. V Stuttgartu pridobljeno znanje je uspešno prenesel v slovenski prostor in s številnimi znanstveno-raziskovalnimi projekti in direktnim sodelovanjem z industrijo dvigal nivo predelave predvsem pločevinskih materialov v slovenski industriji. S svojim sodelovanjem s podjetji IMV, CIMOS, TAM, EMO in drugimi je ključno doprinesel k uveljavljanju postopkov preoblikovanja v slovenskem prostoru. Intenzivno je tudi povezoval svoje pedagoško in znanstveno poslanstvo, saj je v času svoje profesorske aktivnosti na Fakulteti za strojništvo v Ljubljani bil mentor preko 100 diplomantom na dodiplomskem kot tudi podiplomskem študiju.

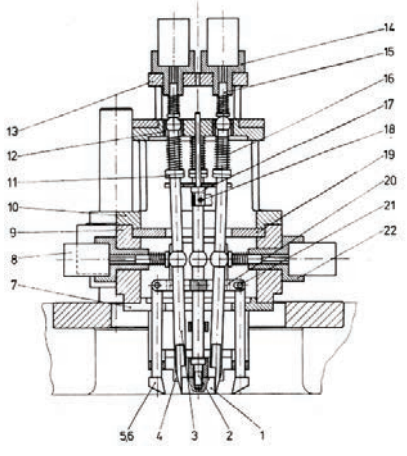

Tenzo-sferometer za avtomatiziran zajem podatkov deformiranja pločevine **[1]**

Prof. Gologranc se je tudi zavedal, da ima pri širjenju znanja o preoblikovanju ključno vlogo tako tuja kot tudi domača znanstvena literatura. Zato je svoja odkritja in znanstvene doprinose objavljal v tujih revijah (najpogosteje Industrie Anzeiger), pri širjenju svojih znanstvenih dognanj v jugoslovanskem prostoru pa se je najpogosteje posluževal ravno našega Strojniškega vestnika. Tako je v Strojniškem vestniku v letih svojega aktivnega znanstvenega delovanja objavil kar 27 strokovnih člankov, prvega že v prvem letniku izhajanja revije, kjer je poročal o razvoju, stanju tehnike in perspektivah na področju fine obdelave ter 10 znanstveno-raziskovalnih objav, v katerih rapravlja že o karakteristikah in dinamičnem izkoristku vretenskih stiskalnic pri preoblikovanju **[2]**.

V svojih člankih v Strojniškem vestniku je prof. Gologranc predstavil svoje široko poznavanje področja obdelav materialov, pri čemer se ni omejil le na področje preoblikovanja temveč je poročal tudi o napredkih in možnostih uporabe elektroerozijske obdelave **[3]** materialov in ultrazvočne obdelave za razmaščevanje in čiščenje **[4]**. Svoje glavne raziskave pa je seveda usmerjal v področja masivnega preoblikovanja **[5]** in predvsem preoblikovanja pločevine **[6]** do **[9]**, kjer je doprinesel tudi največ v bogato zakladnico tehnološkega znanja. Poleg objav v znanstvenih revijah je širil v industriji tudi svoje strokovno znanje z udeležbo na številnih srečanjih kovinsko-predelovalne industrije, kjer se je razpravljalo o sodobnih trendih predelave materialov. Prof. Gologranc je za slovensko stroko napisal tudi učbenike s področja preoblikovanja, prvega Tehnika preoblikovanja že leta 1963, nekoliko let kasneje pa še Uvod v preoblikovanje ter Preoblikovanje 1. del in Preoblikovanje 2. del – Masivno preoblikovanje.

Ob koncu pregleda dela prof. dr. Franca Gologranca lahko zapišem, da nam je s svojo iznajdljivostjo, vztrajnostjo, raziskovalnim duhom ter energijo, ki smo jo vsi prisotni doživeli ob njegovem jubilejnem predavanju februarja 2020, še ob svojem visokem jubileju zgled znanstvenika, ki je svoje življenje posvetil razvoju preoblikovanja kovin.

Spoštovanemu profesorju ob izjemnem življenjskem jubileju iskreno čestitamo, želimo veliko zadovoljstva, zdravja in osebne sreče.

Viri

[1] Gologranc, F. (1980). Kontinuirni izbočevalni preizkus za avtomatično snemanje krivulj plastičnosti. *Strojniški vestnik*, let. 26, št. 7-9, str. 93-98.

[2] Gologranc, F. (1966). Preoblikovanje kovin z velikimi hitrostmi. *Strojniški vestnik*, let. 12, št. 1-2, str. 19-28.

[3] Gologranc, F. (1958). Elektroerozivna obdelava kovin. *Strojniški vestnik*, let. 4, št. 3-4, str. 65-72.

[4] Gologranc, F. (1959). Ultra zvok kot tehnološko sredstvo za obdelavo materialov. *Strojniški vestnik*, let. 5, št. 3, str. 74-77.

[5] Gologranc, F. (1965). O nekaterih sodobnih metodah preoblikovanja z valjanjem. *Strojniški vestnik*, let. 11, št. 3, str. 73-82.

[6] Gologranc, F. (1965). Fino rezanje v tehniki štancanja. Strojniški vestnik, let. 11, št. 6, str. 155-165.

[7] Gologranc, F. (1973). Analitična interpretacija krivulje plastičnosti ter vpliv plastične anizotropije. *Strojniški vestnik*, let. 19, št. 4-5, str. 121-124.

[8] Gologranc, F. (1973). Opredelitev krivulje plastičnosti pri izotropnem utrjanju materiala. *Strojniški vestnik*, let. 19, št. 3, str. 71-75.

[9] Kampuš, Z., Gologranc, F. (1990). Analiza deformacij pri globokem vlečenju brez zadrževala pločevine. *Strojniški vestnik*, let. 36, št. 1-3, str. 9-12.

izr. prof. dr. Tomaž Pepelnjak
vodja Laboratorija za preoblikovanje,
Fakulteta za strojništvo, Univerza v Ljubljani

Guide for Authors

All manuscripts must be in English. Pages should be numbered sequentially. The manuscript should be composed in accordance with the Article Template given above. The maximum length of contributions is 12 pages (approx. 5000 words). Longer contributions will only be accepted if authors provide justification in a cover letter. For full instructions see the Information for Authors section on the journal's website: http://en.sv-jme.eu .

SUBMISSION:

Submission to SV-JME is made with the implicit understanding that neither the manuscript nor the essence of its content has been published previously either in whole or in part and that it is not being considered for publication elsewhere. All the listed authors should have agreed on the content and the corresponding (submitting) author is responsible for having ensured that this agreement has been reached. The acceptance of an article is based entirely on its scientific merit, as judged by peer review. Scientific articles comprising simulations only will not be accepted for publication; simulations must be accompanied by experimental results carried out to confirm or deny the accuracy of the simulation. Every manuscript submitted to the SV-JME undergoes a peer-review process.

The authors are kindly invited to submit the paper through our web site: http://ojs.sv-jme.eu. The Author is able to track the submission through the editorial process - as well as participate in the copyediting and proofreading of submissions accepted for publication - by logging in, and using the username and password provided.

SUBMISSION CONTENT:

The typical submission material consists of:

- A **manuscript** (A PDF file, with title, all authors with affiliations, abstract, keywords, highlights, inserted figures and tables and references),
- Supplementary files:
  - a **manuscript** in a WORD file format
  - a **cover letter** (please see instructions for composing the cover letter)
  - a ZIP file containing **figures** in high resolution in one of the graphical formats (please see instructions for preparing the figure files)
  - possible **appendicies** (optional), cover materials, video materials, etc.

Incomplete or improperly prepared submissions will be rejected with explanatory comments provided. In this case we will kindly ask the authors to carefully read the Information for Authors and to resubmit their manuscripts taking into consideration our comments.

COVER LETTER INSTRUCTIONS:

Please add a **cover letter** stating the following information about the submitted paper:

1. Paper **title**, list of **authors** and their **affiliations**. **One** corresponding author should be provided.
2. **Type of paper**: original scientific paper (1.01), review scientific paper (1.02) or short scientific paper (1.03).
3. A **declaration** that neither the manuscript nor the essence of its content has been published in whole or in part previously and that it is not being considered for publication elsewhere.
4. State the **value of the paper** or its practical, theoretical and scientific implications. What is new in the paper with respect to the state-of-the-art in the published papers? Do not repeat the content of your abstract for this purpose.
5. We kindly ask you to suggest at least two **reviewers** for your paper and give us their names, their full affiliation and contact information, and their scientific research interest. The suggested reviewers should have at least two relevant references (with an impact factor) to the scientific field concerned; they should not be from the same country as the authors and should have no close connection with the authors.

FORMAT OF THE MANUSCRIPT:

The manuscript should be composed in accordance with the Article Template. The manuscript should be written in the following format:

- A **Title** that adequately describes the content of the manuscript.
- A list of **Authors** and their **affiliations**.
- An **Abstract** that should not exceed 250 words. The Abstract should state the principal objectives and the scope of the investigation, as well as the methodology employed. It should summarize the results and state the principal conclusions.
- 4 to 6 significant **key words** should follow the abstract to aid indexing.
- 4 to 6 **highlights;** a short collection of bullet points that convey the core findings and provide readers with a quick textual overview of the article. These four to six bullet points should describe the essence of the research (e.g. results or conclusions) and highlight what is distinctive about it.
- An **Introduction** that should provide a review of recent literature and sufficient background information to allow the results of the article to be understood and evaluated.
- A **Methods** section detailing the theoretical or experimental methods used.
- An **Experimental section** that should provide details of the experimental set-up and the methods used to obtain the results.
- A **Results** section that should clearly and concisely present the data, using figures and tables where appropriate.
- A **Discussion** section that should describe the relationships and generalizations shown by the results and discuss the significance of the results, making comparisons with previously published work. (It may be appropriate to combine the Results and Discussion sections into a single section to improve clarity.)
- A **Conclusions** section that should present one or more conclusions drawn from the results and subsequent discussion and should not duplicate the Abstract.
- **Acknowledgement** (optional) of collaboration or preparation assistance may be included. Please note the source of funding for the research.
- **Nomenclature** (optional). Papers with many symbols should have a nomenclature that defines all symbols with units, inserted above the references. If one is used, it must contain all the symbols used in the manuscript and the definitions should not be repeated in the text. In all cases, identify the symbols used if they are not widely recognized in the profession. Define acronyms in the text, not in the nomenclature.
- **References** must be cited consecutively in the text using square brackets [1] and collected together in a reference list at the end of the manuscript.
- **Appendix(-icies)** if any.

SPECIAL NOTES

Units: The SI system of units for nomenclature, symbols and abbreviations should be followed closely. Symbols for physical quantities in the text should be written in italics (e.g. *v*, *T*, *n*, etc.). Symbols for units that consist of letters should be in plain text (e.g. ms^{-1}, K, min, mm, etc.). Please also see: http://physics.nist.gov/cuu/pdf/sp811.pdf .

Abbreviations should be spelt out in full on first appearance followed by the abbreviation in parentheses, e.g. variable time geometry (VTG). The meaning of symbols and units belonging to symbols should be explained in each case or cited in a **nomenclature** section at the end of the manuscript before the References.

Figures (figures, graphs, illustrations digital images, photographs) must be cited in consecutive numerical order in the text and referred to in both the text and the captions as Fig. 1, Fig. 2, etc. Figures should be prepared without borders and on white grounding and should be sent separately in their original formats. If a figure is composed of several parts, please mark each part with a), b), c), etc. and provide an explanation for each part in Figure caption. The caption should be self-explanatory. Letters and numbers should be readable (Arial or Times New Roman, min 6 pt with equal sizes and fonts in all figures). Graphics (submitted as supplementary files) may be exported in resolution good enough for printing (min. 300 dpi) in any common format, e.g. TIFF, BMP or JPG, PDF and should be named Fig1.jpg, Fig2.tif, etc. However, graphs and line drawings should be prepared as vector images, e.g. CDR, AI. Multi-curve graphs should have individual curves marked with a symbol or otherwise provide distinguishing differences using, for example, different thicknesses or dashing.

Tables should carry separate titles and must be numbered in consecutive numerical order in the text and referred to in both the text and the captions as Table 1, Table 2, etc. In addition to the physical quantities, such as *t* (in italics), the units [s] (normal text) should be added in square brackets. Tables should not duplicate data found elsewhere in the manuscript. Tables should be prepared using a table editor and not inserted as a graphic.

REFERENCES:

A reference list must be included using the following information as a guide. Only cited text references are to be included. Each reference is to be referred to in the text by a number enclosed in a square bracket (i.e. [3] or [2] to [4] for more references; do not combine more than 3 references, explain each). No reference to the author is necessary.

References must be numbered and ordered according to where they are first mentioned in the paper, not alphabetically. All references must be complete and accurate. Please add DOI code when available. Examples follow.

Journal Papers:

Surname 1, Initials, Surname 2, Initials (year). Title. Journal, volume, number, pages, DOI code.

[1] Hackenschmidt, R., Alber-Laukant, B., Rieg, F. (2010). Simulating nonlinear materials under centrifugal forces by using intelligent cross-linked simulations. *Strojniški vestnik - Journal of Mechanical Engineering,* vol. 57, no. 7-8, p. 531-538, DOI:10.5545/sv-jme.2011.013.

Journal titles should not be abbreviated. Note that journal title is set in italics.

Books:

Surname 1, Initials, Surname 2, Initials (year). Title. Publisher, place of publication.

[2] Groover, M.P. (2007). *Fundamentals of Modern Manufacturing.* John Wiley & Sons, Hoboken.

Note that the title of the book is italicized.

Chapters in Books:

Surname 1, Initials, Surname 2, Initials (year). Chapter title. Editor(s) of book, book title. Publisher, place of publication, pages.

[3] Carbone, G., Ceccarelli, M. (2005). Legged robotic systems. Kordić, V., Lazinica, A., Merdan, M. (Eds.), Cutting Edge Robotics. Pro literatur Verlag, Mammendorf, p. 553-576.

Proceedings Papers:

Surname 1, Initials, Surname 2, Initials (year). Paper title. Proceedings title, pages.

[4] Štefanić, N., Martinčević-Mikić, S., Tošanović, N. (2009). Applied lean system in process industry. *MOTSP Conference Proceedings*, p. 422-427.

Standards:

Standard-Code (year). Title. Organisation. Place.

[5] ISO/DIS 16000-6.2:2002. *Indoor Air – Part 6: Determination of Volatile Organic Compounds in Indoor and Chamber Air by Active Sampling on TENAX TA Sorbent, Thermal Desorption and Gas Chromatography using MSD/FID.* International Organization for Standardization. Geneva.

WWW pages:

Surname, Initials or Company name. Title, from http://address, date of access.

[6] Rockwell Automation. Arena, from *http://www.arenasimulation.com,* accessed on 2009-09-07.

EXTENDED ABSTRACT:

When the paper is accepted for publishing, the authors will be requested to send an **extended abstract** (approx. one A4 page or 3500 to 4000 characters or approx. 600 words). The instruction for composing the extended abstract are published on-line: http://www.sv-jme.eu/information-for-authors/ .

COPYRIGHT:

Authors submitting a manuscript do so on the understanding that the work has not been published before, is not being considered for publication elsewhere and has been read and approved by all authors. The submission of the manuscript by the authors means that the authors automatically agree to transfer copyright to SV-JME when the manuscript is accepted for publication. All accepted manuscripts must be accompanied by a Copyright Transfer Agreement, which should be sent to the editor. The work should be original work by the authors and not be published elsewhere in any language without the written consent of the publisher. The proof will be sent to the author showing the final layout of the article. Proof correction must be minimal and executed quickly. Thus it is essential that manuscripts are accurate when submitted. Authors can track the status of their accepted articles on http://en.sv-jme.eu/.

PUBLICATION FEE:

Authors will be asked to pay a publication fee for each article prior to the article appearing in the journal. However, this fee only needs to be paid after the article has been accepted for publishing. The fee is 380 EUR (for articles with maximum of 6 pages), 470 EUR (for articles with maximum of 10 pages), plus 50 EUR for each additional page. The additional cost for a color page is 90.00 EUR (only for a journal hard copy; optional upon author's request). These fees do not include tax.

Strojniški vestnik -Journal of Mechanical Engineering
Aškerčeva 6, 1000 Ljubljana, Slovenia, e-mail: info@sv-jme.eu

9 770039 248001
ISSN 0039-2480

http://www.sv-jme.eu

Contents

Papers